Politecnico
di Torino

DENERG Department of Energy “Galileo Ferraris”
Master’s Degree Course in Electrical Engineering

Master’s Thesis *in*

Comparative Finite Element Analysis of Surface-Mounted and V-Shape Interior Axial-Flux Permanent Magnet Machines for Electric Traction

Supervisors:

Dr. Federica Graffeo

Prof. Silvio Vaschetto

Eng. Fabio Venturini

Candidate: Luca Mandrile

Academic Year: 2025/2026

Contents

List of Figures

List of Tables

Abstract

The electrification of automotive and traction applications has intensified demand for electric machines combining high torque density with extended speed operation. In this framework, Axial Flux Permanent Magnet (AF-PM) machines are emerging as an alternative to conventional Radial Flux topologies, offering compact axial length and specific torque capabilities. While the Surface-Mounted Permanent Magnet (AF-SPM) configuration represents the current industrial standard for axial flux motors, the Interior Permanent Magnet (IPM) topology remains less explored for the axial technology. The primary objective of this thesis is to perform a comparative study between a Surface-Mounted (AF-SPM) and a novel V-shaped Interior Permanent Magnet (AF-IPM) axial flux machine. The comparison is conducted under parity conditions: both machines share the same stator geometry, winding layout, and rated electrical constraints, ensuring that any performance deviation is strictly attributable to the rotor anisotropy and magnet placement. The analysis methodology relies on a Finite Element Analysis (FEA) approach. Detailed 3D models were developed using Altair Flux™ to capture complex electromagnetic phenomenon. A dedicated co-simulation environment was established by coupling Flux 3D with MATLAB®. This framework allowed for automated extraction of current to flux maps. To fully explore the potential of the designs for high-performance traction applications, the investigation was extended to a Peak Performance scenario by doubling the supply current limit.

Introduction

The transition towards electric mobility is imposing stringent requirements on traction systems. In the automotive sector, growing demands for higher power density and efficiency have led to a transition from conventional induction machines to Permanent Magnet Synchronous Machines (PMSMs). In this framework, Radial Flux (RF) topologies represent the consolidated standard. Specifically, the Radial Flux Interior Permanent Magnet (RF-IPM) machine has become the dominant solution for electric vehicles due to its ability to combine high torque density with a wide Constant Power Speed Range (CPSR) through effective flux-weakening operations.

However, the continuous demand for powertrain compactness and weight reduction has directed research interest towards Axial Flux Permanent Magnet (AF-PM) machines. Characterized by a disk-shaped structure, AFPMs offer a higher torque-to-weight ratio and a shorter axial length compared to their radial counterparts. Despite these geometric advantages, the majority of commercial AFPM machines currently rely on Surface-Mounted (AF-SPM) rotor configurations. While the AF-SPM topology excels in torque generation, it inherently suffers from limited flux-weakening capabilities. This limitation restricts the high-speed operational range, often forcing the adoption of multi-speed gearboxes or oversized supply voltage.

To integrate the compactness of axial flux machines and the high-speed performance of interior magnet topologies, this thesis investigates the design and performance of an Axial Flux Interior Permanent Magnet (AF-IPM) machine featuring a V-shaped magnet disposition. The primary objective is to conduct a rigorous comparative analysis between a standard AF-SPM and the proposed AF-IPM design. To ensure a fair comparison, the study imposes strict parity conditions: both machines share identical stator geometries, winding configurations, and thermal/electrical constraints. This approach isolates the rotor topology as the only variable, allowing for a precise assessment of how magnetic saliency and magnet placement influence the machine's behavior. The V-shaped rotor geometry analyzed in this study is inspired by the research presented by Tekgun et al. [1] .This thesis aims to independently validate the effectiveness of the V-shaped topology. To conduct the comparative analysis, high-fidelity 3D models were developed using Altair Flux software. Unlike 2D approximations, which are often insufficient for axial flux topologies due to significant 3D leakage paths and edge effects, this work utilizes full 3D Finite Element Analysis (FEA) to fully capture the electromagnetic phenomena with maximum accuracy.

A key focus of this work is the investigation of the operating limits of the two topologies. The study goes beyond nominal rating conditions, performing a "Peak Performance" analysis to illustrate the machine behavior under high-current scenarios, with the aim of highlighting the benefits of the V-shaped IPM design by comparing the AF-SPM and AF-IPM machines in terms of torque, power and flux-weakening capability.

Thesis outline

This work is organized according to the methodological sequence followed during the research activities. The thesis begins in Chapter 1 by establishing the theoretical framework necessary for the study. This section reviews the state of the art of Permanent Magnet Synchronous Machines, focusing on the evolution from Radial Flux to Axial Flux topologies. It critically analyzes the structural and magnetic differences between Surface-Mounted (SPM) and Interior Permanent Magnet (IPM) configurations, clarifying the motivation for investigating the V-shaped rotor geometry in the axial domain. With the theoretical framework established, Chapter 2 describes the construction of the AF-SPM and AF-IPM model geometries within the Altair Flux™ environment. In particular, it details the geometric definition based on elementary entities (points and lines) established using specific coordinate systems and geometric transformations. Subsequently, the chapter outlines the assignment of physics regions, associating specific material properties to each volume generated by the geometry. Finally, the section presents a comparative analysis of the air-gap flux density for both machines, highlighting their respective harmonic contents. The analysis moves to the dynamic domain in Chapter 3, which is dedicated to Transient Magnetic Analysis and no-load characterization. This section defines the external electrical circuit coupled to the 3D model. Subsequently, the no-load test is performed to obtain the Back-Electromotive Force (Back-EMF) waveforms and the flux linkage values. These data are then processed by a specific MATLAB script to calculate the initial rotor offset, ensuring the correct alignment of the machine for the following on-load simulations. The methodology for the on-load performance analysis is elaborated in Chapter 4, which illustrates the integrated co-simulation environment established between Flux 3D and MATLAB®. This chapter details the automated parametric sweep algorithms used to construct the current to flux maps over the entire current plane. Furthermore, it explains the post-processing logic developed to compute the optimal trajectories, specifically the Maximum Torque Per Ampere (MTPA) and Flux-Weakening capabilities, taking into account the supply's voltage and current limits. The core of the research is presented in Chapter 5, where the comparative results are discussed in depth. The chapter begins by analyzing the magnetic saturation and cross-coupling effects observed in the flux maps. It then compares the mechanical characteristics of the two machines under rated current conditions, highlighting their inherent voltage limitations and torque drop-off at high speeds. The investigation is then extended to a "Peak Performance" scenario, demonstrating how the AF-IPM topology successfully overcomes these constraints under high-current conditions, thereby unlocking the MTPV region and achieving a significantly extended Constant Power Speed Range (CPSR).

1 State of the Art of Synchronous PM Machines

1.1 Evolution of permanent magnet machines

The history of permanent magnets is closely related to the evolution of permanent magnet machines, beginning in the first half of the 20th century. The first materials used for permanent magnets in the 1950s were ferrite and barium ferrite, followed later by aluminum-nickel-cobalt (AlNiCo). One of the earliest machine applications with AlNiCo was a new AC machine described by Merril in 1955 [2]. Rare-earth material for permanent magnets appeared in the 1960s, evolving from samarium cobalt (SmCo) to the more recent neodymium boron iron (NdFeB), which provides an impressive maximum energy product (BH_{max}). Today, NdFeB is considered one of the best permanent magnets available on the market as reported in Table 1.1.

Table 1.1 - Hard magnetic material properties

Material	Remanent flux density (Br) [Wb/m2]	Coercitive force (Hc) [kA/m]
Ferrite	0.20 - 0.43	150 - 350
FeCo	0.8	40
AlNiCo	0.61 - 1.3	40 - 60
SmCo	1.25	950
NdFeB	1.4	800

To understand the evolution of electric drives, it is necessary to compare the properties of the different hard magnetic materials developed over the decades. As summarized in Table 1.1, each material offers a specific trade-off between magnetic performance, thermal stability, and cost.

Ferrites (Ceramic Magnets) are electrically insulated and highly resistant to corrosion. While they are extremely cost-effective, their low remanence (Br) and low energy product (BH_{max}) make them unsuitable for high-performance traction applications. Similarly, AlNiCo magnets boast a high remanent flux density and excellent thermal stability. However, their very low coercivity (Hc) makes them susceptible to demagnetization, limiting their use in modern variable-speed drives where strong demagnetizing fields are present. A significant technological leap was achieved with the introduction of rare-earth materials, starting with Samarium-Cobalt(SmCo) representing the first generation of this class. SmCo offers high energy density and superior thermal stability, maintaining performance at high temperatures where other materials fail. Neodymium-Iron-Boron (NdFeB) represents the current state of the art. As shown in Figure 1.1, NdFeB exhibits the highest maximum energy product (BH_{max}) and coercive force among all commercial magnets. Its primary limitation is its thermal behavior: its Curie temperature (critical threshold at which the material loses its permanent magnetic properties) is lower than that of SmCo, restricting standard operation to approximately 200°C depending on the specific grade.

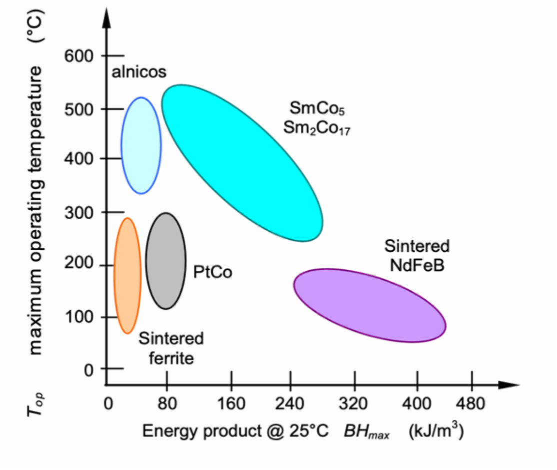

Figure 1.1 - Energy product as function of operating temperature [2]

Nevertheless, due to its superior mechanical strength, highest flux density per unit volume, and relatively lower cost compared to SmCo, NdFeB is currently the preferred choice for automotive traction machines, where high torque density and efficiency are key requirements.

1.2 Synchronous PM Machines

PM brushless machines have become the preferred choice for automotive traction applications over induction machines. Their main advantages include higher torque density due to their reduced weight and volume, superior efficiency as there are no rotor copper losses, and easier cooling since heat is primarily generated in the stator [3]. However, they face significant disadvantages. The elevated cost of these machines is directly attributable to the utilization of permanent magnets composed of rare-earth elements. Furthermore, high speeds can compromise the mechanical integrity of the permanent magnets on the rotor, and there is a risk of accidental demagnetization under high operating temperatures.

PM brushless machines have a simple structure, consisting of a stator with multi-phase windings and a rotor with permanent magnet poles (Fig. 1.2).

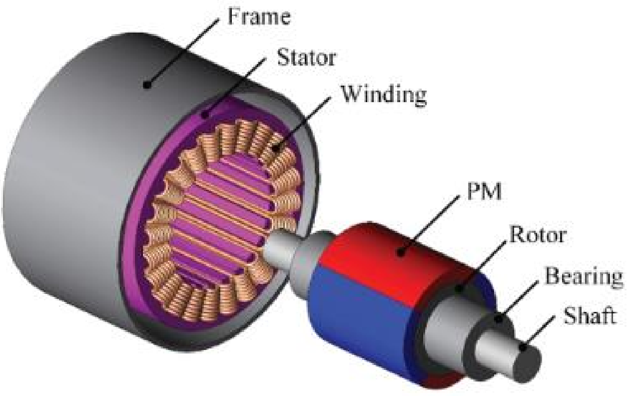

Figure 1.2 - brushless structure [3]

In a PM synchronous machine, when the windings are supplied with three-phase sinusoidal currents, a rotating magnetic field is created. Consequently, the rotor follows this field, rotating in perfect synchronism at a speed that is directly dependent on the frequency of the applied current [3].

Permanent Magnet Synchronous Machines (PMSMs) can be primarily classified based on two fundamental criteria: the direction of the magnetic flux path through the air-gap and the positioning of the permanent magnets within the rotor structure.

Flux Direction Classification: The most significant structural distinction concerns the orientation of the magnetic flux relative to the axis of rotation:

- Radial Flux PM Machines (RF-PM): The magnetic flux flows radially through the air gap, perpendicular to the rotating shaft. This represents the conventional cylindrical design, widely established in industrial and automotive applications due to its mature manufacturing technology.
- Axial Flux PM Machines (AF-PM): The magnetic flux flows axially, parallel to the shaft. These machines typically feature a disc-shaped structure. Due to their larger diameter-to-length ratio, AF-PMs offer superior torque density and compactness compared to their radial counterparts, making them particularly attractive for in-wheel or high-performance automotive traction applications.

Rotor Topology Classification: Both radial and axial flux categories can be further subdivided based on the rotor configuration:

- Surface Permanent Magnet (SPM): The magnets are mounted on the surface of the rotor iron. This is the simplest configuration to manufacture and, for a given magnet volume, provides a higher air-gap flux density compared to IPM topologies.
- Interior Permanent Magnet (IPM): The magnets are buried inside the rotor lamination (e.g., V-shaped, Spoke-type, or Bar-type). This topology offers distinct advantages, including mechanical robustness at high speeds and the ability to generate reluctance torque in addition to the magnetic alignment torque.

The classification of these topologies is systematically illustrated in the flowchart in Fig.1.3.

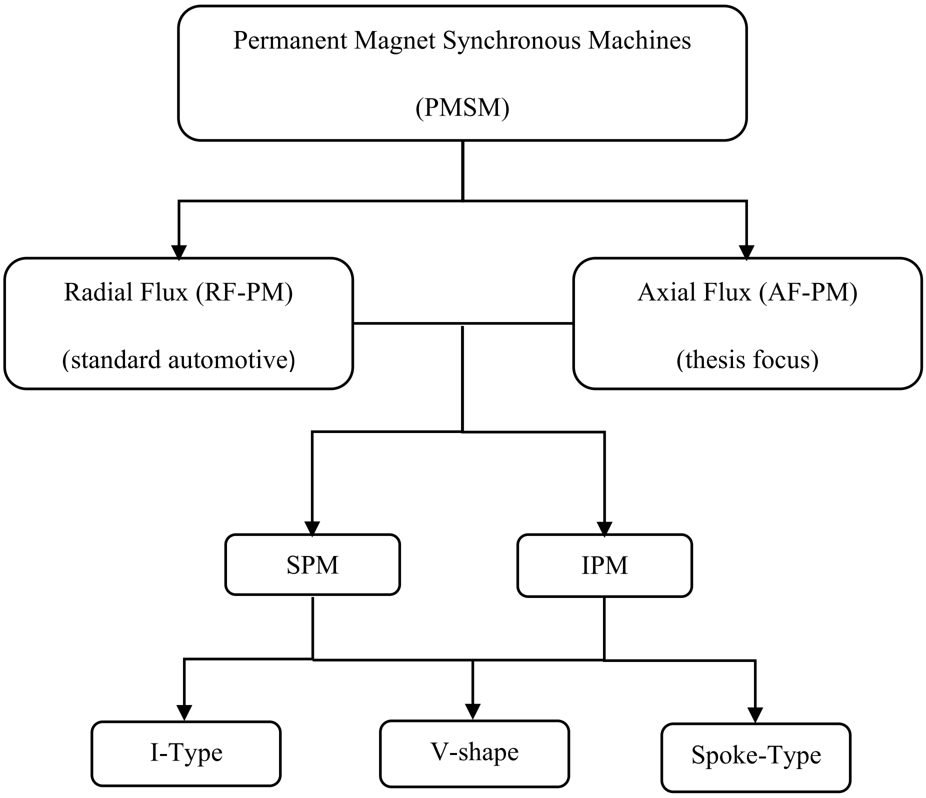

Figure 1.3 - Main PM machines topologies classification

While Radial Flux machines represent the consolidated standard in the mass-market automotive industry, this thesis focuses specifically on Axial Flux (AF-PM) topologies. The choice is driven by the increasing demand for high torque density drives where axial compactness is a critical constraint. Within the AF-PM landscape, the Surface-Mounted (AF-SPM) configuration currently represents the state of the art and is the commercially dominant solution for axial flux machines. Conversely, the Interior Permanent Magnet (IPM) configuration, specifically the V-shaped topology, is the standard for Radial Flux traction machines due to its excellent flux-weakening capabilities. However, the application of the V-shaped IPM topology to Axial Flux geometry has not yet been fully explored in scientific literature.Therefore, the primary objective of this work is to design and analyze the novel Axial Flux AF-IPM V-shaped machine and benchmark its performance against a state-of-the-art Axial Flux AF-SPM baseline under identical stator constraints.

1.3 State of the art: axial flux permanent magnet machines (AFPM)

Axial Flux Permanent Magnet (AF-PM) machines represent an attractive alternative to traditional Radial Flux (RF-PM) machines, particularly in applications demanding high torque density and compact axial dimensions. As widely reported in the literature [3], a key advantage of the AF-PM topology derives from its geometry: for a given external diameter, AF-PMs typically provide a larger active magnetic surface area compared to their radial counterparts. Consequently, they often exhibit a superior torque density. However, the planar air-gap orientation introduces a significant axial magnetic attraction force between the stator and rotor discs. In radial flux machines, magnetic forces are ideally balanced in the radial direction (canceling each other out). Conversely, in axial flux machines, this strong attractive force acts parallel to the shaft. If not properly managed, this force imposes a severe load on the mechanical structure and bearings. Consequently, while single-stage (one stator/ one rotor) configurations exist, the development of multi-stage topologies (stacking multiple stators and rotors) is primarily driven by the need to balance these axial forces internally, neutralizing the thrust on the bearings and simplifying the mechanical housing design.

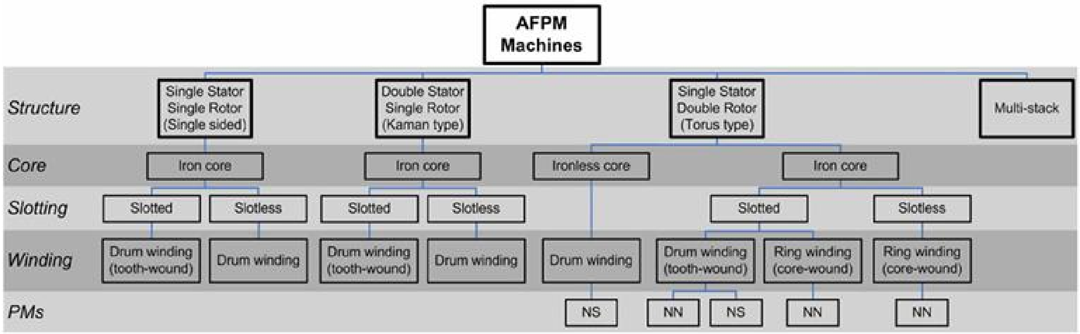

Figure 1.4 - Different topologies of AF-PM machines [4]

1.3.1 Single-Stator Single-Rotor (SSSR)

The SSSR topology, often referred to as the "pancake" machine, represents the most basic form of AF-PM machine, consisting of one stator disc and one rotor disc separated by a single air-gap. While this configuration offers the highest level of simplicity and the lowest manufacturing cost, it presents a significant mechanical challenge due to the large unbalanced axial magnetic pull between the rotor and stator. As discussed in [5] , this force requires heavy-duty bearings and an extremely rigid housing to prevent the air-gap from closing, which generally limits its use to low-power applications or environments where axial space is strictly constrained. The general layout of this structure is illustrated in Fig. 1.5.

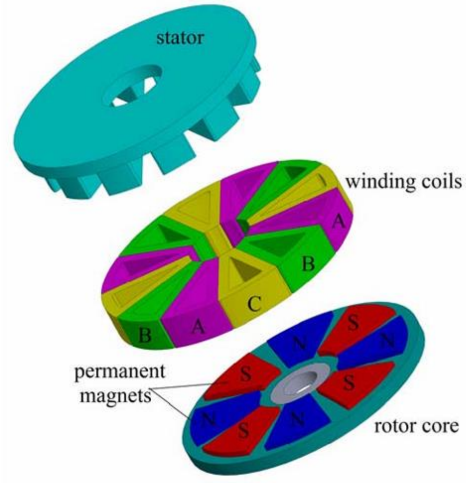

Figure 1.5 - View of a four-pole-pair/12-slot SSSR AF-PM machine [5]

1.3.2 Single-Stator Double-Rotor (SSDR)

The Single-Stator Double-Rotor (SSDR) configuration represents a significant improvement over the single-sided topology. Widely known as the TORUS topology, it is a popular choice for electric traction because it naturally balances the axial forces: since the stator is sandwiched between two rotating discs, the magnetic pull from the two external rotors cancels out, relieving the load on the bearings.

Within this category, the magnetic circuit can be designed following two distinct flux paths, leading to radically different stator structures: the TORUS-NN and the TORUS-NS configurations.

- TORUS-NN (North-North): In this configuration, magnets of the same polarity (N-N) face each other across the stator. Consequently, the magnetic flux is forced to turn 90 degrees and travel circumferentially through the stator core to complete the circuit. This arrangement requires a sufficient stator back-iron (yoke) to carry the flux without saturation.
- TORUS-NS (North-South): In this structure, magnets of opposite polarity (N-S) face each other. This allows the magnetic flux to travel straight through the stator core axially, from one rotor to the other, without traveling circumferentially along the stator. The most significant advantage of this flux path is the possibility of eliminating the stator yoke. This concept is the foundation of the YASA (Yokeless and Segmented Armature) topology. By removing the stator back-iron, the total mass is drastically reduced, and the stator can be manufactured using segmented pole pieces, significantly increasing torque density and efficiency (Fig. 1.6) [5].

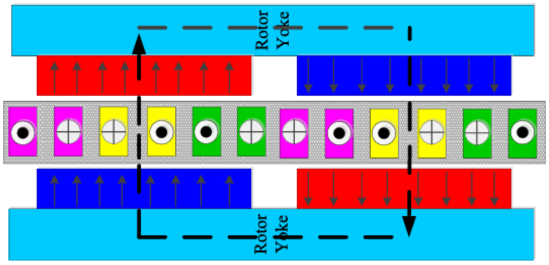

Figure 1.6 - Coreless NS TORUS structure of the AFPM machine [5]

1.3.3 Double-Stator Single-Rotor (DSSR)

The Double-Stator Single-Rotor (DSSR) configuration, also widely known as the AFIR (Axial Flux Internal Rotor) topology, places a central rotor disc sandwiched between two external stators. Mechanically, the rotor acts as a single rotating body; however, in terms of magnetic circuit, it effectively supports excitation on both axial faces. This configuration is particularly advantageous for high-torque density applications because the rotor can be designed as a lightweight disc, significantly reducing the overall inertia of the system [5]. Regarding the rotor construction, the AFIR topology can be implemented with either Surface-Mounted (AFIR-S) or Interior Permanent Magnet (AFIR-I) rotors. The Fig. 1.7 illustrates the standard AFIR-S configuration, where magnets are mounted on the surface of the rotor disc. While this structure is simpler to manufacture, it poses challenges at high rotational speeds due to centrifugal forces acting on the magnets. Consequently, the AFIR-I (IPM) variant is often preferred. By burying the magnets inside the rotor structure, the AFIR-I design provides superior mechanical robustness and eliminates the risk of magnet detachment, overcoming the structural limits of the surface-mounted topology shown in the Fig. 1.7.

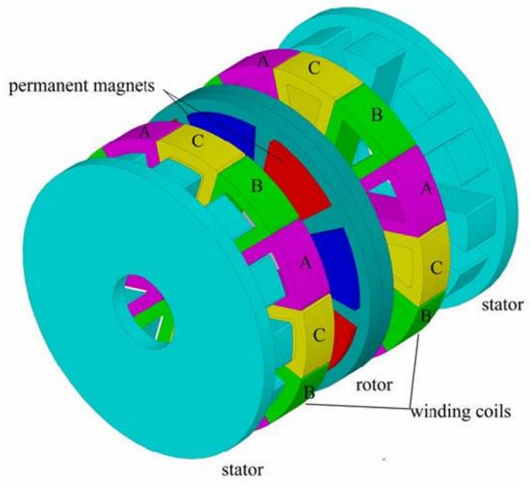

Figure 1.7 - 3-D view of a four-pole-pair/12-slot DSSR AF-PM machine [5]

1.4 Comparison between axial flux and radial flux machines

The transition from conventional electric machine designs to high-performance traction solutions requires a fundamental evaluation of how magnetic flux is directed and utilized within the machine's active volume. While the previous sections established the general state of the art for axial flux technology, it is necessary to formally compare this architecture with the more traditional radial flux standard. This comparison is crucial to highlight the geometric and torque-density advantages that justify the adoption of a disc-shaped structure over a cylindrical one, providing the necessary topological foundation before evaluating specific rotor internal configurations.

Beyond the classification based on magnet placement (IPM, SPM), an additional major distinction can be made according to the direction of the magnetic flux in relation to the rotation axis. The two main configurations are the more common radial flux machine (RFM) and the axial flux machine (AFM), which is becoming more popular for certain applications. Radial flux machines are characterized by a cylindrical structure where the magnetic flux flows radially (perpendicular to the rotation axis). This configuration is currently the most widely adopted in industrial environments and in automotive applications. Conversely, AFMs are built as stacked disc-shaped structures, where the magnetic flux flows parallel to the shaft axis as shown in Fig. 1.8. [6]

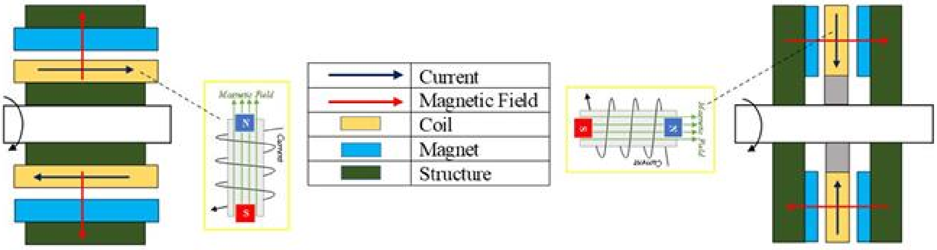

a) Radial Flux Motors **b) Axial Flux Motors**

Figure 1.8 - Basic schematic Radial Flux vs Axial Flux [7]

1.4.1 Torque Density, Geometry, and Pole Number Impact

A key parameter for traction applications, especially those with space constraints, is torque density. Here, AFM topologies show significant potential, particularly in geometrically "flat" designs. Comparative studies based on thermal constraints clearly highlight this trend. [6] While RFMs excel in long and narrow machine designs (ratio λ = Length/Outer Diameter > 1), AFMs (specifically the AFIR) become particularly advantageous for short and flat machines. In this geometric range, AFMs can deliver higher torque density compared to RFMs.

However, compact axial geometry introduces specific challenges regarding thermal management. Unlike conventional radial flux machines where the stator is located at the outer radius, enabling direct cooling via a housing water jacket, the stator in many AF-PM topologies is enclosed between rotor discs. This structural arrangement makes heat extraction from the windings more complex, often requiring advanced cooling solutions to handle high current densities [6] [7].

The sensitivity of radial flux machines to these geometric proportions is clearly illustrated in the torque density trends shown in Fig. 1.9. To ensure a fair comparison, the graph adopts a unified aspect ratio defined as the total motor axial length over its external diameter ($\lambda = L_d/D_e$), which differs from the traditional RFM definition (stator core length over rotor diameter). The graph highlights how the performance of RFMs is strictly dependent on the aspect ratio λ; specifically, it can be observed that these structures reach a high degree of utilization and are practically realizable only for low-pole machines when $\lambda > 0.5$, and for high-pole configurations when $\lambda > 0.75$. As a consequence, the curves in Fig. 1.9 are represented with dashed lines for $\lambda < 0.5$ to indicate the zone where the radial geometry becomes structurally and electromagnetically inefficient, further reinforcing the superiority of axial flux solutions in the "flat machine" region.

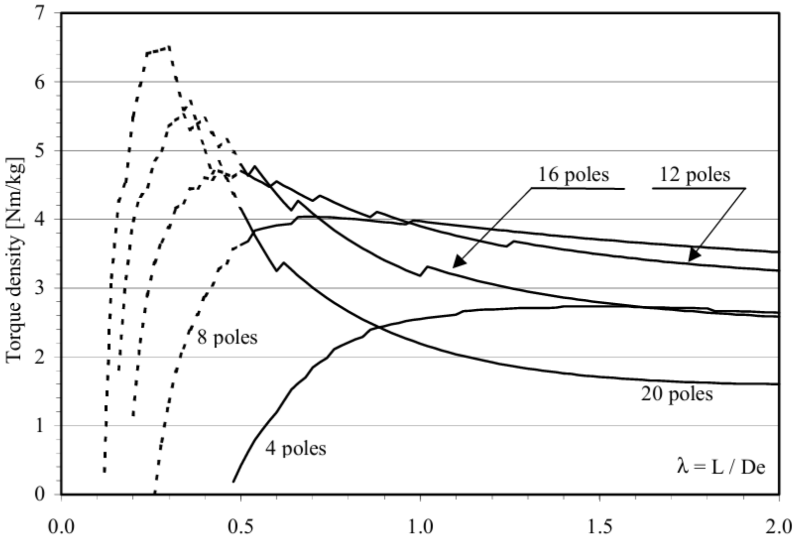

Figure 1.9 – RFMs torque density versus λ for different poles number. [6]

As shown in Fig. 1.10, in AFMs with high λ values the slots become excessively deep and the tooth too thin, which makes the structure impossible to assemble. The curves highlight an optimal geometric range for each pole configuration, with torque density dropping sharply outside this range due to constructional constraints.

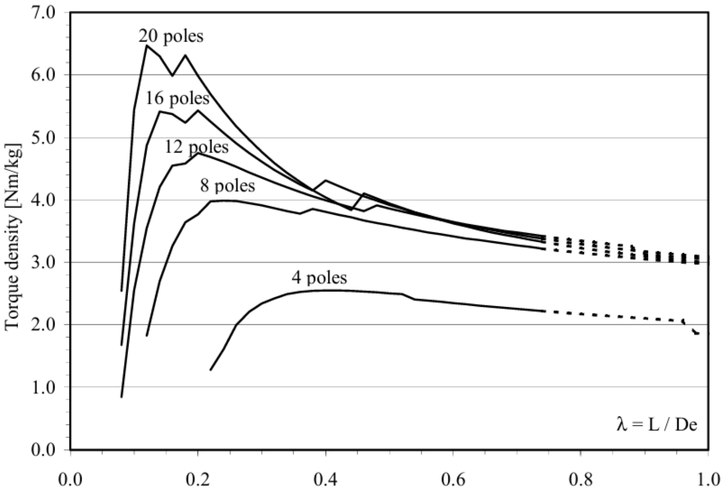

Figure 1.10 - AFMs torque density versus λ for different poles number. [6]

1.4.2 Speed Range and Field Weakening Performance

For electric traction, performance across a wide speed range is crucial, not just peak torque at low speeds. A key performance metric is the Constant Power Speed Range (CPSR), which defines the speed range over which the machine can maintain its rated power under constant voltage limits. A wide CPSR is essential as it directly impacts the vehicle's ability to sustain acceleration and reach higher cruising speeds.

A comparative study using the Finite Element Method (FEM) [7] analyzed the performance of three specific topologies designed for automotive traction applications: a Transverse Flux Machine (CPTFM), an Axial Flux Machine with Segmented Armature Torus (SAT), also known as YASA, and a conventional Radial Flux Machine (RF-PM). To ensure a meaningful comparison, the machines were designed with identical outer dimensions, identical permanent magnet mass, and subjected to the same supply limits.

The Radial Flux (RF-PM) utilizes an Embedded PM (IPM) structure, which is the industry standard for traction due to its natural flux-weakening capability. The Axial Flux (SAT) utilizes a Surface-Mounted (RF-SPM) configuration. Typically, IPM machines are superior in the field-weakening region thanks to the contribution of reluctance torque. However, this study reveals that the intrinsic benefits of axial geometry can overcome this topological disadvantage [8].

The results indicate that while the Radial Flux IPM maintains a stable constant torque up to a slightly higher base speed (3800 rpm vs 3000 rpm), the Axial Flux AF-SPM exhibits superior performance in the deep field-weakening region. As shown in Fig. 1.11, the Axial machine achieves a higher torque magnitude at high speeds compared to the Radial IPM. Consequently, as illustrated in the power curves of Fig. 1.12, the Axial topology delivers higher peak power and a broader power plateau.

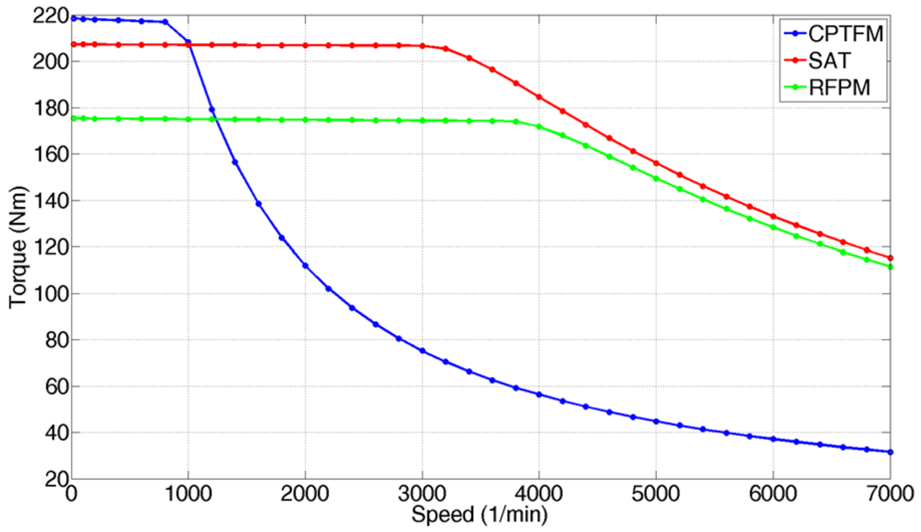

Figure 1.11 - Speed-Torque Curve of CPTFM, SAT and RF-PM (constant J) [8]

As a direct consequence of this superior torque maintenance, the AFM achieves a higher peak power and a broader power plateau compared to its radial counterpart. As illustrated in Fig. 1.12, the power-speed curves demonstrate that the AFM (SAT) does not suffer from the same rapid power drop-off as the RFM after the base speed is exceeded, providing a more consistent performance for high-speed cruising and a wider CPSR.

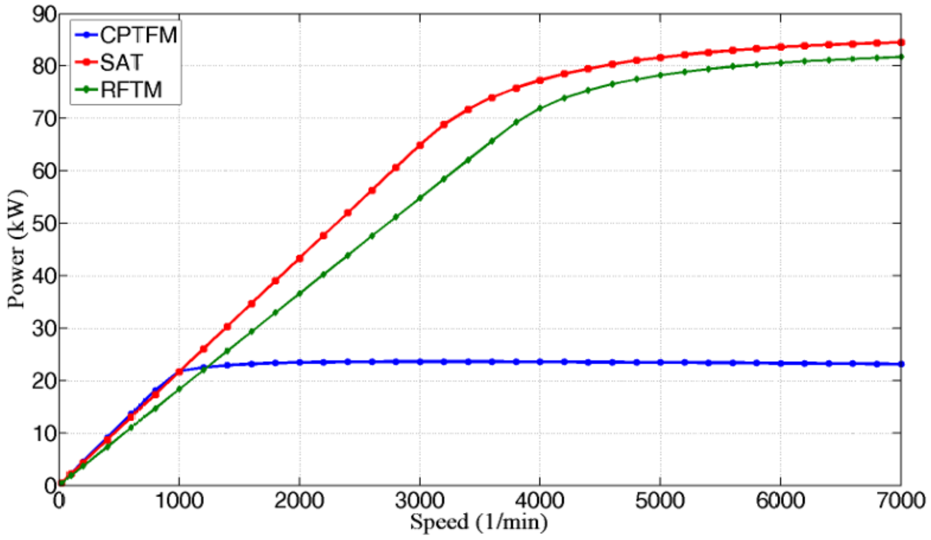

Figure 1.12 - Power vs Speed graph AFM vs RFM [8]

1.4.3 Comparative Conclusions: Axial vs. Radial Flux Technologies

The comparison analysis provides evidence that, while RFMs remain the dominant and well-understood technology for electric traction applications, AFMs possess a unique set of advantages making them increasingly competitive candidates, especially for axially compact designs. AFMs are particularly good at providing high torque density in flat geometries and hence are suitable for narrow spaces. Specific FEM studies [8] for EV applications have shown that AFMs can achieve equal or higher torque density compared to RFMs.

A critical differentiator lies in thermal management. In standard RFMs, the stator is located on the outer radius, facilitating heat dissipation via a simple water jacket. Conversely, AFMs present a distinct thermal scenario dictated by their geometry. As detailed in comparative studies [6], the performance of these machines is strictly linked to the 'wasting surface' (S_w), which represents the total area available for heat dissipation. While internal heat generation in multi stage topologies can be complex to manage, the large diameter-to-length ratio (low λ ratio) characteristic of AFMs naturally provides an extensive lateral surface area relative to the active volume [6]. If properly utilized with advanced cooling techniques, this geometric feature allows for effective handling of high current densities."

However, these performance advantages must be balanced against practical considerations, particularly manufacturability and mechanical robustness. RFMs benefit from mature and standardized production processes. AFMs can introduce significant construction challenges, such as the precise assembly of stators, the management of strong axial forces between components, and the mechanical integrity of the disc-shaped rotor at high speeds. Nevertheless, the overall performance of AFMs, in conjunction with their natural suitability for direct-drive applications, makes them a strategic technology for the future evolution of electric propulsion systems.

1.5 Comparison between radial SPM and IPM topologies

Since interior magnet technology is far more consolidated in the radial flux domain, the following sections will analyze the theoretical and performance differences between RF-SPM and RF-IPM topologies in radial flux machines. This analysis will serve as a fundamental theoretical basis to predict and justify the advantages expected when applying an IPM V-shaped rotor to the axial flux architecture.

Magnet disposition is a fundamental aspect in machine design, as it determines key aspects such as air-gap flux density, magnetic and iron losses, cogging torque, and the constant power speed range (CPSR). The scientific literature on this topic is extensive, offering numerous studies and comparisons between RF-SPM and RF-IPM machines; however, no one provides evidence that one topology is universally superior to the other. The choice of rotor type is closely related to the specific application and the operating environment. The key configurations analyzed in this study are Surface Permanent Magnet (RF-SPM), Interior Permanent Magnet I-shaped (RF-IPM I-shaped), and Interior Permanent Magnet V- shaped (RF-IPM V-shaped) as shown Fig. 1.13.

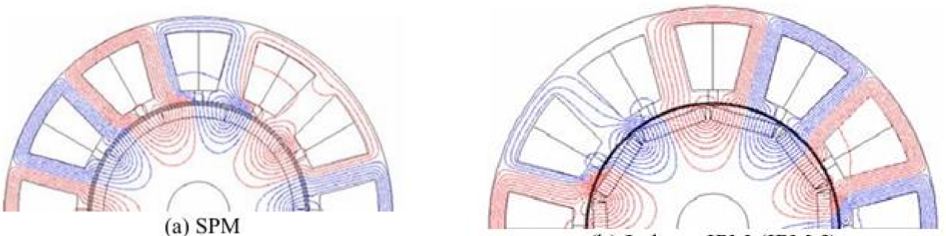

(a) SPM

(b) I-shape IPM (IPM-I)

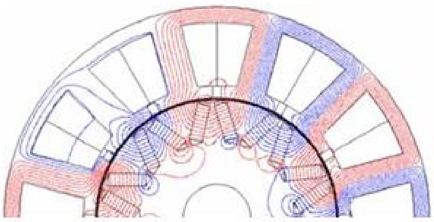

(c) V-shape (IPM-V)

Figure 1.13 - comparison of three topologies [9]

1.5.1 Mechanical Robustness and Flux-Weakening Capability

The advantages of RF-IPM designs are widely recognized in literature. Firstly, RF-IPM rotors are more robust from a mechanical perspective. The magnets are buried within the rotor iron, which provides protection from centrifugal forces at high speed and reduces the risk of magnet detachment, a known concern for surface-mounted rotors. Consequently, the manufacturing process is simplified, as it eliminates the need for highly sophisticated structural adhesives or external retaining sleeves typically required to secure surface magnets. Secondly, the specific shaping of the rotor around the embedded magnets produces magnetic saliency ($Ld \neq Lq$).

This configuration enables a significant reluctance torque contribution, which is the primary reason why RF-IPM topologies exhibit superior flux-weakening capability and a wider CPSR compared to RF-SPM designs. Specifically, a sufficiently high direct-axis inductance (*Ld*) renders the demagnetizing d-axis current component (*id*) highly effective in counteracting the permanent magnet flux. Comparative analyses show that I-shaped IPMs typically attain the largest CPSR due to their favorable magnetic parameters, followed by V-shaped IPMs (Fig. 1.14) [9].

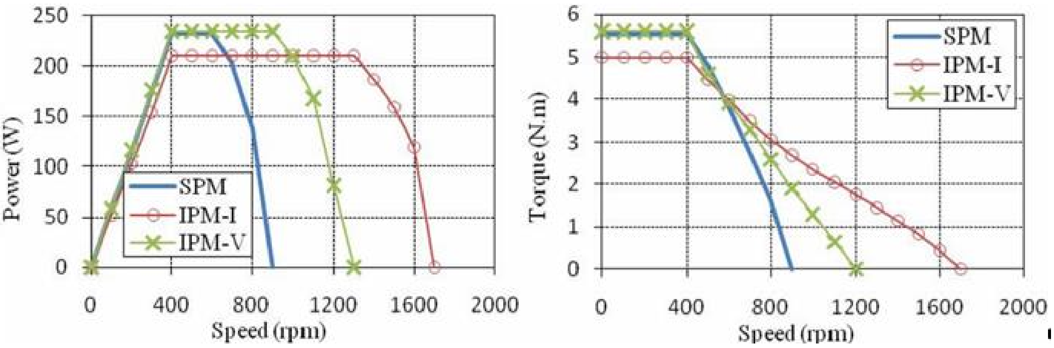

Figure 1.14- power-speed and torque-speed curve of RF-SPM, RF-IPM-I, RF-IPM-V [9]

Furthermore, the choice of stator winding significantly impacts this capability; single-layer non-overlapping windings generally yield higher *Ld* than double-layer windings, which increases the CPSR in all configurations, theoretically allowing IPMs to operate over an unlimited speed range (Figure 1.15). [10]

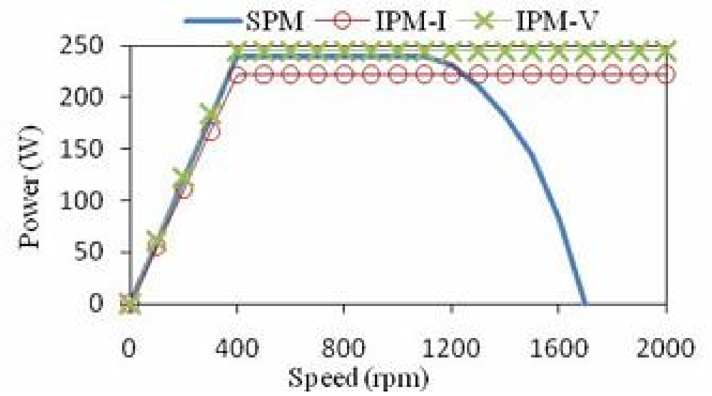

Figure 1.15 - power-curves for single layer windings [10]

1.5.2 Magnet Losses

While RF-IPMs offer clear advantages in CPSR, the analysis of losses is more complex and highlights the sensitivity of the design. A key advantage of the RF-IPM topology is the reduction of magnet losses. In an RF-SPM, the magnets are directly exposed to the armature reaction field, inducing eddy currents. In RF-IPM machines, the rotor iron serves as a magnetic shield that protects the embedded magnets. This shielding effect improves efficiency while mitigating magnet heating, thus lowering the risk of thermal demagnetization. [9]

As demonstrated by the authors in [9], magnet segmentation is a highly effective technique to further mitigate these losses by interrupting eddy-current paths. The V-shaped configuration naturally introduces segmentation, since each pole is formed by two magnet pieces, which helps reduce overall magnet losses. A RF-IPM I-shaped, if artificially segmented, can achieve even lower magnet losses than the V-shaped, benefiting from both segmentation and the superior shielding effect associated with its high *Ld*.

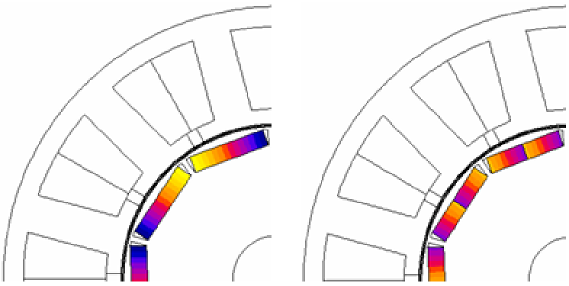

(b) Non-segmented I-shape IPM (e) Segmented I-shape IPM

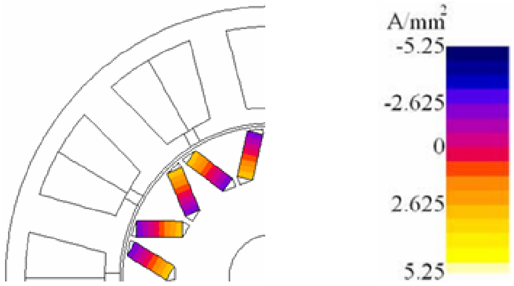

(c) Segmented V-shape IPM (f) Current density scale

Figure 1.16 - full load current at the rated speed of segmented magnets and non-segmented magnets [9]

1.5.3 Iron Losses (Core Loss)

The literature reports conflicting trends for iron loss, indicating this metric is highly dependent on winding configuration, harmonic content, and the specific operating point. Comparative analyses of fractional-slot machines reveal that RF-IPM configurations suffer from higher iron losses under load compared to RF-SPM alternatives [9]. The explanation provided is that the armature reaction field in these specific RF-IPMs has higher harmonics, increasing the alternating flux components in the iron. Conversely, when employing distributed windings the RF-SPM machine had the highest iron loss, while the conventional RF-IPM and V-shaped designs showed significantly lower losses [11] . This divergence highlights that iron loss depends on air-gap flux density profile, stator winding topology, magnet depth, harmonic content, and local iron saturation. Studies show that single-layer windings tend to increase iron losses compared to double-layer windings due to larger air-gap flux density sub-harmonics [9].

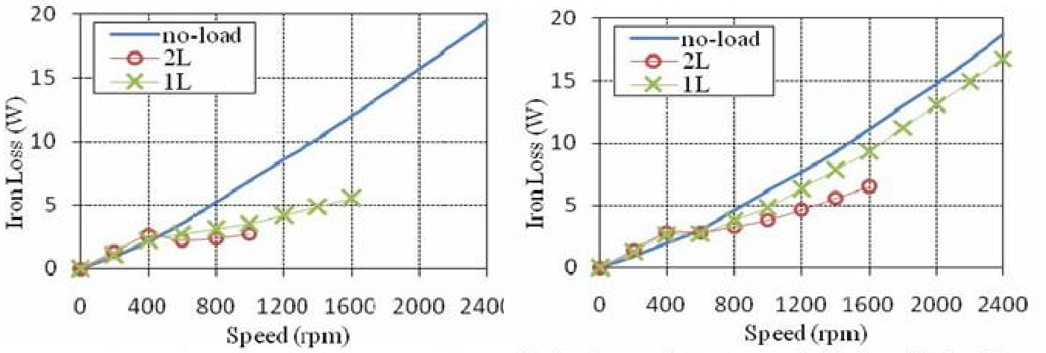

(a) Iron loss against rotor speed of SPM machines (c) Iron loss against rotor speed of I-shape IPM machines

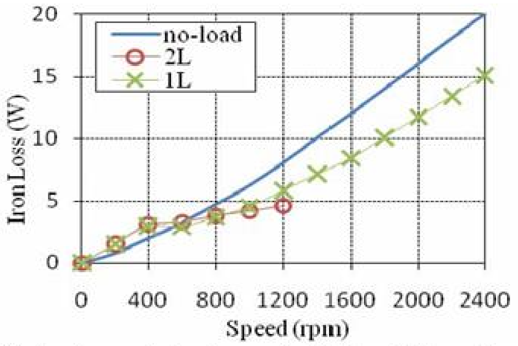

(e) Iron loss against rotor speed of V-shape IPM machine

Figure 1.17 - Iron loss of RF-SPM, RF-IPM-I, RF-IPM-V [9]

1.5.4 Performance comparison (torque, ripple, demagnetization)

Regarding torque production, [10] shows that RF-IPM V-shaped machines, through optimization of parameters like the magnet angle (α) and magnet thickness, can achieve torque levels comparable to RF-SPM machines, using both magnet and reluctance torque. However, RF-IPM I-shaped designs may struggle to have the same torque output as RF-SPM or RF-IPM V-shaped due to geometric constraints limiting magnet volume. RF-IPM machines are also noted to suffer more significantly from the cro**ss-**coupling effect where q-axis armature reaction reduces the d-axis PM flux linkage compared to RF-SPM machines [10]. The air-gap flux density under no-load conditions tends to be highest in RF-SPM machines because the magnets are closer to the air gap, whereas RF-IPMs show lower values due to the magnets being embedded.

Cogging torque and torque ripple are strongly influenced by magnet shape, pole arc, slot openings, and the interaction between rotor poles and stator slots. In particular [10] reported the lowest cogging torque for the IPM-I configuration and the highest for the RF-IPM-V within a specific 10-pole/12-slot design. However, [11] found a RF-IPM-I design resulted in lower cogging torque than a RF-IPM V-shaped within an 8-pole/24-slot machine.

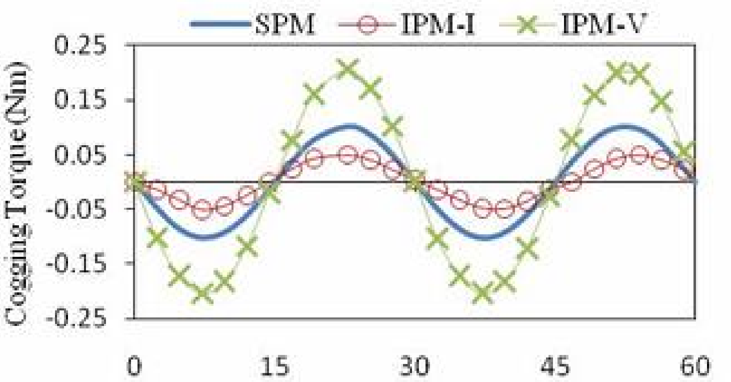

Figure 1.18 - comparison of cogging torque

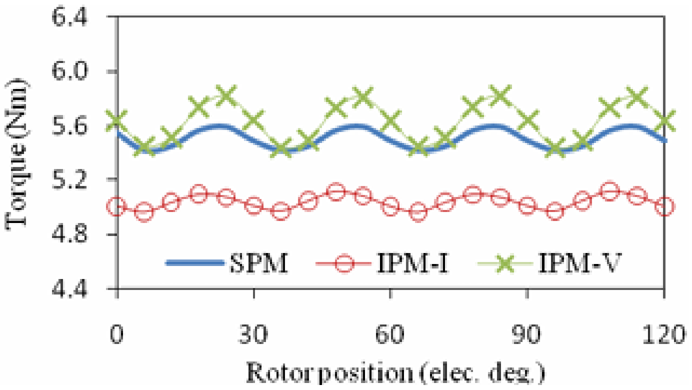

Figure 1.19 - torque for machines with double layer windings [10]

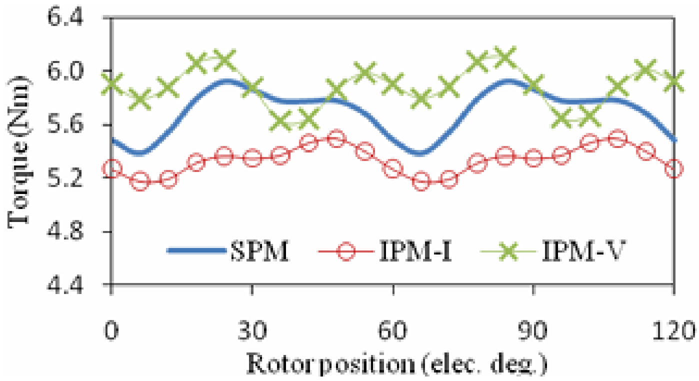

Figure 1.20 - torque for machines with single layer windings [10]

Finally, demagnetization risk depends on local magnet temperature (influenced by magnet losses) and the peak opposing armature reaction field. [11] indicated that under specific full-load conditions, a conventional RF-IPM showed a higher risk of demagnetization compared to the RF-SPM and V-shaped designs in that comparison. The extensive analysis of radial flux topologies confirms that the RF-IPM configuration, particularly the V-shaped, offers a superior balance between high-speed capabilities (CPSR), efficiency, and mechanical reliability compared to RF-SPM designs.

1.6 Comparison between axial flux IPM and SPM

Transposing the advantages of the Radial Flux IPM topology into the Axial Flux domain is not straightforward due to the complex 3D flux paths and manufacturing constraints of disc-shaped rotors. Consequently, the next section will focus on a specific novel topology, the Axial Flux V-shaped IPM. Currently, the literature regarding Axial Flux machines with V-Type Interior Permanent Magnet configurations is remarkably limited. While Interior Permanent Magnet concepts have been explored in the axial domain, most existing studies and prototypes reported in literature adopt the Spoke-Type configuration. Conversely, the V-Shaped topology despite being the established industry standard for high performance Radial Flux traction machines remain largely unexplored in the Axial Flux context. Driven by this gap in the state of the art, this work aims to investigate this specific topology.

1.6.1 Structural Differences and Mechanical Integrity

The study conducted in [1] proposes a novel Axial Flux Interior Permanent Magnet (AF-IPM) machine featuring a V-shaped magnet arrangement. In this topology, the permanent magnets are embedded within the rotor core at a specific inclination angle to exploit reluctance torque and achieve an extended speed operating range. As shown in Fig. 1.21, this configuration requires a thicker rotor back-iron to accommodate the V-shaped magnets, which also helps reduce magnetic saturation for improved efficiency. Although embedding the magnets slightly increases the overall rotor mass, it provides intrinsic mechanical retention against centrifugal forces, eliminating the need for additional sleeves and reducing the risk of magnet detachment at high speeds. Furthermore, the V-shaped configuration allows the machine to achieve a high saliency ratio while simultaneously maintaining a high airgap flux density.

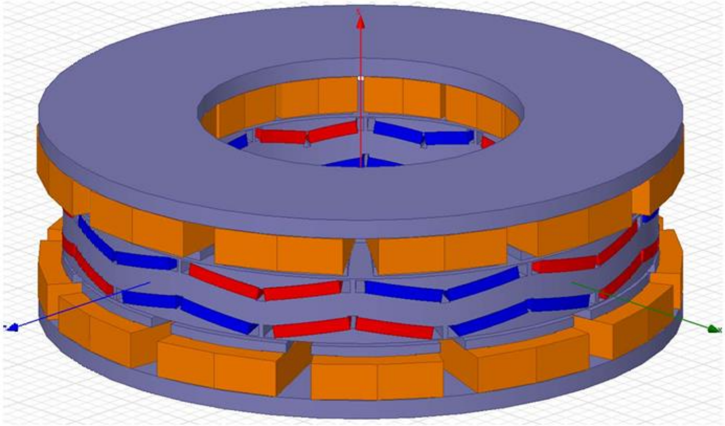

Figure 1.21 - Proposed AF-IPM V-shape [1]

1.6.2 Machine Specifications and Design Constraints

To evaluate the effectiveness of the V-shaped IPM topology, the reference study [1] defines a set of specifications for a traction application. The goal is to design a 5.75 kW machine with a rated speed of 2000 rpm. These target values, along with the electrical and thermal constraints, are summarized in Table 1.2.

The design is limited by a maximum current of 19 A RMS and a nominal DC bus voltage of 400 V. From a thermal perspective, the machine is expected to be cooled via a cooling jacket, which limits the allowable current density to 9 A/mm². These constraints are particularly challenging for axial flux machines, where the limited axial length and outer diameter restrict the space available for active materials.

Regarding the materials selected for the study, high-remanence NdFeB (Br = 1.21 T) magnets are used. The stator and rotor cores are designed using M270 35A silicon steel laminations, specifically employing toroidal tape wound cores to optimize the flux path and reduce iron losses at high frequencies.

Table 1.2 – Reference machine specifications

Parameter	Value
Magnet	NdeFeB 35 SH
Operation mode	Continuous
Current density	9 A/mm2
Rated Power	5.75 kW
Rated Speed	2000 rpm
Max Irms used	19 A
Nominal Voltage	400 V
Cogging Torque Max	1 Nm (peak to peak)

1.6.3 Magnetic Saliency and Torque Production Mechanism

The most critical electromagnetic distinction between the V-shaped AFM and the AF-SPM counterpart is the introduction of magnetic saliency. In a standard AF-SPM, the direct-axis inductance (L_d) and quadrature-axis inductance (L_q) are identical because the surface magnets behave magnetically like air, resulting in an isotropic rotor structure. Conversely, the IPM-V geometry creates preferential paths for the magnetic flux, leading to a difference between inductances ($L_q > L_d$).

This anisotropy fundamentally changes the torque production mechanism. As described by the general torque equation (1.1) for synchronous machines, the total electromagnetic torque is the sum of two distinct components:

$$T = \frac{3}{2}\, p\, \lambda_{pm}\, I_q + \frac{3}{2}\, p\, \left(L_d - L_q\right) I_d\, I_q \tag{1.1}$$

Where PM Torque (Alignment Torque) is:

$$\mathrm{T}_{pm} = \frac{3}{2}\, p\, \lambda_{pm}\, I_q \tag{1.2}$$

This component represents the interaction between the permanent magnet flux linkage (λ_{pm}) and the q-axis stator current, and the Reluctance Torque is:

$$T_{rel} = \frac{3}{2}\, p\, (L_d - L_q)\, I_d\, I_q \tag{1.3}$$

In an AF-SPM machine, since Ld ≈ Lq, the second term (Reluctance Torque) is negligible. The torque is almost entirely generated by the interaction between the magnet flux and the q-axis current (I_q). In the IPM-V topology, the term (L_d - L_q) is non-zero and significant. This implies that the machine can exploit the Reluctance torque component.

It is important to note that the presence of reluctance torque does not necessarily imply a higher total peak torque compared to an AF-SPM design, especially if the volume of magnets is reduced or if the magnets are placed deeper within the rotor. However, it provides a strategic advantage in control flexibility. By injecting a negative I_d current (Maximum Torque Per Ampere - MTPA strategy), the AF-IPM V-shaped can generate a portion of its torque from the rotor's iron saliency.

1.6.4 Geometric Parameters

The performance of the AF-IPM V-shaped axial flux machine is highly sensitive to the geometric configuration of the rotor. To optimize the saliency ratio and protect the magnets, three main parameters are analyzed: the V-angle (alpha), the flux barriers, and the mechanical ribs (or bridges).

- V-angle (α_m) : This is the angle between the two magnet segments forming a pole. A smaller angle tends to increase the flux concentration effect and the machine anisotropy, but requires a thicker rotor disc. The choice of alpha is a trade-off between maximizing the fundamental air-gap flux density and managing the d-axis inductance.
- Flux Barriers (W_{fb}): At the ends of the V-shaped magnets, small air pockets (barriers) are designed to minimize magnetic leakage. Without these barriers, a significant portion of the magnet flux would circulate internally within the rotor iron instead of crossing the air-gap to link with the stator windings [1].
- Mechanical Ribs (Dg, Dm): These are the thin iron sections that remain between the magnets and the rotor outer/inner diameters. As reported in [1] they are essential for the structural integrity of the disc at 2000 rpm, they

must be as thin as possible to ensure magnetic saturation, thereby limiting the leakage flux.

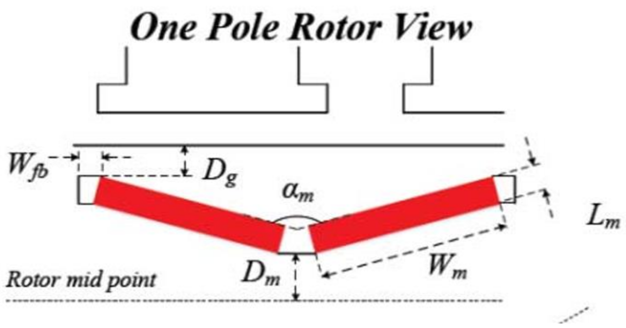

Figure 1.22 - machine geometric parameters [1]

1.6.5 Magnetic Flux Distribution

The 3D nature of the axial flux machine requires a careful analysis of the flux paths. In the DSSR (Double-Stator Single-Rotor) configuration, the flux generated by the V-shaped magnets travels axially through the air-gap, enters the stator teeth, and returns through the toroidal stator core. Inside the rotor, the V-shaped creates a "flux focusing" effect. The flux lines are squeezed toward the pole center, increasing the air-gap flux density. As illustrated in Fig. 1.23, the flux distribution shows that the iron poles between the V-magnets are designed to be highly permeable paths for the q-axis flux, while the magnets themselves present a high reluctance to the d-axis flux, effectively creating the saliency (Lq > Ld) discussed in the previous section. This visualization confirms that the flux barriers successfully direct most of the magnetic field into the active air-gap area.

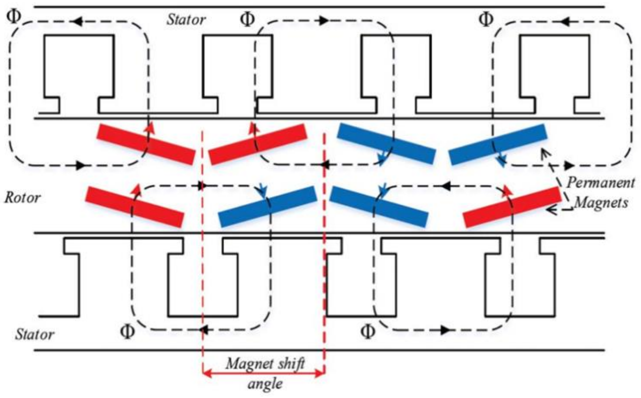

Figure 1.23 - Illustration of flux directions of the proposed AF-IPM V-shaped [1]

2 Comparison criteria and modeling of AF-SPM and AF-IPM

The primary objective of this chapter is to present the design process and the numerical modeling of the two axial flux machines. To ensure a fair and direct comparison, both machines are studied using the exact same stator structure and identical operating conditions, sharing the same supply current, DC bus voltage, winding layout and the same pole arc ratio of permanent magnet material.

It is important to note that while the pole arc ratio and magnet thickness (h_{pm}) are kept identical, the internal placement of the magnets in the AF-IPM V-shaped configuration results in a slightly smaller radial dimension because the magnets are buried within the rotor disk. Consequently, the total volume of permanent magnet material in the AF-IPM model is approximately 5% lower than in the AF-SPM benchmark. This approach ensures that any performance difference found during the analysis is strictly due to the different placement of the magnets within the rotor (surface-mounted vs. interior V-shaped).

2.1 Geometric Modeling and Parameterization

The development of the numerical models in Altair Flux 3D is based on a set of predefined geometric and electrical specifications. Instead of performing preliminary sizing from scratch, this study adopts a validated Surface-Mounted Permanent Magnet (AF-SPM) machine as the reference baseline. The design choices regarding the AF-IPM rotor, such as the V-angle of the magnets and the rotor disk thickness, are based on the reference work [1] and the current scientific literature on axial flux AF-IPM machines. The following Table 2.1 lists the design parameters for the benchmark AF-SPM configuration. Since both machines share the same stator and supply conditions, these values also represent the fixed constraints maintained for the AF-IPM model.

Table 2.1 – Reference machine Specifications

Parameter	Symbol	Unit	Value
Number of stator slots	Nc	-	18
Number of pole pairs	pp	-	6
Rated power	Pn	kW	16.1
Rated speed	nnom	rpm	2730
Rated torque	Tn	Nm	53.3
DC bus voltage	Vdc	V	400
Current density	J	A/mm2	7.4
Stator inner diameter	D1	mm	125.7
Stator outer diameter	D2	mm	217.7
Height yoke stator	hys	mm	12.2
Height slot edge	hes	mm	1
Height slot link	hls	mm	1
Width slot opening	wso	mm	5
Width slot	ws	mm	10.7
Inner tooth width	wt1	mm	11.1
Outer tooth width	wt2	mm	27.2
Height tooth slot	hts	mm	45.3
Air-gap Thickness	hgap	mm	1
Height permanent magnet	h_pm	mm	5
Slot pitch	tau_s	mm	29.9
Pole pitch	tau_p	mm	44.9
Pole arc ratio	alpha_pm	%	0.7
Phase resistance	Rphase	Ω	0.045
N.of conductors per phase	Zph	-	144
Copper area in the slot	Acu	mm2	75
Slots per pole per phase	q	-	0.25
Winding layout	wdg	-	conc
Winding layer	wdgl	-	double

2.2 Geometric Modeling and periodicity

The design and electromagnetic characterization of the two axial flux machines were carried out using **Altair Flux 3D,** a Finite Element Method (FEM) software dedicated to the simulation of low-frequency electromagnetic and thermal phenomena. Regarding the modeling dimensionality for Axial Flux Surface-Mounted (AF-SPM) machines, 2D approximations can yield sufficiently accurate results with reduced computational cost. However, the same validation does not currently exist for Axial Flux Interior Permanent Magnet (AF-IPM) configurations. The complex leakage paths and local magnetic saturation phenomena inherent to buried magnets might be underestimated by a 2D simplification. Therefore, to ensure a rigorous comparison and capture all non-linear effects, a full 3D Finite Element Analysis was selected for both topologies. In this study, the software is used to build a fully parametric model. This approach ensures that any modification to the design specifications can be automatically propagated throughout the entire model, allowing for rapid iterations and optimization. To optimize the computational efficiency of the FEA simulations, the machine is not modeled in its entirety. Instead, only a representative sector of the machine is analyzed, based on its geometric and magnetic periodicity. The machine features a double-layer concentrated winding with Nc = 18 slots and p = 12 poles. By utilizing the **Emetor** [12] analytical tool, the periodicity of this specific combination was identified. As illustrated in the winding diagram provided by Emetor [12] in Fig. 2.1, the fundamental periodicity of the machine is equal to 6. Consequently, it is possible to represent and simulate only a 1/6 sector of the machine. This reduction significantly decreases the number of nodes and elements in the mesh, leading to faster solving times while maintaining full accuracy in the characterization of the electromagnetic behavior for both the AF-SPM and AF-IPM configurations.

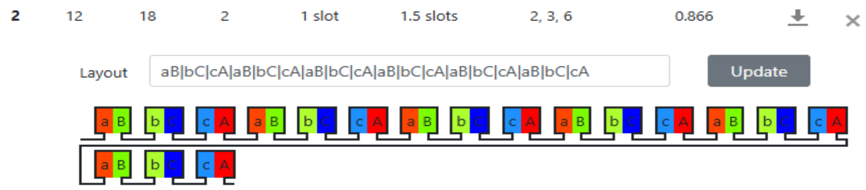

2 12 18 2 1 slot 1.5 slots 2, 3, 6 0.866

Layout aB|bC|cA|aB|bC|cA|aB|bC|cA|aB|bC|cA|aB|bC|cA|aB|bC|cA

Figure 2.1 - Winding layout [12]

2.2.1 3D model geometric parameters

Before proceeding with the geometric construction, it is necessary to define the set of symbolic parameters within the Altair Flux environment. These variables represent the mathematical link between the initial sizing data and the 3D model.

The following Fig. 2.2 illustrates the complete list of parameters used for the AF-IPM model. It should be noted that the AF-SPM configuration utilizes a subset of these parameters.

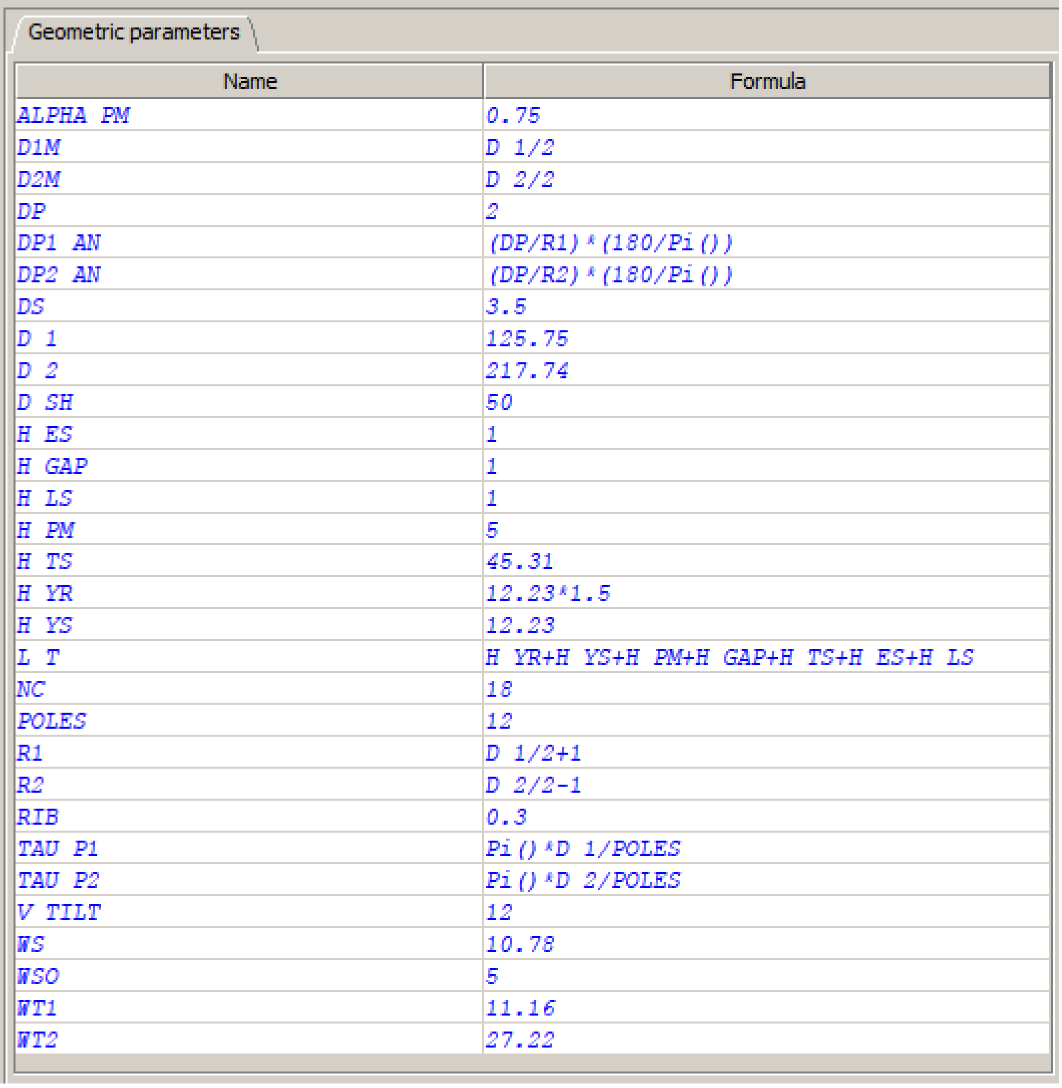

Name	Formula
ALPHA PM	0.75
D1M	D 1/2
D2M	D 2/2
DP	2
DP1 AN	(DP/R1)*(180/Pi())
DP2 AN	(DP/R2)*(180/Pi())
DS	3.5
D 1	125.75
D 2	217.74
D SH	50
H ES	1
H GAP	1
H LS	1
H PM	5
H TS	45.31
H YR	12.23*1.5
H YS	12.23
L T	H YR+H YS+H PM+H GAP+H TS+H ES+H LS
NC	18
POLES	12
R1	D 1/2+1
R2	D 2/2-1
RIB	0.3
TAU P1	Pi()*D 1/POLES
TAU P2	Pi()*D 2/POLES
V TILT	12
WS	10.78
WSO	5
WT1	11.16
WT2	27.22

Figure 2.2 - Flux AF-IPM parameters

The goal was to achieve an optimal parameterization that allows the model to be easily adapted to different geometric variations. These additional parameters are the key to the AF-IPM machine:

- DP (Inter-polar Iron Thickness): Defines the thickness of the iron bridge between two adjacent rotor poles. It is expressed as an arc length in millimeters, maintained constantly from the inner to the outer diameter.
- DP1_AN and DP2_AN: Support parameters used for the analytical definition of the geometric points during the construction phase in Flux 3D.
- DS (Inter-polar Distance): Angle between magnets of different polarity, effectively considering the sum of the iron bridge (DP) and the flux barriers (WFB).
- WFB (Flux Barrier Width): The width of the flux barriers is defined by the angular difference between DS and DP for both the inner and outer radius. While DS remains constant along the diameter, the flux barrier width varies with the radius. This choice was made because the barrier width has minimal influence on the overall performance, as noted in the reference study [1].
- R1 and R2 (inner and outer magnet radius): These parameters define the radial boundaries of the magnets. Since the magnets are buried within the rotor core, the inner radius (R1) is increased, and the outer radius (R2) decreased compared to the disk boundaries. Modifications to R1, R2, and DS lead to significant changes in machine behavior due to the varying ratio of iron to permanent magnet material.
- RIB (Mechanical Bridge Width): This is the width of the iron bridge interposed between the magnet corners and the air-gap. A smaller RIB value increases the air-gap induction; however, its minimum value is limited by mechanical stress constraints.
- V_tilt: This parameter defines the relative inclination of the magnets with respect to the XY plane, effectively setting the V-angle of the interior architecture. A tilt angle of 12° was selected, consistent with the optimal configuration in the reference study. Since the geometry of this machine differs from the reference, a full sensitivity analysis would be required to

determine the absolute optimum. As this is beyond the scope of the thesis, the literature-validated value is adopted as a robust initial design parameter.

- H_YR: The rotor yoke thickness increased by 50% compared to the AF-SPM benchmark to prevent excessive magnetic saturation caused by the flux-concentrating V-shaped magnets, thereby preserving efficiency and torque capability.

2.2.2 Coordinate Systems

The transition from symbolic parameters to a 3D geometric model requires a precise definition of reference frames. The origin (0,0,0) of the global environment is placed at the geometric center of the machine, specifically at the center of the air-gap. All other components are positioned relative to this point using specific coordinate systems and transformations.

To simplify the assembly and movement of the machine, several coordinate systems were established:

- ROTOR_MAIN and STATOR_MAIN: These are the primary cylindrical reference frames. ROTOR_MAIN is located at (0,0, h_gap/2) and is attached to the rotating part, while STATOR_MAIN is positioned at (0,0, -h_gap/2) for the stationary part.
- MAG_GLOBAL_CART: A global Cartesian system located at (0,0, h_gap/2 + RIB), rotated around the Z-axis by the distance DS.
- MAG_LOCAL_CYL_TILT: This is a local cylindrical system anchored to MAG_GLOBAL_CART and tilted by the angle V_tilt relative to the X-axis. This coordinate system is used to define the specific inclination of the interior magnets.
- MAG_GLOBAL_CART_TILT: A reference system located at (0,0, h_gap/2 + RIB) and tilted with respect to both X (by V_tilt) and Z (by DS). This system is specifically designed to handle the PM_transl transformation, which defines the upper face of the buried magnet.

2.2.3 Geometric Transformations

Geometric transformations are used to automate the construction and ensure the periodicity of the 60° sector. The most significant transformations implemented include:

- Rotational Transformations (ROT_STATOR and ROT_ROTOR): These allow the generation of the periodic structure from a single elementary component. ROT_STATOR applies a rotation of 360/Nc to define the stator slots, while ROT_ROTOR uses 360/p to position the poles.
- Translational Transformations: Various translations along the Z-axis are used to "extrude" 2D sketches into 3D volumes, defining the axial depth of the core, the magnets, and the yokes.
- Affine Transformation (MAG_MIRROR): Only for the AF-IPM V-shaped rotor, it utilizes an affine transformation with respect to a plane defined by three points. This plane is transversal to the XY plane and bisects the pole, allowing for the perfect mirrored creation of the two magnets with the same polarity, ensuring a perfectly symmetrical V-shape.

The combination of coordinate systems and geometric transformations allows the generation of the machine skeleton in Altair Flux 3D. A 60° periodic stator–rotor sector is reconstructed using points and lines only, forming the wireframe foundation for faces and volumes (Fig. 2.3 and Fig. 2.4).

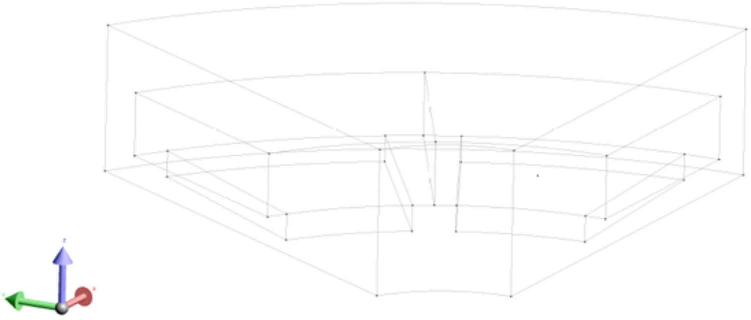

Figure 2.3 – 3D sketch of the AF-SPM

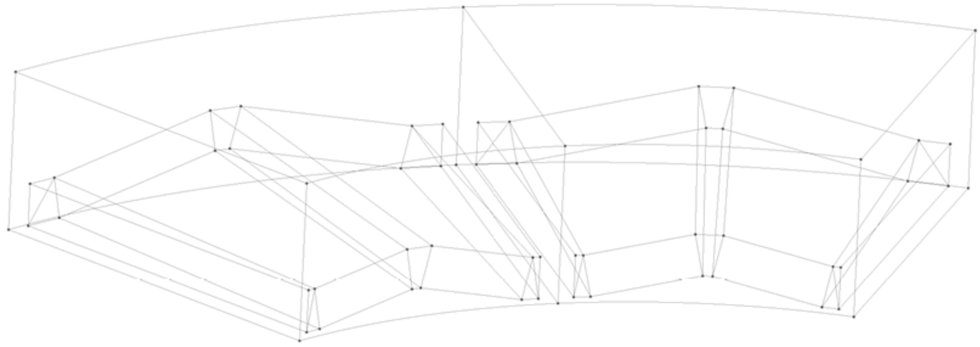

Figure 2.4 - 3D sketch of the AF-IPM V-shaped

The geometric wireframe models include auxiliary points and lines extending beyond the rotor iron and magnets to define a surrounding air region. This volume is essential for accurately modeling the magnetic flux in the space around the rotor. A similar air region is included in the stator model (Fig. 2.5). During assembly, the stator and rotor air regions are joined at the air-gap, ensuring electromagnetic field continuity over the 60° sector.

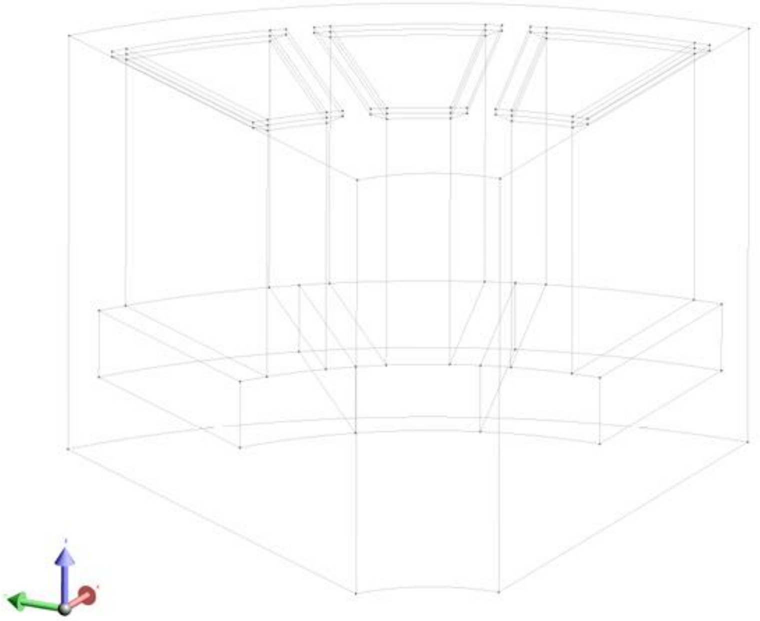

Figure 2.5 - 3D sketch of the Stator

2.2.4 Volume Generation, Physics Assignment, Magnetization

Once the point and line representation is completed, Altair Flux 3D automatically generates the corresponding faces and volumes. Each volume must be assigned to a specific Physical Region, which defines the material properties and the electromagnetic behavior of that component.

AF-SPM and AF-IPM configurations share the same materials and stator properties:

- AIR_ROTOR and AIR_STATOR: These regions are assigned the properties of air. They represent the surrounding environment and, most importantly, the air-gap.
- STEEL_STATOR and STEEL_ROTOR: These regions represent the ferromagnetic cores. They are defined as *Laminated Magnetic Non-Conducting* regions. The material chosen for both machines is M19 steel. To accurately model the physical construction, a stacking factor of 0.95 is applied. In Flux 3D, the lamination effect is simulated by assigning “cylindrical lamination" property to the magnetic region.
- INFINITE: This region is assigned to the outermost volume (the Infinite Box). As shown in Fig. 2.6, this specialized region is indispensable for correctly simulating the magnetic flux behavior at the boundaries of the domain, allowing the field to decay naturally and ensuring accurate results.

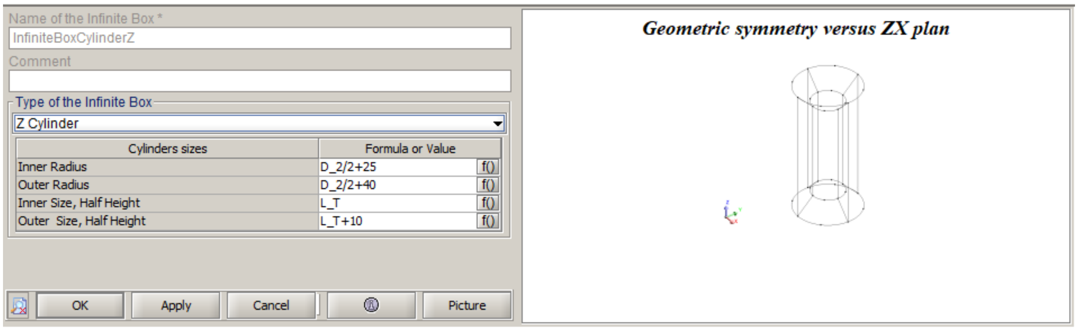

Name of the Infinite Box *
InfiniteBoxCylinderZ
Comment

Type of the Infinite Box
Z Cylinder

Cylinders sizes	Formula or Value
Inner Radius	D_2/2+25
Outer Radius	D_2/2+40
Inner Size, Half Height	L_T
Outer Size, Half Height	L_T+10

Figure 2.6 - Infinity box

PM_NORTH and PM_SOUTH: These are defined as *Magnetic Non-Conducting* regions using TEXA_MAGNET as the material. For the AF-SPM configuration, the magnetization is purely axial (Fig. 2.7):

- PM_NORTH (represented in red): Magnetization oriented at 0° relative to the ZX plane.
- PM_SOUTH (represented in blue): Magnetization oriented at 180° relative to the ZX plane.

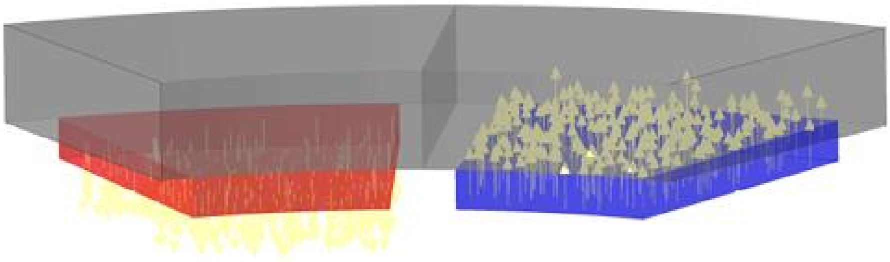

Figure 2.7 – AF-SPM: PM_NORTH and PM_SOUTH magnetization

The interior magnet configuration requires additional regions to manage the flux-concentration effect and the complex V-shaped geometry:

- BARRIER_FLUX: This region, exclusive to the AF-IPM model, represents the air-filled pockets inside the rotor. These flux barriers are strategically placed to increase the magnetic reluctance in specific paths, effectively "squeezing" and directing the magnetic flux toward the air-gap to enhance the saliency and the torque density of the machine.
- PM_NORTH (1 & 2) and PM_SOUTH (1 & 2): Due to the V-shape, four distinct regions are necessary to correctly define the magnetization. Each magnet segment must have its magnetization vector tilted by the V_tilt angle relative to its local coordinate system (Fig. 2.8).

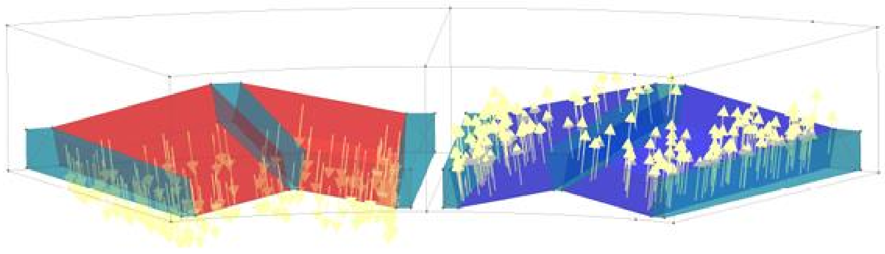

Figure 2.8 – AF-IPM: PM_NORTH (1 & 2) and PM_SOUTH (1 & 2) magnetization

This ensures that the magnetization remains perpendicular to the magnet's face, as shown in the Flux schematic below:

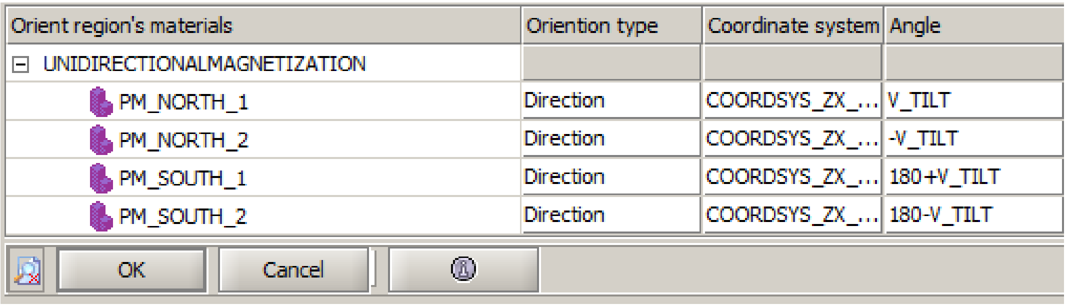

Orient region's materials	Oriention type	Coordinate system	Angle
⊟ UNIDIRECTIONALMAGNETIZATION			
PM_NORTH_1	Direction	COORDSYS_ZX_...	V_TILT
PM_NORTH_2	Direction	COORDSYS_ZX_...	-V_TILT
PM_SOUTH_1	Direction	COORDSYS_ZX_...	180+V_TILT
PM_SOUTH_2	Direction	COORDSYS_ZX_...	180-V_TILT

Figure 2.9 - IPM Magnetization settings

With the complete definition of the geometry, material properties, and magnetization strategies, the virtual prototypes of the AF-SPM and AF-IPM machines are fully characterized. The model thus evolves from a purely geometric description into a functional electromagnetic system.

Fig. 2.10 illustrates this final configuration, displaying the complete machine assembly:

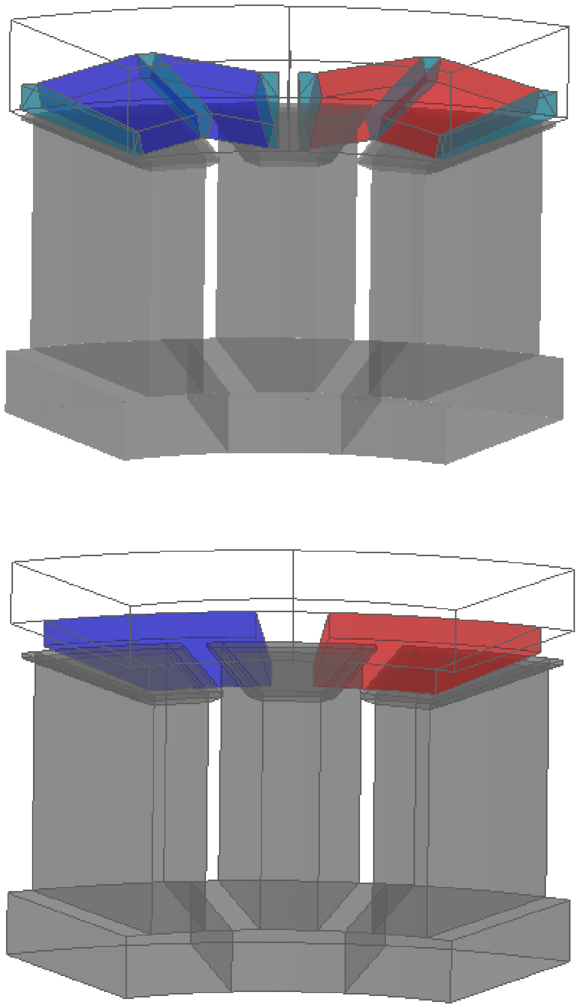

Figure 2.10 – 1/6 sector 3D model of the AF-SPM and AF-IPM V-shaped

2.3 Air-gap flux density evaluation

The first stage of the numerical evaluation is the Static Magnetic Analysis. This study is conducted with zero stator current, focusing exclusively on the magnetic field distribution generated by the permanent magnets. This analysis is fundamental to validate the flux-concentration effect of the AF-IPM V-shaped topology and to characterize the air-gap induction profile before proceeding to dynamic simulations.

The static analysis is performed using a multi-position static scenario. The rotor is moved from 0° to 60° with a step size of 30°. This angular span corresponds to one complete electrical period of the machine.

To implement this movement within the software, specific Mechanical Systems were defined and assigned to the various regions. This allows for a clear distinction between the stationary parts (stator-related regions) and the rotating parts (rotor-related regions). By defining a rotational kinematic state for the rotor's mechanical system, Flux 3D can compute the magnetic field at each discrete step, as illustrated in Fig. 2.11, which shows the rotor's 60° displacement relative to the stator.

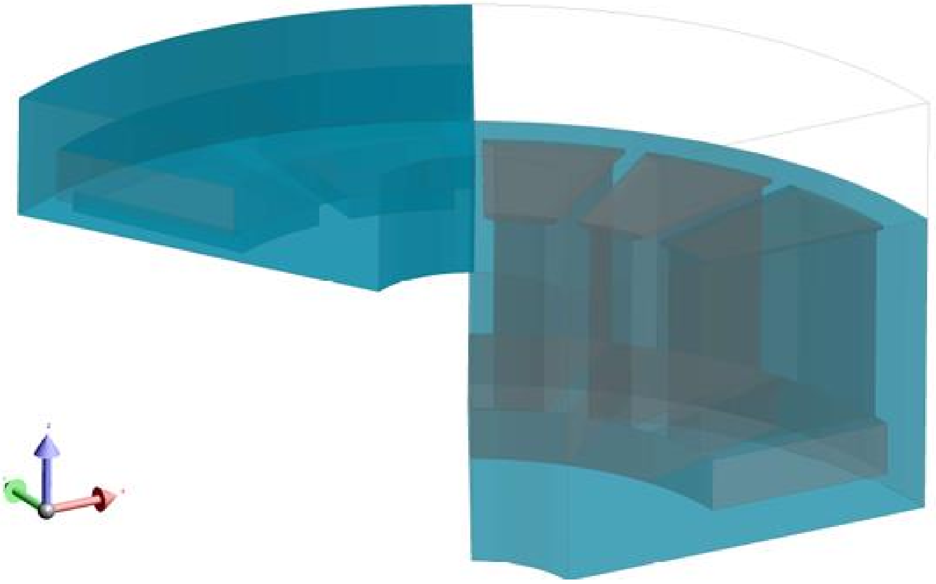

Figure 2.11 - Bgap solved scenario solved

2.3.1 Air-gap Induction Profile

The air-gap flux density distribution is one of the most significant parameters in electrical machine design, as it directly influences torque production, back-EMF waveform, and magnetic losses. In this comparative study, it is important to emphasize that no attempt was made to equalize the fundamental component (B_g) of the air-gap induction between the two machines.

To extract these values, a computation path was defined within the Flux 3D environment. As illustrated in Fig. 2.12, the path consists of a circular arc located exactly at the average diameter (D_{avg}) and positioned at the center of the air-gap ($h_{gap}/2$). The air-gap flux density is calculated along this path for an angular span corresponding to one magnetic pole. This spatial sampling allows for a precise evaluation of how the V-shaped concentration effect in the AF-IPM compares to the standard radial distribution of the AF-SPM.

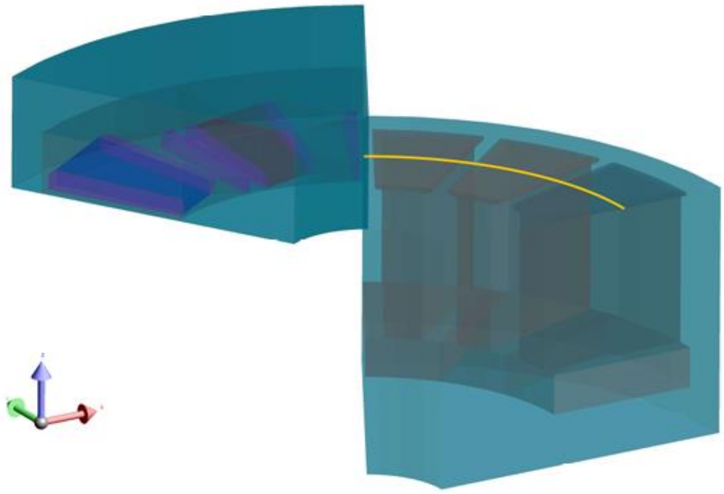

Figure 2.12 - Computation Path

The obtained waveforms, shown in Fig. 2.13, reveal distinct characteristics for each configuration:

AF-SPM Profile: Evaluating the harmonic content rather than localized maxima, spectral analysis reveals that this topology achieves a fundamental air-gap flux density amplitude of 1.101 T. The spatial profile shows an ascending trend towards the edges of the pole before experiencing localized drops in correspondence with the stator slot openings.

AF-IPM Profile: The waveform across the pole arc appears flatter. In terms of effective magnetic loading, the AF-IPM yields a slightly lower fundamental amplitude of 1.076 T, which corresponds to a marginal reduction of approximately 2.2% compared to the surface-mounted design. Although the fundamental component remains highly comparable, the influence of the stator slots is visually more pronounced in this topology.

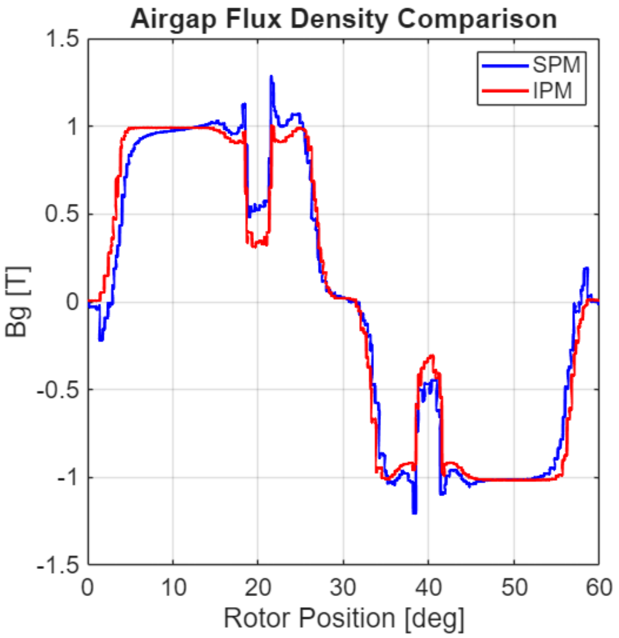

Figure 2.13 - Air-gap flux density comparison

Table 2.2: Fundamental airgap flux density

Parameter	AF-SPM [T]	AF-IPM [T]	Δ (%)
Bg	1.101	1.076	2.2

To further quantify the differences observed in the waveforms, a Fast Fourier Transform (FFT) analysis was performed using the embedded Altair flux tool. The harmonic spectrum (Fig. 2.14) highlights the distribution of the magnetic content for both machines.

Fundamental Component Analysis Despite the visible differences in the peak values and the depth of the slotting dips, the analysis of the fundamental component reveals a substantial equivalence between the two designs. The spectral extraction indicates that the fundamental flux density is 1.101 T for the AF-SPM and 1.076 T for the AF-IPM. The difference is less than 2.5%. This result confirms that the designed AF-IPM rotor can match the fundamental magnetic loading of the AF-SPM benchmark, effectively compensating for the geometric differences and the slightly lower magnet volume.

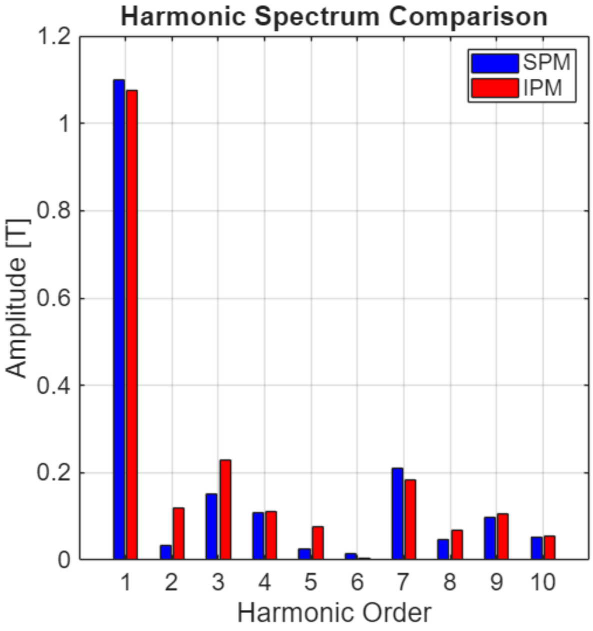

Figure 2.14 - Harmonic spectrum comparison

Table 2.3: Harmonic spectrum details

Harmonic order	AF-SPM [T]	AF-IPM [T]	Δ (%)
1	1.101	1.076	2.2
3	0.150	0.228	51.7
5	0.026	0.076	188.7
7	0.210	0.183	12.6

- 3rd Harmonic: The AF-IPM spectrum shows a dominant 3rd harmonic component of approximately 0.2 T, which is higher than that of the AF-SPM. This high value correlates with the flatter shaped of the induction waveform observed in the time domain.
- 5th Harmonic: The AF-IPM configuration exhibits a marginally higher fifth harmonic component, with a peak value of about 0.1 T.
- 7th Harmonic: Conversely, the analysis shows that the 7th harmonic magnitude is lower in the AF-IPM compared to the AF-SPM.

In summary, the FFT analysis demonstrates that while the two machines share an identical fundamental component, they possess a distinct harmonic signature due to their different rotor structures.

3 Transient Magnetic Analysis and No-Load Tests

In this section, dynamic behavior requires a transition from the *Magneto-Static* application to the *Transient Magnetic* application. This solver allows for the inclusion of motion equations and the coupling with electrical circuits, enabling the simulation of time-dependent phenomena.

The first stage of the dynamic analysis is the No-Load Test. In this scenario, the rotor is assigned a constant rotational speed equal to the rated speed (n_nom = 1500 rpm), while the stator windings are open-circuited (I_phase = 0 A). The simulation solves the Maxwell equations [13] at discrete time steps over an electrical period to extract the following critical parameters:

- Back-Electromotive Force (Back-EMF): The voltage induced in the stator windings by the time-varying magnetic flux of the permanent magnets.
- Permanent Magnet Flux Linkage: The fundamental flux interacting with the coils.
- Offset Angle Determination: The most crucial output of this phase is the identification of the initial rotor position offset. This angle represents the phase relationship between the rotor's magnetic axis (d-axis) and the stator Phase A axis. Accurate offset estimation ensures correct definition of the synchronous reference frame and proper alignment of the rotor d-axis with the magnetic axis of Phase A during load simulations.

3.1 Physical Parameters

To perform transient simulations, the Finite Element model must be coupled with an external electrical circuit implemented in the Flux Circuit Editor. Before defining the circuit topology, however, it is necessary to establish the mathematical framework and the physical parameters.

The model on Flux operates with a three-phase stator winding (abc system); the control logic and the simulation strategy are based on the rotating reference frame (dq system). This approach allows for the decomposition of the stator current into two DC components: I_d (flux-producing component) and I_q (torque-producing component). Since the Flux 3D circuit requires instantaneous current values for the three phases, an Inverse Park and Clarke Transformation is implemented directly within the software parameters using mathematical formulas. This ensures that by simply defining the inputs I_d and I_q, the software automatically generates the correct time-varying sinusoidal currents for the phases, synchronized with the rotor position.

The transformation chain implemented is:

Inverse Park: From rotating dq system to stationary alpha\beta system:

$$\begin{cases} i_\alpha = i_d \cdot cos(\theta_e) - i_q \cdot sin(\theta_e) \\ I_\beta = i_d \cdot sin(\theta_e) + i_q \cdot cos(\theta_e) \end{cases} \tag{3.1}$$

Inverse Clarke: From stationary alpha\beta system to three-phase system:

$$\begin{cases} i_a = i_\alpha \\ i_b = -\frac{1}{2}\, i_\alpha + \frac{\sqrt{3}}{2} i_\beta \\ i_c = -\frac{1}{2}\, i_\alpha - \frac{\sqrt{3}}{2} i_\beta \end{cases} \tag{3.2}$$

The following parameters were defined in the Flux 3D *Physical Parameter* manager to drive the simulation:

- *Nnom*: Set to 1500 rpm (Rated speed).
- *FREQUENCY*: Calculated as $f = \frac{p \cdot n}{120}$, where p is the number of poles.
- *OMEGA*: The angular electrical frequency, $\omega = 2\,\pi f$
- *OFFSET_ANGLE*: This parameter represents the alignment angle between the rotor magnets and the stator Phase A. In the initial No-Load Test, this is set to 0°. It will later be accurately calculated via post-processing (using Matlab) and updated for the load tests to ensure correct FOC alignment.
- *AngPos(ROTOR)*: defines the instantaneous mechanical angular position of the rotor during the transient simulation
- *GAMMA*: This is the instantaneous electrical position of the rotor, used to calculate the trigonometric functions for the transformations. It is defined as:

$$GAMMA = AngPos(ROTOR) \cdot \frac{POLES}{2} + OFFSET\_ANGLE \tag{3.3}$$

- *ID / IQ*: These are the inputs for the currents. For the No-Load Test, both are set to 0 A.
- *IDtot* / *IQtot*: These parameters represent the total Ampere-Turns per coil. They are defined as:

$$ID_{TOT} = N_{turns} \cdot ID\ ;\ IQ_{TOT} = N_{turns} \cdot IQ \tag{3.4}$$

The factor 12 represents the number of turns per coil (N_{turns}). This value is derived from the winding design: with Z_ph=144 series conductors per phase and 18 slots, the machine features a double-layer winding with 12 turns per coil.

A specific modeling strategy was adopted for the windings: the parameter *TURNS* in the circuit component is set to 1. This approach, combined with the definition of

IDtot (which includes factor 12), allows the current source to inject the total Ampere-Turns (N I) directly.

This method simplifies the parametric sweep, as modifying the number of turns in the future would only require updating the multiplier in the parameter list rather than modifying the circuit topology.

$$N_{turns} = \frac{Zph}{2} \cdot \frac{1}{pp \cdot q \cdot c} = \frac{144}{2} \cdot \frac{1}{6 \cdot 1/2 \cdot 2} = 12 \tag{3.5}$$

Where q is defined as:

$$q = \frac{Nc}{2 \cdot pp \cdot m} = \frac{18}{2 \cdot 6 \cdot 3} = \frac{1}{2} \tag{3.6}$$

Phase Current Generation (Inverse Transformations): The stationary frame currents are derived dynamically using the rotor angle GAMMA

$$I_{alpha} = IDtot \cdot cosd(GAMMA) - IQtot \cdot sind(GAMMA) \tag{3.7}$$

$$I_{beta} = IDtot \cdot sind(GAMMA) + IQtot \cdot cosd(GAMMA) \tag{3.8}$$

$$I1 = I_{alpha} \tag{3.9}$$

$$I2 = -\frac{1}{2} I_{alpha} + \frac{\sqrt{3}}{2} I_{beta} \tag{3.10}$$

$$I_3 = I_1 - I_2 \tag{3.11}$$

In the circuit editor, the coil components representing the phases are assigned a resistance value of R_{ph} = 45.1 mΩ.

3.2 Electric circuit on Flux

The electrical supply is defined using the *Circuit Editor* context in Altair Flux. The adopted circuit topology consists of a three-phase star connection. The schematic is constructed using the following components:

Current Sources: The circuit is driven by ideal current generators. The source for Phase A is driven by formula 3.9, and the source for Phase B is driven by I_2 (derived from the Inverse Park/Clarke transformations). The current in Phase C is determined by the circuit balance at the neutral node ($I_A + I_B + I_C = 0$).

Ground Reference: Unlike an isolated neutral system, the star point is connected to a Ground component, setting the potential reference (V=0) for the circuit solution.

Resistors: Three lumped resistance elements are placed in series with the coils to model the phase resistance. These are assigned to the value Rph previously defined.

Coil Conductors: The interface between the circuit and the 3D model is represented by three *Coil Conductor* components (Coil 1, Coil 2, Coil 3). These conceptual components function as the link that transfers the current from the schematic to the physical domain and collects the induced Back-EMF.

The resulting electrical schematic is shown in Fig. 3.1

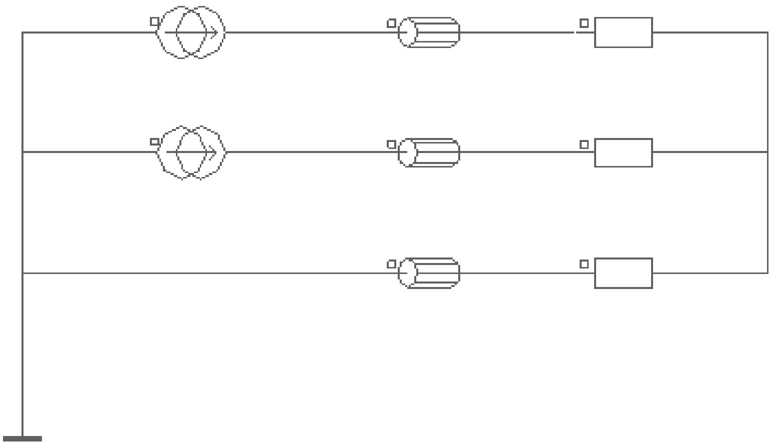

Figure 3.1 - Electric circuit in Flux

Once 3D Winding Geometry and the circuit components are defined, they must be associated with physical geometry. In the Flux 3D environment, the windings are modeled as specific volumes defined as Non_Meshed_Coil magnetic regions.

The coils are generated using the Composed Coil entity available in Flux, as shown in Fig. 3.2.

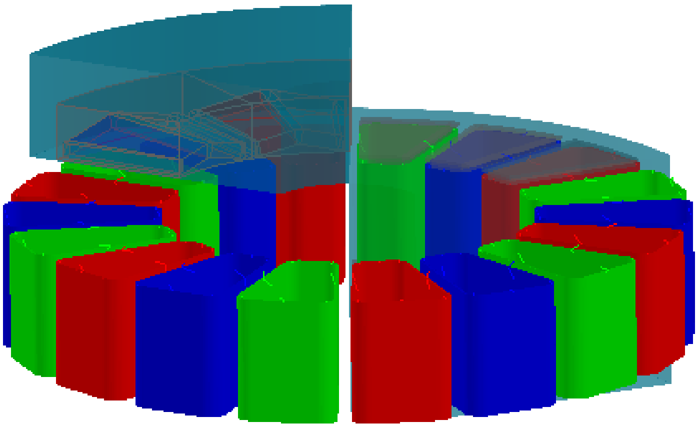

Figure 3.2 - Composed coil

This tool allows for the definition of the coil path through a set of geometric parameters (points and lines) that follow the stator tooth profile as shown in Fig. 3.3, which specifically depicts the geometric construction of Phase A.

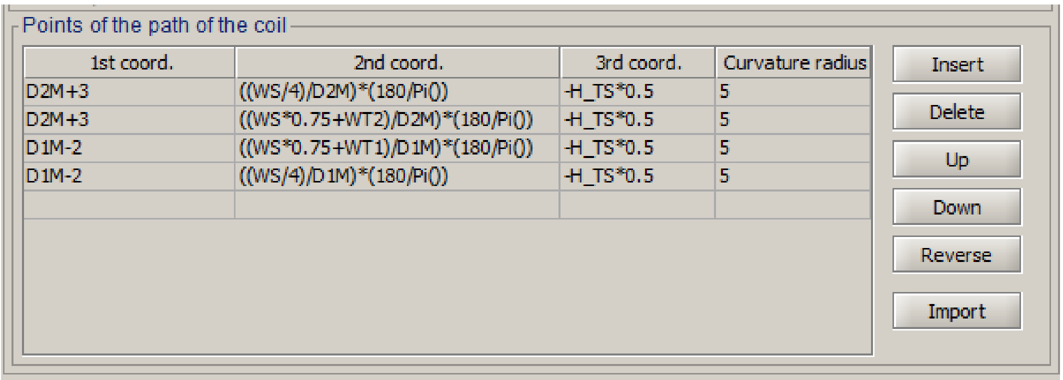

Points of the path of the coil

1st coord.	2nd coord.	3rd coord.	Curvature radius
D2M+3	((WS/4)/D2M)*(180/Pi())	-H_TS*0.5	5
D2M+3	((WS*0.75+WT2)/D2M)*(180/Pi())	-H_TS*0.5	5
D1M-2	((WS*0.75+WT1)/D1M)*(180/Pi())	-H_TS*0.5	5
D1M-2	((WS/4)/D1M)*(180/Pi())	-H_TS*0.5	5

Figure 3.3 - Path of the coil

3.3 No-Load: Back-EMF, Flux Linkage, and Offset Angle

With the complete definition of the geometry, physical parameters, and the coupling with the external electrical circuit, the Finite Element model is ready for the dynamic solution.

The primary objective of the No-Load Analysis is to characterize the electromagnetic performance of the machine in open-circuit conditions ($I_d = I_q = 0$ A). Specifically, this test aims to evaluate the Back-Electromotive Force (Back-EMF) and the Permanent Magnet Flux Linkage, which are fundamental for determining the offset angle. The rotor is assigned a constant rotational speed equal to the rated velocity ($n_{nom} = 1500$ rpm).

To capture the full cyclic behavior of the electromagnetic quantities, the simulation interval must cover at least one complete electrical period. Given the machine's polarity with 6 pole pairs (p=6), one electrical cycle corresponds to a mechanical rotation of 60°.The mechanical angle range is set from −2° to 60°, rather than starting at 0°. This negative offset mitigates the numerical transient inherent to the finite element solver initialization. In dynamic simulations, the initial time steps exhibit numerical noise as the system transitions from a null state to the operating condition. Starting at −2° allows these transients to decay before the rotor enters the post-processing interval (0°–60°).

After completing the transient simulation in Flux 3D, the time-domain results were exported to Matlab for post-processing. This section presents the analysis of the induced voltages (Back-EMF) and flux linkages in the natural three-phase reference frame (abc), leading to the determination of the critical Offset Angle.

The Back-Electromotive Force (Back-EMF) Analysis represents the first dynamic indicator of the machine's performance. Fig. 3.4 illustrates the comparison between the Back-EMF of the AF-SPM and AF-IPM at the speed of 1500 rpm.

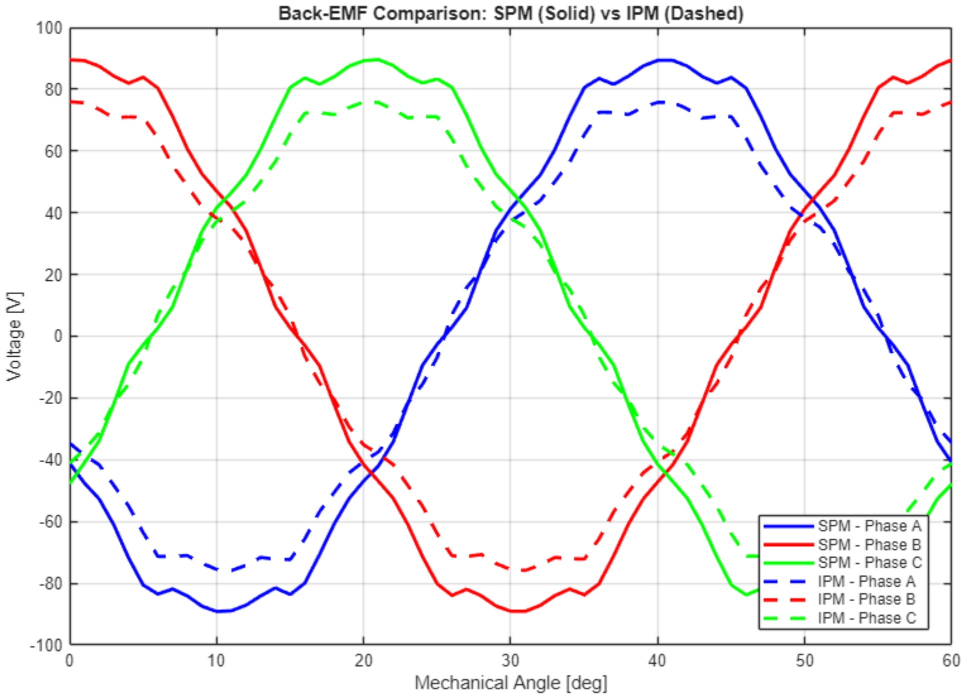

Figure 3.4 - Back-EMF Comparison

Table 3.1: Phase A voltage comparison (no-load)

Parameter	AF-SPM [V]	AF-IPM [V]	Δ (%)
Peak Back EMF	89.35	75.90	15.1
RMS Back EMF	62.94	53.09	15.6

A clear difference is observed in the voltage amplitude, where the AF-SPM exhibits a peak phase voltage of approximately 89 V, whereas the AF-IPM reaches a lower peak of 75 V. This disparity originates from the magnetic circuit architecture: the AF-SPM maximizes flux linkage through surface-mounted magnets directly facing the air-gap, whereas in the AF-IPM the buried magnets introduce iron leakage paths that reduce the effective stator-linked flux. Consequently, the AF-IPM possesses a larger voltage margin, allowing it to reach higher rotational speeds before exceeding the max supply capability. This behavior suggests that the AF-IPM design is naturally better suited for extended speed ranges and flux-weakening operations.

As illustrated in Fig. 3.5 and detailed in Table 3.2, the permanent magnet flux linkage (λ_{pm}) evaluated in the three-phase domain is noticeably lower for the AF-IPM configuration compared to the surface-mounted topology. Specifically, the AF-SPM exhibits a peak flux of 0.0943 Wb and an RMS value of 0.0673 Wb, whereas the AF-IPM achieves lower values of 0.0813 Wb (peak) and 0.0568 Wb (RMS), corresponding to a reduction of 13.8% and 15.7%, respectively. As expected, this reduction is perfectly consistent with the Back-EMF results.

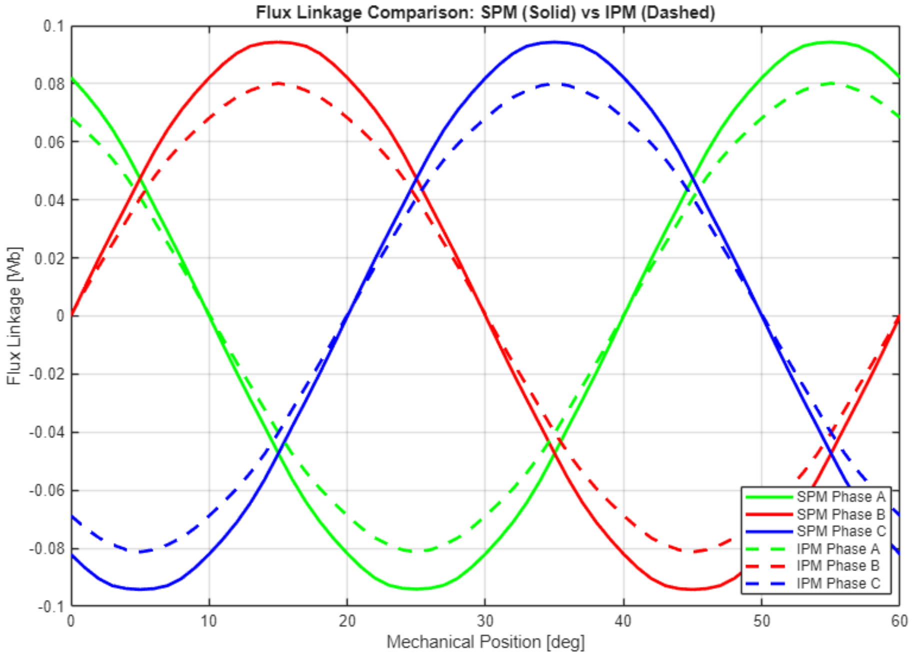

Figure 3.5 - Flux linkage comparison

Table 3.2: Phase A flux linkage (no-load)

Parameter	AF-SPM [Wb]	AF-IPM [Wb]	Δ (%)
Peak flux	0.0943	0.0813	13.8
RMS flux	0.0673	0.0568	15.7

By applying the Fast Fourier Transform (FFT) to the Phase A induced voltage (λ_a), the phase angle of the fundamental component (φ_{bemf}) is extracted:

$$\theta_{offset} = \left(\varphi_{bemf} \cdot \frac{180}{\pi}\right) \tag{3.12}$$

The calculated Offset Angles are:

AF-SPM offset = **30.19°**

AF-IPM offset = **30.01°**

The most rigorous way to evaluate the accuracy of the offset is to perform the coordinate transformation of the flux linkages. In an ideally oriented d-q reference system under no-load conditions, the quadrature flux component (λq) must have a zero-mean value.

3.4 Offset verification

Once the offset angle is determined, the physical three-phase quantities (abc) are transformed into the rotating d-q reference frame. This transformation primarily serves to validate the correctness of the computed offset: under proper alignment, the quadrature-axis flux component (λq) is negligible. Direct Clarke Transformation (*abc* → αβ) The three-phase flux linkages are projected onto the stationary two-phase system using the Amplitude Invariant matrix T_{clarke}:

$$\begin{bmatrix} \lambda_\alpha \\ \lambda_\beta \\ \lambda_0 \end{bmatrix} = \begin{bmatrix} \frac{2}{3} & -\frac{1}{3} & -\frac{1}{3} \\ 0 & \frac{\sqrt{3}}{3} & -\frac{\sqrt{3}}{3} \\ 1 & 1 & 1 \end{bmatrix} \cdot \begin{bmatrix} \lambda_a \\ \lambda_b \\ \lambda_c \end{bmatrix} \tag{3.15}$$

Rotor Angle and Direct Park Transformation (αβ → dq) The electrical angle θ_e is calibrated using the calculated offset and the generator convention shift:

$$\theta_e(t) = (\theta_{mec}(t) \cdot pp) + \theta_{offset} \tag{3.16}$$

The stationary components are then rotated into the synchronous frame using the matrix $T_{park}(\theta_e)$:

$$\begin{bmatrix} \lambda_d \\ \lambda_q \end{bmatrix} = \begin{bmatrix} \cos(\theta_e) & \sin(\theta_e) \\ -\sin(\theta_e) & \cos(\theta_e) \end{bmatrix} \cdot \begin{bmatrix} \lambda_\alpha \\ \lambda_\beta \end{bmatrix} \tag{3.15}$$

Fig. 3.6 (AF-SPM) and Fig. 3.7 (AF-IPM) illustrate the final dq flux components obtained using the selected interpolated offsets. It can be observed that λd correctly settles around the maximum Permanent Magnet flux value, while λq oscillates perfectly around zero, validating the alignment.

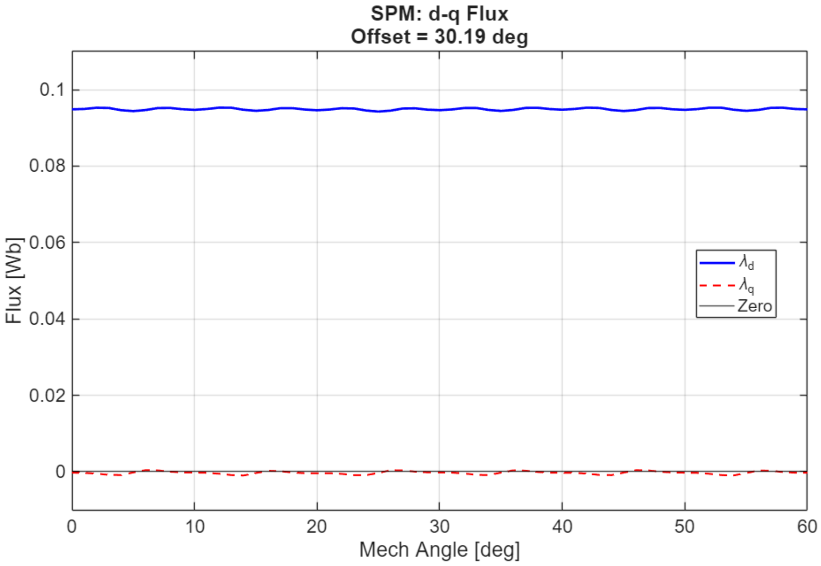

Figure 3.6 – AF-SPM: d-axis alignment verification

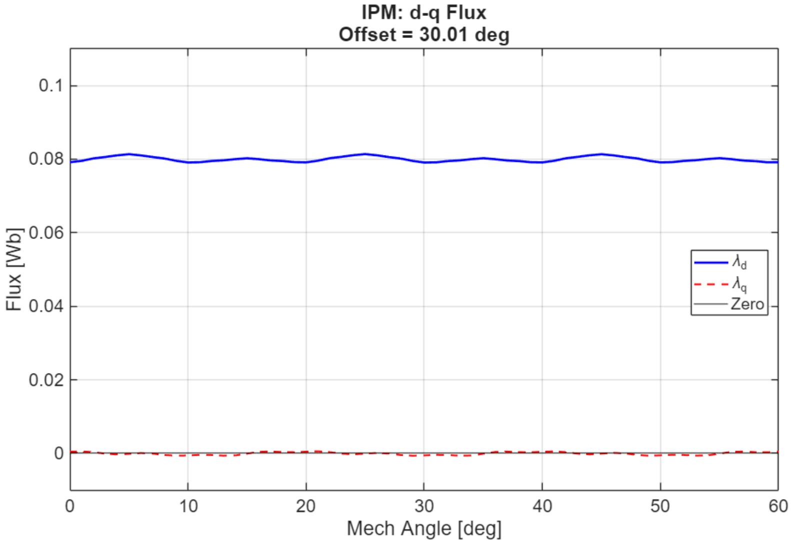

Figure 3.7 – AF-IPM: d-axis alignment verification

Finally, it is important to acknowledge that the offset calibration method adopted in this phase relies on a numerical approach rather than an exact analytical solution. While this method successfully identifies a functional operating point where the mean quadrature flux (λq) is zero, a strictly rigorous determination of the electromagnetic axis would require a detailed analytical calculation of the Magnetomotive Force (MMF) distribution. However, the alignment precision achieved is sufficiently high to ensure an accurate current vector orientation relative to the rotor flux.. A simplified flowchart is presented next to outline the core logic of the MATLAB script used for the offset validation.

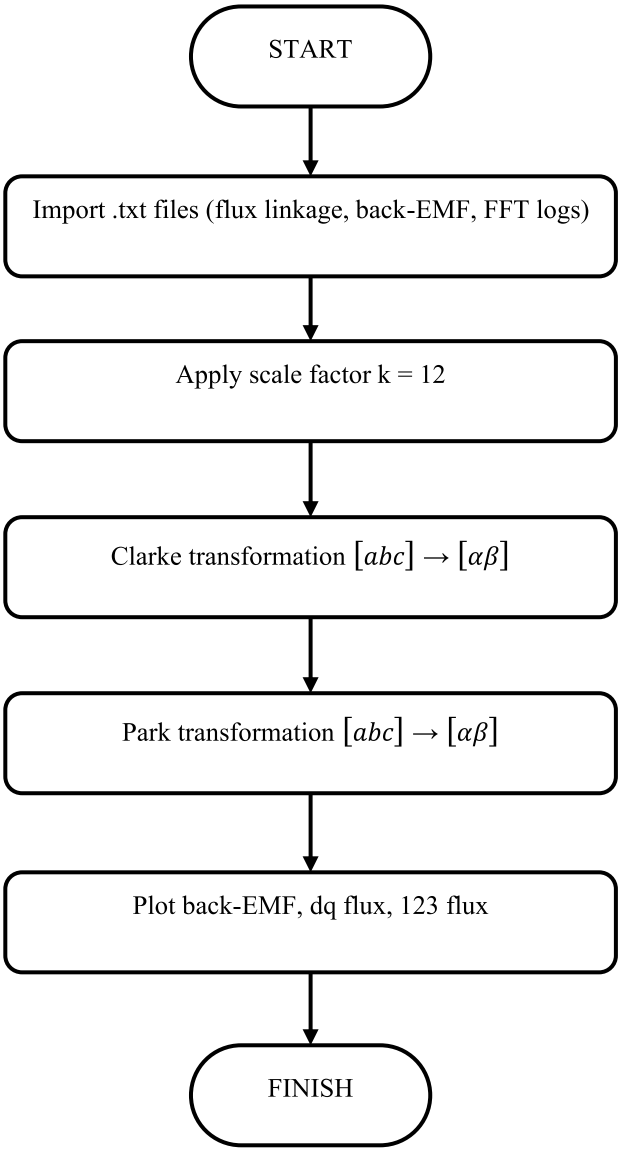

Figure 3.8 - Flowchart of the Offset validation algorithm

Figure 3.8: Flowchart of the post-processing algorithm for a single machine topology. The procedure computes the rotor offset angle using two distinct methods: detection of the Phase A flux linkage peak via Cubic Spline Interpolation and Back-EMF FFT. Comparative verification is then performed by applying the Park transformation with both angles; the method yielding a quadrature flux component (λq) with a mean value closest to zero is selected as the optimal offset angle

4 Operating trajectories and on-load analysis

4.1 Integrated matlab-flux 3D simulation environment

To evaluate the current to flux maps of the considered machines, a dedicated co-simulation environment was developed. This setup combines Altair Flux 3D for finite element analysis with Matlab for scripting and data processing.

Matlab: Manages the co-simulation framework. It defines the input variables, generates the reference test vectors (I_d, I_q,rotor position), and controls the overall simulation workflow. The main logic is centralized in a single script (*master.m*) valid for both AF-SPM and AF-IPM machines.

Flux 3D (FEM Solver): Serves as the computational core of the framework. Operating in server mode, it receives the input parameters, updates the physical model, solves the load scenario in Flux 3D, and returns the computed results to the Matlab environment.

The interaction between the two environments is modularized through dedicated solver functions (Appendix: *solver_SPM.m* and *solver_IPM.m*). Based on the selected machine topology, the script *master.m* calls the appropriate function. The total duration of the process, as well as the resolution of the resulting Look-Up Tables, is directly governed by the discretization of the current domain. A finer current grid (I_{STEP}) improves the accuracy in capturing magnetic saturation effects but leads to a proportional increase in the computational time required for the FEA solution.

To provide a clear overview of the iterative scanning process in the script, the algorithm is schematically depicted in the flowchart of Fig. 4.1:

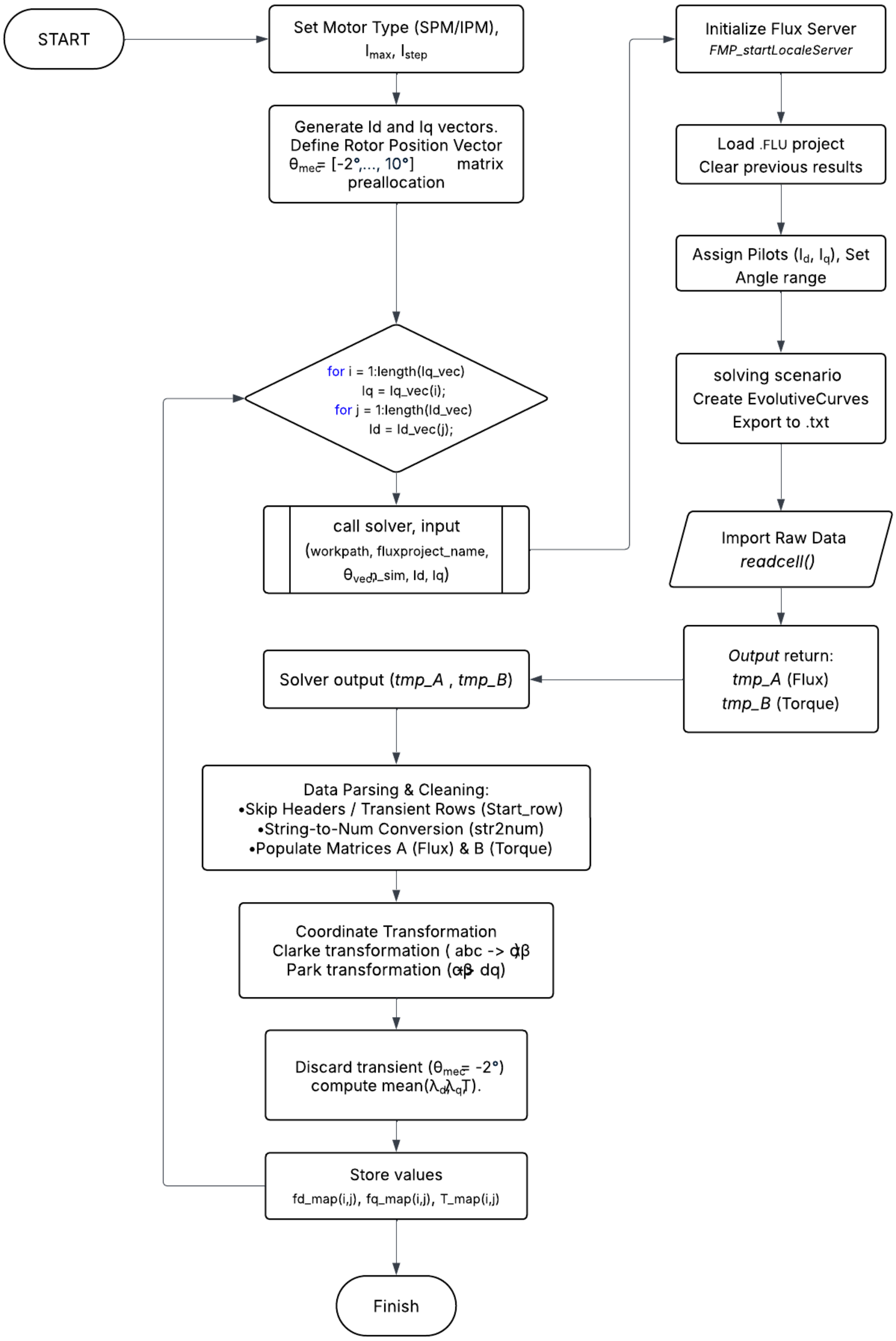

Figure 4.1 – Algorithm Flowchart (master.m; SPM_solver.m; IPM_solver.m)

4.2 Definition of the simulation domain

To ensure the Finite Element Analysis correctly represents the physical limits of the machine, the input vectors for the co-simulation specifically the current magnitude and the rotor position range must be defined starting from the initial sizing data.

The maximum current value for the simulation grid is derived from the thermal limit imposed during the preliminary sizing phase. The design assumes a nominal current density $J_{rms} = 7.43\ A/mm^2$ and a total available copper area per slot $A_{Cu} = 72.5\ mm^2$. Since the Flux 3D model is set up with single-turn coils (imposed number of TURNS = 1), the solver input requires the Ampere-turns (A t):

$$A \cdot t_{peak} = J_{rms} \cdot S_{Cu} \cdot \sqrt{2} = 7.43 \cdot 72.5 \cdot \sqrt{2} = 761.8\ \ A \cdot t \tag{4.1}$$

However, the logic in Matlab and the current to flux maps must operate in terms of phase current (Amperes), the maximum phase current limit (I_{max}) adopted for the simulation grid is:

$$I_{max} = \frac{A \cdot t_{peak}}{N_{turns}} = \frac{761.8}{12} = 63.48\ A \tag{4.2}$$

Based on this limit, the I_d and I_q current vectors are discretized over the range [-63, +63] A. To balance computational time with map resolution, a step size of $I_{max}/4$ is chosen ($I_{step} \approx$ 15.75 A), resulting in a 9x9 matrix of operating points.

Regarding the simulation range, the rotor position (ϑ_{mec}) is varied to capture the electromagnetic torque ripple and average flux values, the simulation must cover a representative portion of the electrical period. Given that the torque profile repeats six times within one electrical period of 60° mechanical, a rotation range of 10° was selected. This span is sufficient to fully characterize one complete fundamental cycle of the torque ripple and the repeating variations of the magnetic quantities.

To mitigate the numerical initialization errors inherent to the transient solver in Flux 3D (which produce unstable results in the first time-step), the simulation interval is extended backwards:

$$\vartheta_{sim} = [\,-2°, 0°, 2°, .\,.\,., 10°\,] \tag{4.3}$$

With a step size of 2°, this results in 7 simulation points per current couple. In the post-processing phase, the first point ($-2°$) is discarded as a transient error, and the values from $0°$ to $10°$ are averaged to obtain the DC parameters for the current to flux maps.

The core of the identification algorithm is structured around a nested loop iteration that scans the entire discretized current plane. As defined in the configuration parameters, the outer loop iterates through the quadrature current (I_q), while the inner loop scans the direct current (I_d). For every operating point ($I_{d,k}$, $I_{q,k}$), the Master script calls the corresponding solver function (Appendix: *SPM_ solver.m* or *IPM_ solver.m*).

A critical aspect of this implementation is the management of the Finite Element Method (FEM) server. To minimize memory leakage and ensure a "clean state" for every simulation point, the Flux 3D server is instantiated and terminated at each iteration. The communication is established via the Java-based Flux-machine-Link API, initialized directly from Matlab. Once the server is active, Matlab acts as a remote commander, sending instructions that are executed within the Flux environment as Jython (Java-Python) scripts. The *FMP_executeJythonCommand* function is used to bridge the two environments, allowing Matlab to drive the FEM software as if the user were typing commands manually in the Flux console. Inside the solver function, the simulation environment is prepared dynamically.

4.3 Execution of the parametric sweep

The script first loads parametric physics and clears any results or scenarios from previous runs to prevent data corruption. Subsequently, a new simulation scenario is generated for the specific current couple and rotor position vector defined in the Master script. The currents I_d and I_q are injected into the model by assigning them to the pilot parameters of the physical circuit:

```
FMP_executeJythonCommand(serverUid,strcat('Scenario["RES_FLUXPROJECT"].addPilot(..
pilot=MonoValue(parameter=VariationParameter["ID"], value=',num2str(Id),'))'))

FMP_executeJythonCommand(serverUid,strcat('Scenario["RES_FLUXPROJECT"].addPilot(..
pilot=MonoValue(parameter=VariationParameter["IQ"], value=',num2str(Iq),'))'))
```

Listing 4.1 *- (from "SPM_solver.m") Initialization of the local Flux Server*

Following the parameter assignment, the magnetostatic solution is launched. The solver computes the magnetic field distribution for each step of the rotor position vector ($\vartheta_{mec} = [\,-2°,.\ .\ .\,, 10°\,]$). Upon completion, the connection is closed to release system resources. After the transient magnetic solution is completed, the relevant field data are stored within the Flux project. To extract usable results, the solver via Jython commands to generate evolutive curves that describe the variation of selected physical quantities as a function of the rotor mechanical position (ϑ_{mec}). Specifically, two distinct curve objects are created, Flux linkage curves and Electromagnetic torque curve. The Matlab command dynamically constructs the Jython string to define these curves and export them to .txt files in the working directory. Then the solver performs a read operation to bring the data back into the Matlab environment. Using the readcell() function.

```
tmp_A = readcell(fullfile(WORKPATH, 'SPM_MTPV.txt'));    % Raw Flux Data
tmp_B = readcell(fullfile(WORKPATH, 'SPM_MTPV_1.txt')); % Raw Torque Data
```

Listing 4.2 *- (from "SPM_solver.m") raw data*

Consequently, the solver function terminates by returning two raw cell arrays, tmp_A and tmp_B, directly to the Master script. This approach ensures that the Master code handles MATLAB variables rather than file paths.

Once the Master script receives the *tmp_A* and *tmp_B* arrays, it proceeds to clean and parse the data. Since the raw export from Flux includes headers and string-formatted numbers, the script iterates through the cell array starting from the valid data row (skipping the initial lines), converts the text strings into numerical values (*str2num*), and extracts the relevant columns. The clean phase flux linkages $\lambda_{abc}(\theta)$ are then processed through the coordinate transformation chain:

Clarke Transformation: $abc \rightarrow \alpha\beta$.

Park Transformation: $\alpha\beta \rightarrow dq$, utilizing the specific rotor offset angle (θ_{offset}) to align the reference system.

Finally, to populate the static Look-Up Tables, the instantaneous *d-q* flux and torque waveforms are averaged over the simulated electrical period (excluding the initial transient step at $\theta = -2°$. The resulting mean values are stored in the *fd_map*, *fq_map*, and *T_map* matrices. This cycle repeats until the entire current grid is scanned, and the final 3D maps are saved in a .mat binary file for subsequent analysis.

4.4 Post-Processing and Performance Mapping

The script *master.m* outputs flux linkages (λ_d, λ_q) and electromagnetic torque (T_{fem}) over the discretized current domain. A dedicated Matlab post-processing algorithm converts these static maps into performance metrics such as torque–speed envelopes, and optimal current trajectories. This section details the analytical procedures implemented to process the results, validate the magnetic model, and derive the maximum performance capabilities of both the Surface Permanent Magnet (AF-SPM) and Interior Permanent Magnet (AF-IPM) configurations.

4.4.1 Initialization, parameter scaling and interpolation of input

The post-processing script (*post_processing.m*) is designed as a comparative tool, iteratively analyzing the *.mat* datasets generated by the script *master.m*. The first step involves the normalization of physical quantities to ensure consistency between the FEA domain and the domain. The traction drive is powered by a DC link voltage $V_{dc} = 400\,V$ and the maximum available phase voltage amplitude (V_{phmax}) is derived as:

$$V_{phmax} = \frac{V_{dc}}{\sqrt{3}} \cdot \frac{1}{\sqrt{2}} = \frac{V_{dc}}{\sqrt{6}} = 163.3\,V_{pk} \tag{4.4}$$

This value defines the voltage limit used later for the flux-weakening analysis.

Flux Linkage Rescaling (K_{scale}): A specific alignment is required between the torque computed directly by Flux 3D and the flux linkages extracted from the coils. In Flux 3D the coils were defined with a unitary number of turns per elementary region, while the current injection was scaled by the equivalent turns ratio ($N_{turns} = 12$, as derived in equation 3.5). Consequently, the raw flux linkage values exported by the solver (λ_{raw}) correspond to the single-turn definition. To obtain the actual phase flux linkage (λ_{ph}) consistent with the torque production, a scaling factor must be applied:

$$\lambda_{d,q} = \lambda_{d,q}^{raw} \cdot N_{eq} = \lambda_{d,q}^{raw} \cdot 12 \tag{4.5}$$

The script then reconstructs the current axes vectors (I_d, I_q) based on the simulation limits determined in the previous section ($I_{max} = 63.48\,A$). This defines the discrete support grid for the subsequent interpolation.

The Finite Element Analysis yields the magnetic characteristics of the machine on a relatively sparse grid (9 x 9 points) to maintain reasonable simulation times. While this resolution captures the macroscopic saturation trends, it is insufficient for the precise numerical determination of current trajectories on the plane d-q. Algorithms for Maximum Torque Per Ampere (MTPA) and Flux-Weakening rely on finding the exact tangency points between current circles and voltage ellipses. Using the raw discrete data would result in "step-like" gradients and inaccurate peak detection. To overcome this limitation, the post-processing algorithm reconstructs the continuous magnetic surfaces through an interpolation process.

First, a dense grid is defined using the meshgrid command. The current plane is re-sampled with a significantly finer step size ($\Delta \mathrm{I}_{calc} = 0.1\,A$) compared to the original FEA step ($\approx 15\,A$). The interpolated grid is extended to cover the entire current plane ($I_d \in [-I_{max}, +I_{max}], I_q \in [-I_{max}, +I_{max}]$). This mapping ensures that the analysis is not restricted to a single quadrant, allowing for the evaluation of the machine's behavior in all current quadrants.

The mapping of the original sparse data (T_{map}, $\lambda_{d,q}^{map}$) onto the new dense grid (T_{grid}, $\lambda_{d,q}^{grid}$) is performed using the interp2 function. This function performs 2D interpolation: it takes the discrete FEA results (such as flux linkages and torque) and calculates their values on the new high-resolution grid.

Among the available methods, Cubic Spline interpolation ('spline') was selected. The result of this stage is a set of matrices (*Lambda_d_grid, Lambda_q_grid, T_grid*) containing a large number of operating points.

4.4.2 Ideal MTPA trajectory and current limit

The determination of the Maximum Torque Per Ampere (MTPA) trajectory is performed numerically by scanning the d-q plane. Since the MTPA strategy aims to maximize the torque for a given current magnitude, the algorithm operates in polar coordinates, iterating through concentric current circles.

The MATLAB script implements this search through the following steps:

1. Magnitude Discretization: A loop iterates the current vector magnitude $|I_s|$ from 0 up to the maximum supply current limit (I_{max}).

2. Angular Sweep: For each fixed current magnitude, the current phase angle θ is varied. The search is strictly limited to the second quadrant (from π/2 to π). This range corresponds to the motor operation mode with negative d-axis current (i_d < 0), which is necessary to exploit the reluctance torque component in the AF-IPM configuration.

3. Coordinate Transformation: The polar coordinates ($|I_s|$, θ) are converted into Cartesian coordinates (i_d, i_q) to query the interpolated torque map.

4. Peak Detection: For each current circle, the algorithm extracts the torque profile and identifies the index of the maximum value. The corresponding (i_d, i_q) pair is stored as an optimal operating point.

By collecting these optimal points for increasing current levels, the continuous MTPA locus is reconstructed. For the AF-SPM machine, this locus naturally aligns with the q-axis, whereas for the AF-IPM machine, it follows a hyperbolic trajectory into the second quadrant.

The specific logical flow adopted for the MTPA calculation is detailed in the following flowchart (Fig. 4.2). This diagram summarizes the core algorithm implemented in the post_processing.m script, the full script is reported in the Appendix.

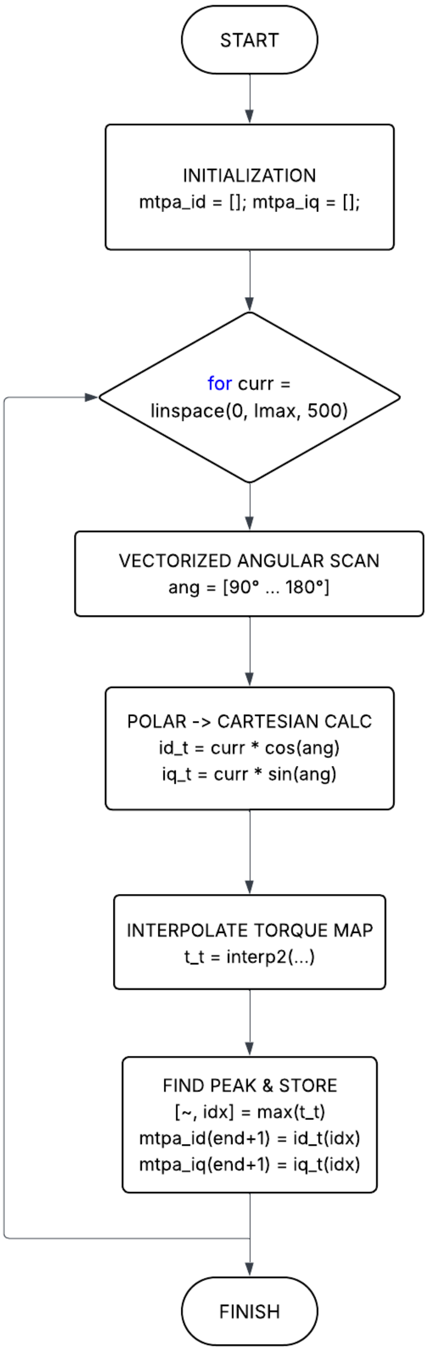

Figure 4.2 – Flowchart of the numerical algorithm used to identify the MTPA trajectory by scanning current circles in the second quadrant.

4.4.3 Speed Loop and Flux-Weakening Strategy

Once the MTPA locus is identified, the analysis extends to the entire speed range to evaluate the machine's behavior under voltage constraints. This phase is handled by a *while* loop that iteratively increases the rotational speed (n) until a maximum threshold is reached or the machine can no longer produce torque.

As the rotor speed (ω_{el}) increases, the Back Electromotive Force (Back-EMF) induced in the stator windings rises proportionally. The system must supply a terminal voltage sufficient to overcome both the resistive voltage drop and the Back-EMF. The magnitude of the required voltage vector is calculated at each grid point using the steady-state equations:

$$\begin{cases} V_d = R_s\, i_d - \omega_{el} \cdot \lambda_q(\, i_d\, i_q) \\ V_q = R_s\, i_q + \omega_{el} \cdot \lambda_d(\, i_d\, i_q) \end{cases} \tag{4.6}$$

$$V_{peak} = \sqrt{{V_d}^2 + {V_q}^2} \leq V_{phmax} \tag{4.7}$$

When V_{peak} approaches the DC bus limit (V_{max}), the inverter saturates. The current vector must be adjusted to reduce the flux linkage (Flux-Weakening), typically by increasing the negative d-axis current component.

The Matlab script (*post_processing.m*) implements a Boolean masking approach, which acts as a filter on the interpolated maps:

- Current Mask: Identifies all points within the thermal limit circle (${i_d}^2 + {i_q}^2 \leq I_{max}$).
- Voltage Mask: Identifies all points where the required voltage is lower than the supply limit ($V_{peak} \leq V_{lim}$).
- Valid Mask: The intersection of these two masks defines the valid operating area for the specific speed step.

where the supply voltage limit is defined as:

$$V_{lim} = \frac{400}{\sqrt{6}} \tag{4.8}$$

Within the valid operating area, the algorithm searches for the maximum torque value (max_Te) .At low speeds, the voltage constraint fully covers the current limit circle, and the maximum torque coincides with the MTPA operating point. As the speed increases, the voltage ellipse gradually contracts, causing the maximum torque point to move along the current boundary toward the negative d-axis, entering the flux-weakening region.

Once the optimal operating point (i_d, i_q) is identified for the current speed step, the script extracts the corresponding flux values (λ_d, λ_q) from the maps. To ensure the consistency of the numerical model, a validation step is performed by calculating the electromagnetic torque analytically:

$$\mathrm{T}_{em} = \frac{3}{2}\, p\, \left(\lambda_d\, i_q - \lambda_q i_d \right) \tag{4.9}$$

This value is stored alongside the FEM-lookup torque (t_fem). If the simulation is consistent, these two values must be identical. Finally, the mechanical power is computed as $\mathrm{P}_{mec} = \mathrm{T}_{em} \cdot \omega_{mec}$. The loop continues incrementing the speed until the valid operating area (torque drops to zero).

This process generates the complete datasets (Speed, Torque, Power, I_d, I_q trajectories) required for the comparative performance analysis.

To provide a clear visual representation of the iterative strategy, the following flowchart (Fig. 4.3) summarizes the logical steps executed by the script.

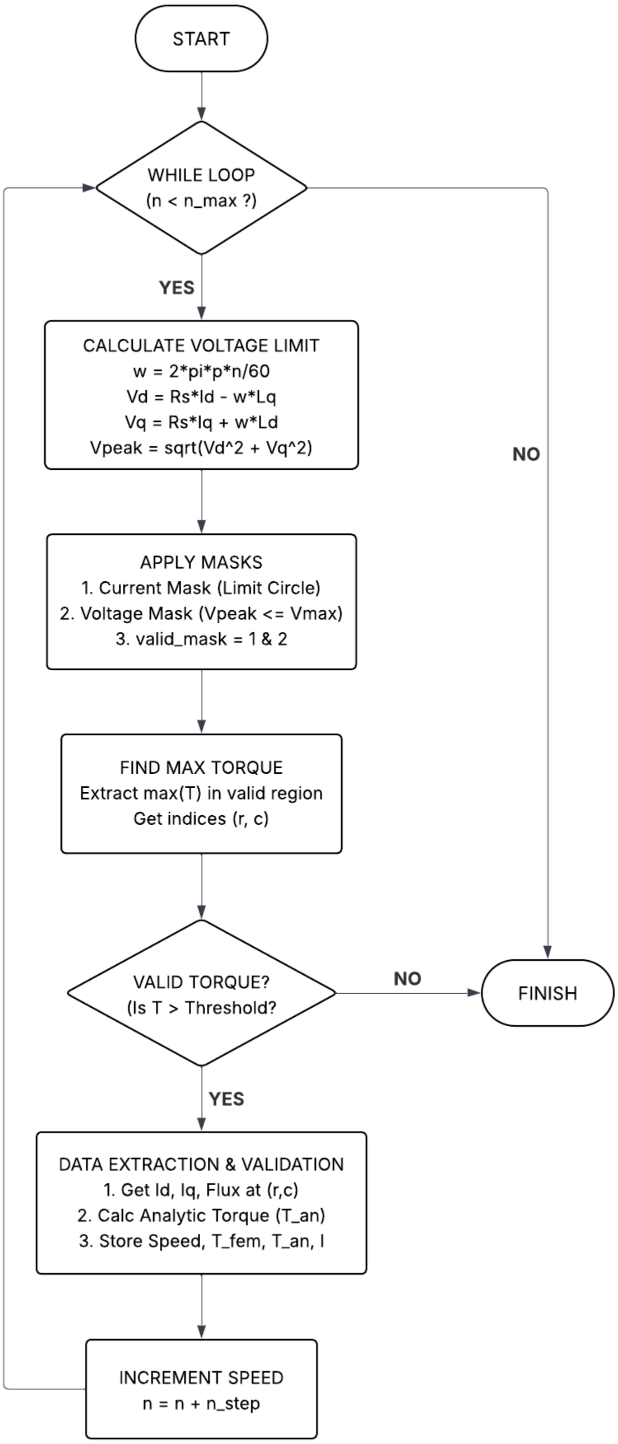

Figure 4.3 – Flowchart of the speed loop Algorithm

5 Performance comparison

The following analysis presents the comparative simulation results obtained for the two machines under investigation, the AF-SPM and the AF-IPM. The performance metrics and operating envelopes reported in this chapter are the result of a numerical elaboration performed via a dedicated MATLAB script (Appendix: `post_processing.m`). This algorithm processes the raw flux to current and torque maps, previously extracted from the Finite Element Analysis (FEA) over the entire current domain (i_d, i_q), to reconstruct the machine behavior and identify the optimal trajectory. The investigation begins with the magnetic characterization, where the flux maps are analyzed to quantify the non-linear saturation and cross-coupling effects that influence the machine parameters. These maps serve as the foundation for identifying the optimal current trajectories in the *d*-*q* plane, specifically the Maximum Torque Per Ampere (MTPA) and Flux-Weakening loci. Consequently, the initial performance evaluation focuses on the rated current scenario, comparing the torque-speed envelopes, power delivery, and torque ripple. These results confirm the limitations predicted by the theory, showing a characteristic power drop-off at high speeds. To overcome these constraints and fully explore the potential of the proposed designs, the final part of the chapter introduces a Peak Performance investigation.

5.1 Flux Mapping and Saturation Effects

The Finite Element Analysis (FEA) allows for the accurate extraction of the magnetic flux linkages λ_d and λ_q as functions of the current vector components (i_d , i_q). Unlike ideal linear models, the resulting maps exhibit significant saturation and cross-coupling effects. To better appreciate the differences between the two topologies, the analysis is conducted separately for the direct axis (magnetizing axis) and the quadrature axis.

5.1.1 Direct Axis Flux (λ_d) Analysis

The direct axis flux represents the combined contribution of the permanent magnets and the armature reaction along the rotor's magnetic axis.

In the Surface-Mounted AF-PM configuration, the trend is primarily dominated by the constant magnet flux. As illustrated in Fig. 5.1, for a fixed i_d, the flux λ_d is maximum when $i_q = 0$. As the quadrature current increases toward the rated value (63 A), it saturates the stator teeth. The iron, once filled by the q-axis flux, becomes less permeable to the magnet flux, causing a slight reduction in λ_d.

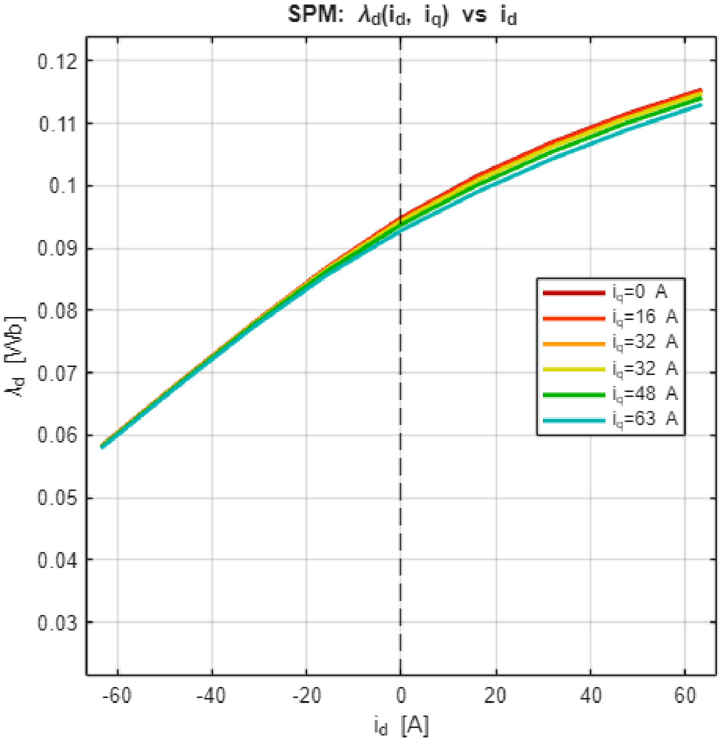

Figure 5.1 - λ_d flux maps for the AF-SPM machine

The Interior Permanent Magnet machine exhibits a more complex behavior due to the rotor geometry. As shown in Fig. 5.2, while the main cross-saturation trend persists (high i_q reduces λ_d), specific non-linearities appear at low currents. These low-current nonlinearities are probably linked to the thin iron bridges (ribs), which, due to their reduced cross-section, tend to saturate early and locally distort the magnetic flux distribution.

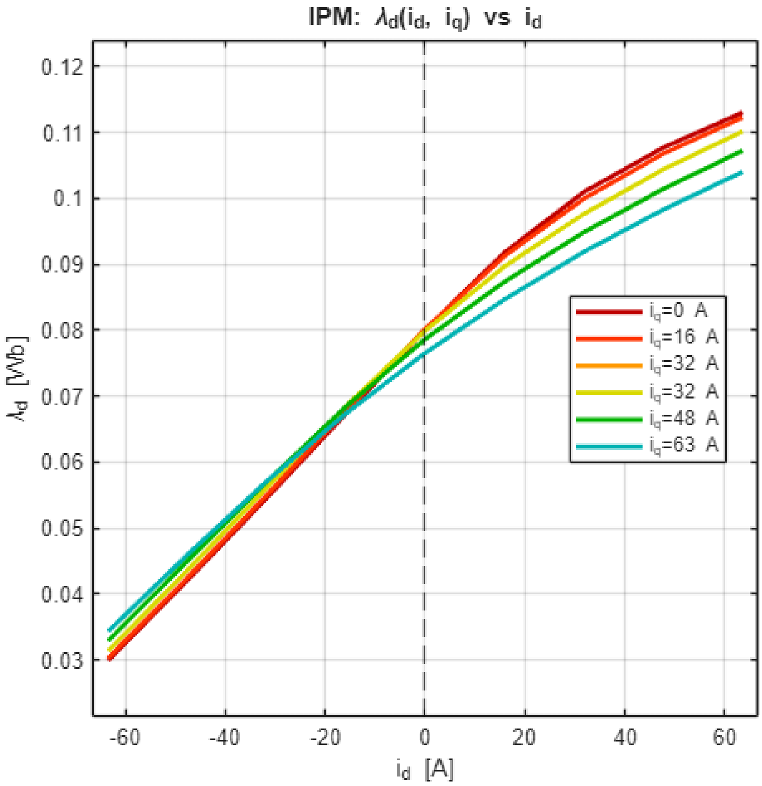

Figure 5.2 - λ_d flux maps for the AF-IPM machine

The 3D flux maps comparison of the magnetic surfaces is provided in Figure 5.3 and

Figure 5.4. The AF-SPM surface exhibits a quasi-planar topology: while it is significantly more regular than the AF-IPM counterpart, it is not a perfectly rigid plane. A visible inclination along the transverse axis confirms the presence of stator saturation and cross-coupling effects, which modulate the flux capability under load. Conversely, the AF-IPM surface presents a distinctly different topography: it originates from a lower absolute flux value at the no-load point compared to the AF-SPM and exhibits a sharper, non-linear curvature.

This visible "warping" of the surface deviates from linear behavior, confirming that the d-axis inductance in the AF-IPM machine is heavily modulated by the operating point, influenced by the variable saturation levels of the rotor iron bridges and the leakage flux paths.

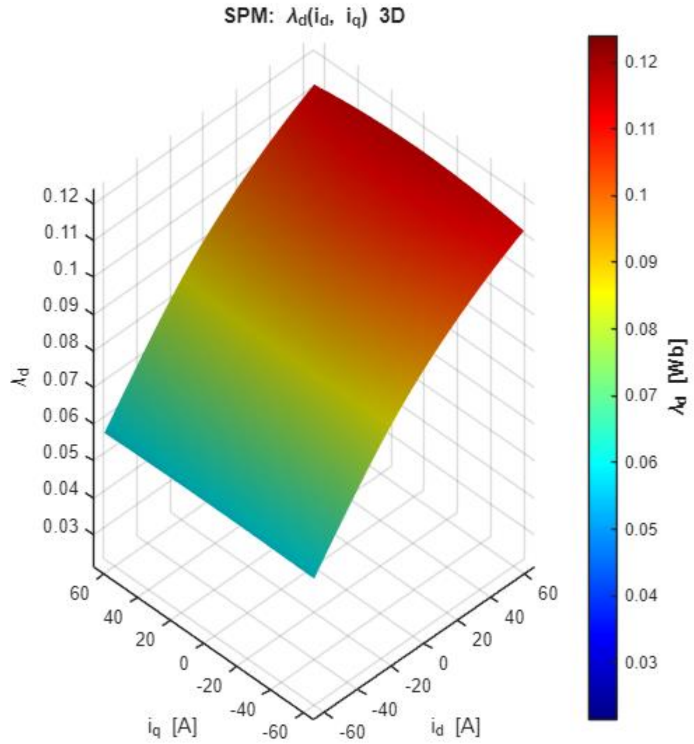

Figure 5.3 - 3D Comparison of λ_d flux surfaces for AF-SPM.

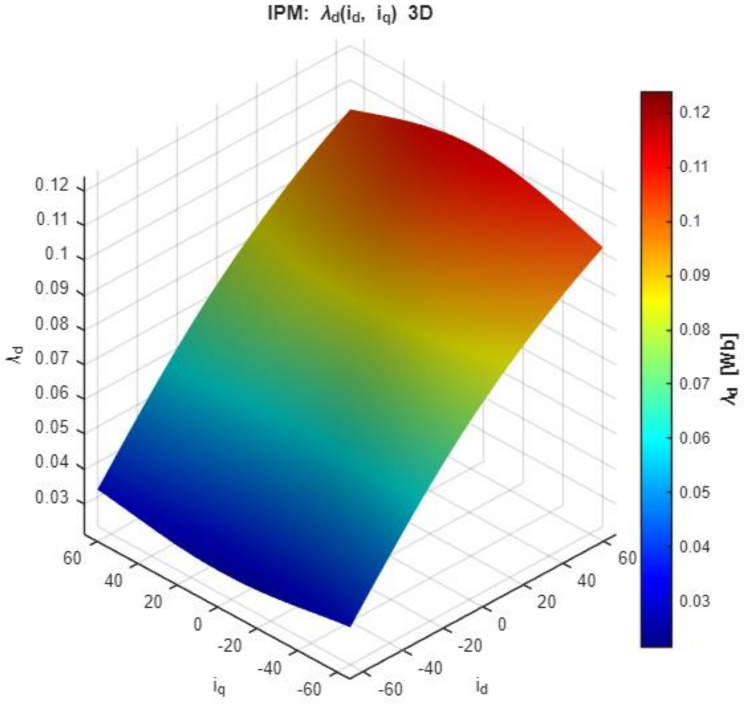

Figure 5.4 – 3D Comparison of λ_d flux surfaces for AF-IPM.

5.1.2 Quadrature Axis Flux (λ_q) Analysis

The quadrature axis flux is directly associated with the torque-producing current component and relates to the q-axis inductance (L_q). Since the rotor has no magnetic source aligned with this axis, one might expect a linear relationship where λ_q is zero when i_q =0. However, the FEA results reveal significant deviations from linearity due to saturation.

In the Surface-Mounted AF-SPM configuration, the behavior is quasi-linear but exhibits a notable inverse saturation effect. As shown in Fig. 5.5, the characteristic curves cross each other at high currents. Specifically, the slope of the curve is steeper when a demagnetizing current (negative i_d) is injected compared to the $i_d = 0$ case. Physically, when the machine operates with high i_q and zero i_d , the stator iron is deeply saturated by the armature field. By injecting a negative i_d component, the field opposes the magnet flux, effectively reducing the net flux density magnitude in the stator yoke. This "unloading" effect brings the ferromagnetic material back to a region of higher permeability. Consequently, the q-axis flux encounters less reluctance and reaches higher values for the same current input.

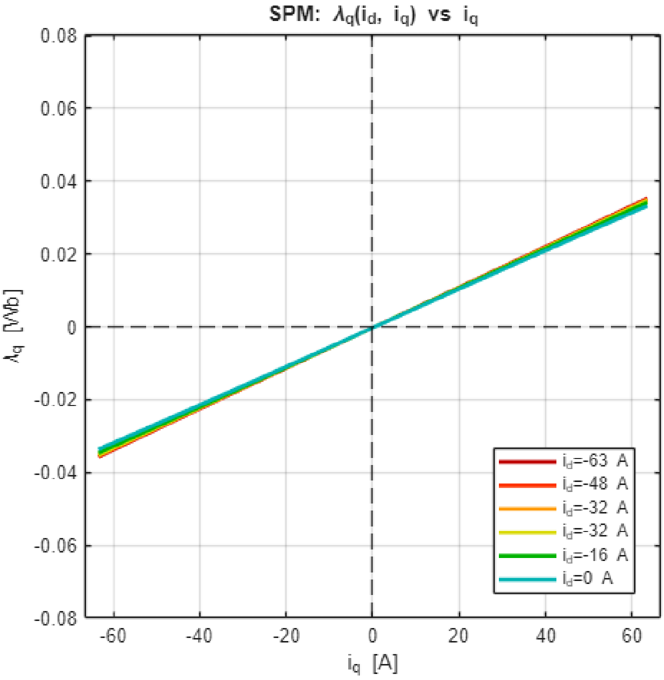

Figure 5.5 – λ_q flux maps for the AF-SPM machine

The Interior Permanent Magnet machine exhibits strongly non-linear behavior, characterized by an "S-shaped" profile and multiple curve crossings, as illustrated in Fig. 5.6. This complex trend is dictated by the sequential saturation of different magnetic paths. At low currents, the iron guides the flux efficiently (linear zone). As i_q increases, the thin rotor bridges (ribs) saturate completely, effectively acting as air-gaps and causing a sharp "knee" in the magnetization curve. Finally, at high current, the stator teeth also saturate. The interaction is intricate because the d-axis current directly modulates the saturation level of these bridges. Depending on whether i_d aids or opposes the saturation of the ribs, the resulting L_q varies, confirming the necessity of precise FEM mapping.

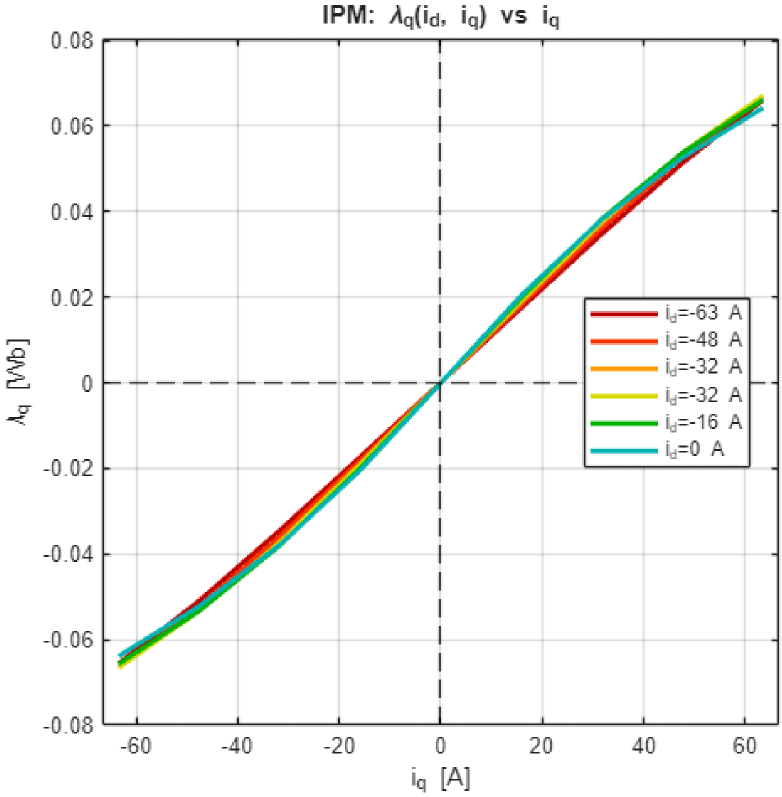

Figure 5.6 – λ_q flux maps for the AF-IPM machine

3D flux map comparison of the magnetic surfaces is provided in Fig. 5.7 and Fig. 5.8. The AF-SPM surface displays a characteristic "twisting" effect: while relatively smooth, the surface gradient changes with the application of negative i_d, visually confirming the beneficial demagnetization effect described above. The AF-IPM surface, conversely, is dominated by a high initial gradient at the origin, reflecting the high q-axis inductance ($L_q > L_d$) due to the rotor saliency. This surface flattens out rapidly as current increases, exhibiting a steep non-linear curvature that corresponds to the saturation of the rotor iron bridges. The comparison reveals that the AF-IPM topology achieves higher flux capability under current excitation compared to the AF-SPM. This highlights that while the AF-SPM offers a more stable inductance profile, the AF-IPM exploits this superior flux capability and high-saliency region to generate a substantial reluctance torque component.

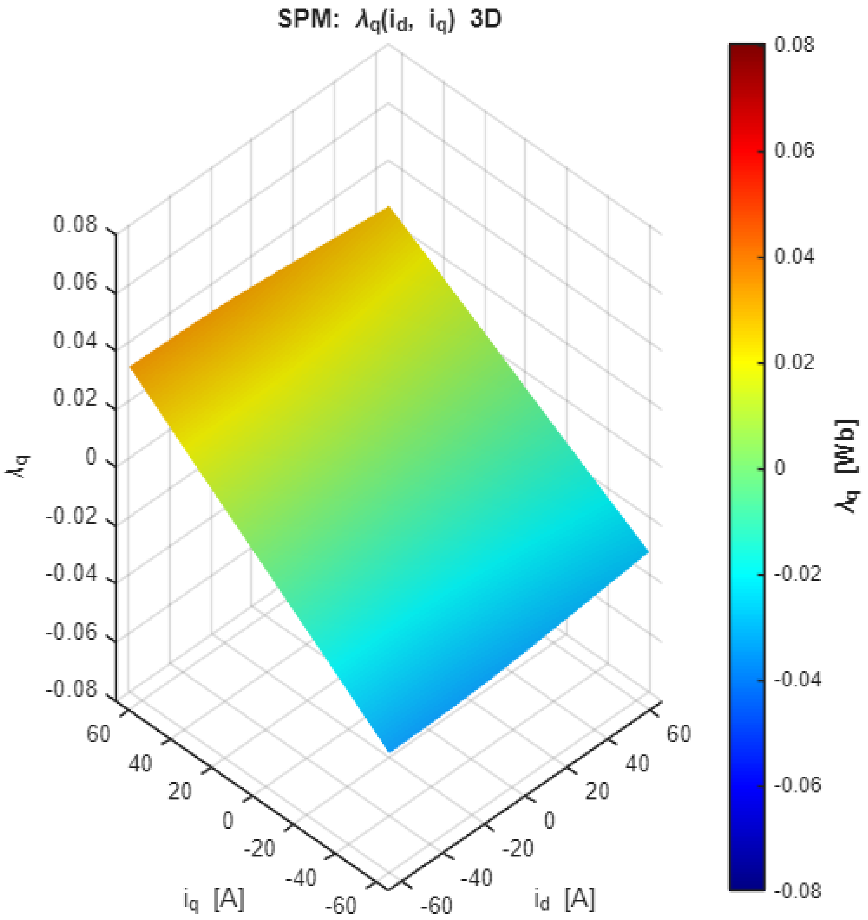

Figure 5.7– 3D Comparison of λ_q flux surfaces for AF-SPM.

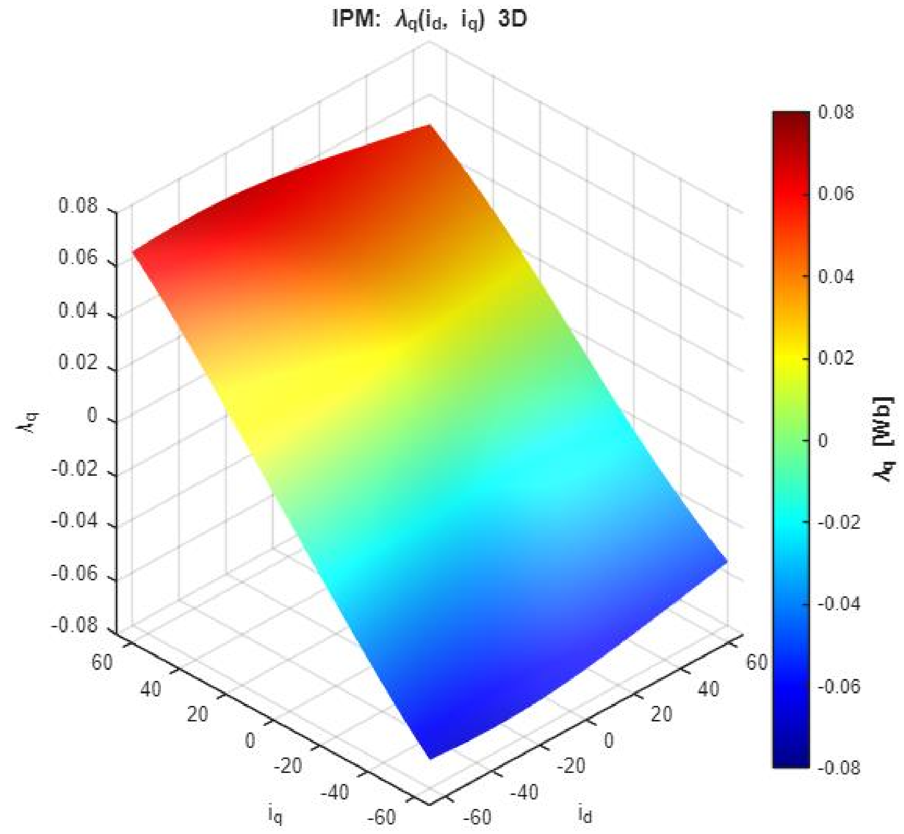

Figure 5.8– 3D Comparison of λ_q *flux surfaces for AF-IPM*

5.2 Comparative Analysis of Operating Trajectories

The analysis proceeds to the identification of the optimal operating current trajectories. The goal is to maximize the torque output within the supply's rated current limit ($I_{max} = 63\ A$) and the available DC bus voltage (400 V). The resulting operating loci in the d-q plane provide crucial insights into the machine's behavior, particularly regarding the saturation effects and the operating range limits.

5.2.1 MTPA Strategy and Saturation Impact

The Maximum Torque Per Ampere (MTPA) trajectory represents the locus of operating points that maximizes the electromagnetic torque per unit stator current. Theoretically, for a non-salient Surface-Mounted AF-PM machine ($L_d = L_q$), the reluctance torque is zero, and the optimal strategy is to align the current vector entirely with the q-axis ($i_d = 0$). However, the FEA results for the proposed AF-SPM reveal a deviation from this ideal behavior. As shown in Fig. 5.9, at high current levels, the optimal trajectory shifts slightly towards the second quadrant ($i_d < 0$). To investigate the root cause of this anomaly, a validation test was performed using an ideal ferromagnetic material (infinite permeability, non-saturating) in the Flux simulation. The comparison is presented in Fig. 5.10.

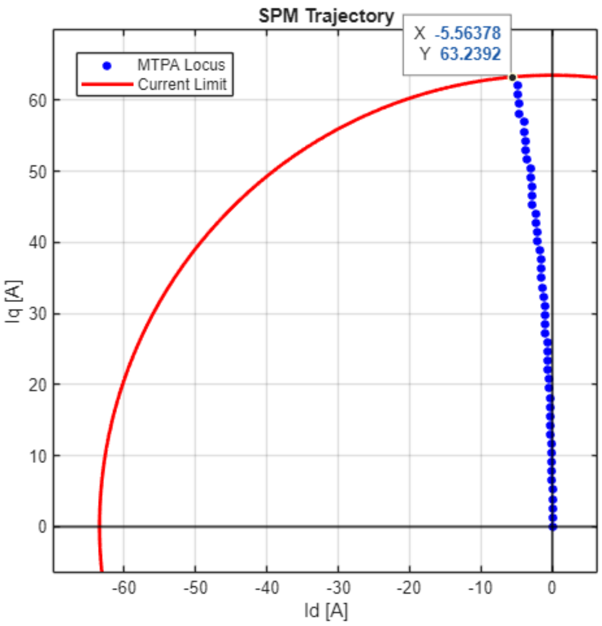

Figure 5.9 – MTPA Locus AF-SPM machine

Linear Iron: The trajectory lies perfectly on the q-axis ($i_d = 0$), confirming that the geometry itself is non-salient.

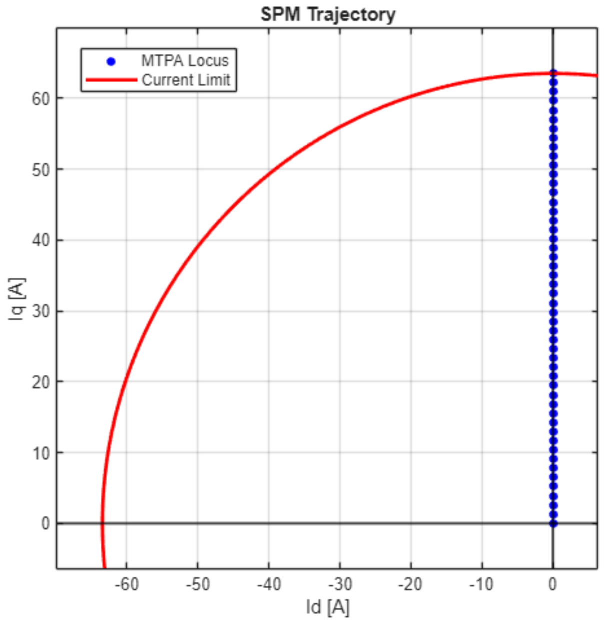

Figure 5.10 – MTPA Locus AF-SPM machine (Ideal iron)

This comparison confirms that the negative i_d requirement is purely driven by stator saturation. Since the high i_q saturates the teeth, injecting a small demagnetizing current ($i_d < 0$) helps to "unload" the iron, recovering permeability and thus maximizing the torque output.

The Interior Permanent Magnet configuration exhibits the expected hyperbolic trend in the second quadrant (Fig. 5.11). Unlike the AF-SPM, this behavior is structural and dominant. The algorithm actively injects a significant negative i_d component to exploit the saliency ratio ($L_q > L_d$), summing the reluctance torque contribution to the magnet alignment torque.

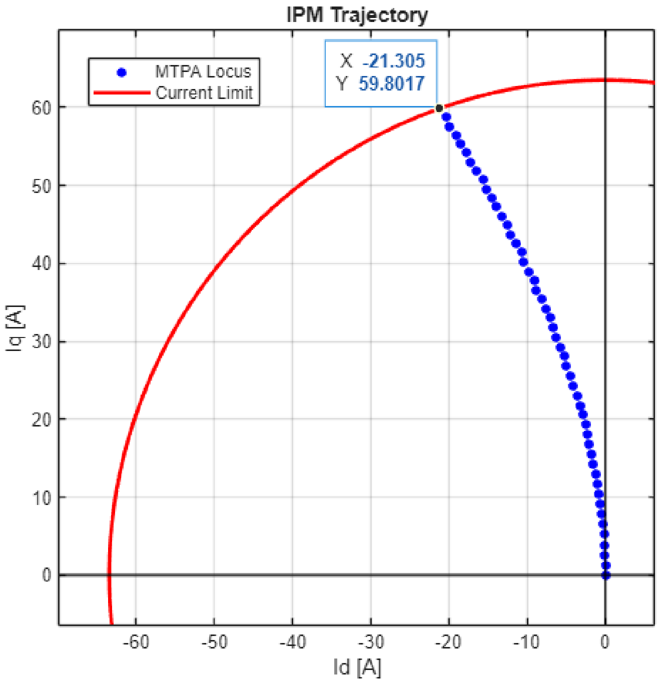

Figure 5.11 – MTPA Locus AF-IPM machine

5.3 Comparative Performance Analysis at Rated Current

This section presents mechanical performance of two prototypes evaluated under rated conditions ($I_{rms} = 63\ A$). The analysis focuses on torque and power envelopes across the entire speed range, validating numerical models and highlighting the trade-offs between the two topologies.

5.3.1 Torque-Speed Characterization and Model Validation

The comparative results are presented in Fig. 5.12, which compares torque-speed envelopes of both the AF-SPM and AF-IPM machines. The analysis reveals distinct behaviors driven by specific rotor anisotropy. In the constant torque region (base speed range), AF-SPM exhibits a higher average torque output compared to AF-IPM. This advantage is attributable to rotor architecture: surface-mounted magnets face the air-gap directly, maximizing the fundamental air-gap flux density without the leakage associated with the iron bridges of AF-IPM structure. Consequently, at rated current of 63 A, the direct magnet alignment torque of the AF-SPM prevails. However, as the rotational speed increases and the voltage limit is reached, the situation reverses. The AF-IPM demonstrates superior flux-weakening capabilities, sustaining a higher torque level for a wider speed range. Thanks to its saliency ($L_q > L_d$), the AF-IPM configuration exploits a significant reluctance torque component that persists even as the magnet flux is weakened to stay under voltage limit. In contrast, the AF-SPM torque drops more precipitously after the base speed, as it relies exclusively on the magnet interaction, which is strictly limited by the available voltage.

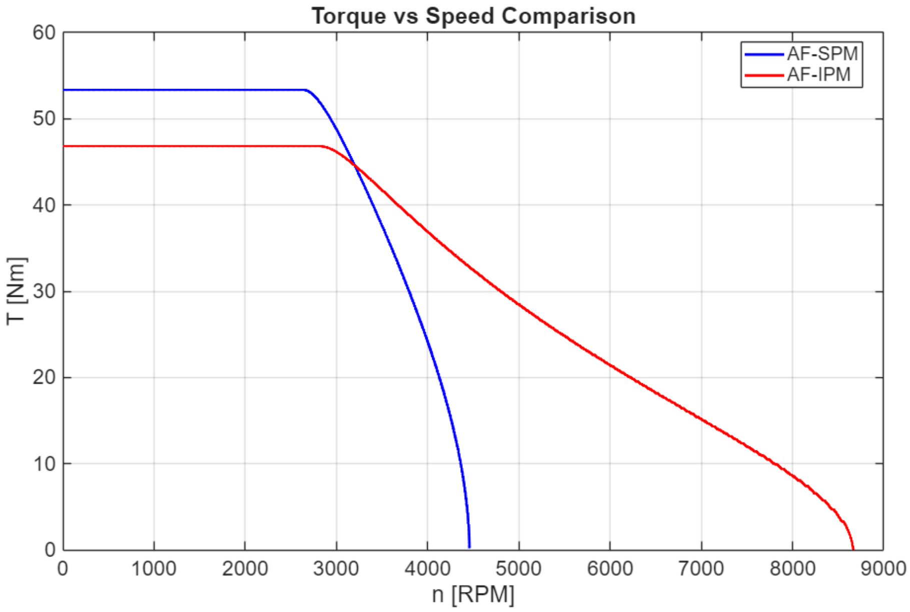

Figure 5.12 - Torque-Speed characteristics comparison at rated current (63 A)

As detailed in Table 5.1, the comparison highlights a clear trade-off between peak torque and flux-weakening capability. Thanks to its higher fundamental magnet flux, the AF-SPM delivers a 12.2% higher peak torque (53.3 Nm vs. 46.8 Nm). Conversely, the AF-IPM exhibits a vastly extended high-speed range: while its base speed is only 8.4% higher, its maximum speed reaches 8660 rpm, representing a massive +94.3% increase over the AF-SPM limit (4450 rpm).

Table 5.1: Torque comparison

Parameter	AF-SPM	AF-IPM	Variation (%)
Peak Torque [Nm]	53.3	46.8	-12.2
Base Speed [rpm]	2730	2960	+8.4
Max speed [rpm]	4450	8660	+94.3

5.3.2 Power-Speed Profiles

The mechanical power characteristics, derived from the torque profiles, are reported in Fig. 5.13 and quantitatively detailed in Table 5.3. Interestingly, despite the AF-SPM's initial advantage in absolute torque, both machines achieve a remarkably similar peak power near base speed, with the AF-IPM delivering 15.47 kW compared to the AF-SPM's 15.38 kW (+0.6%). However, as the rotational speed increases, the AF-IPM topology demonstrates a clear superiority in maintaining useful power delivery, whereas the AF-SPM output declines rapidly. This broader operating range results in a +13.7% higher average power for the AF-IPM across the speed envelope (10.57 kW versus 9.30 kW). A critical observation must be made regarding the CPSR. As previously seen from the operating trajectories, true MTPV operation is not reached under these nominal constraints. Because the rated stator current is insufficient to completely counteract the permanent magnet flux, an asymptotically flat constant power region is absent. Consequently, both power curves eventually peak and progressively decrease. Nevertheless, even within this restricted flux-weakening regime, the structural advantage of the AF-IPM is evident: it sustains its power output within the defined CPSR band for 1926 rpm, representing a massive +308.1% extension compared to the narrow 472 rpm range exhibited by the AF-SPM.

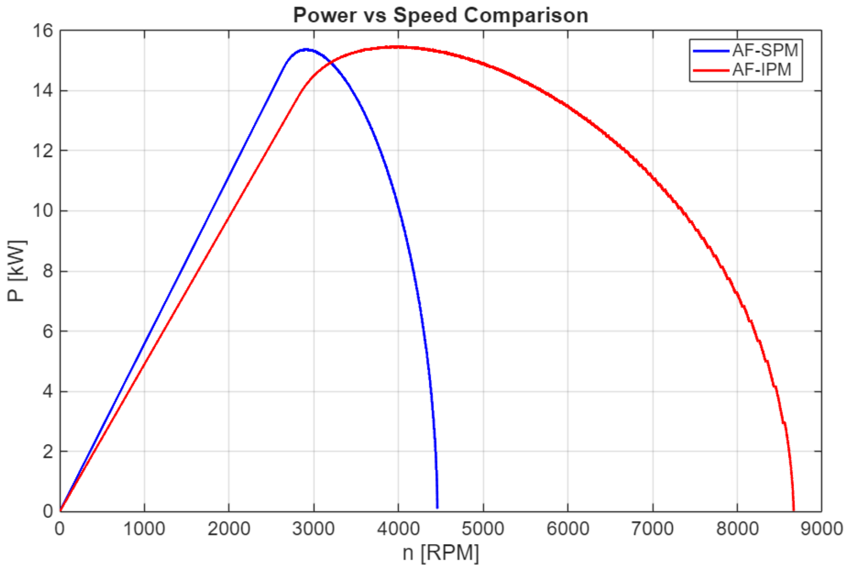

Figure 5.13- Power-Speed characteristics comparison at rated current (63 A)

Table 5.2: Power comparison

Parameter	AF-SPM	AF-IPM	Variation (%)
Peak power [kW]	15.38	15.47	+0.6
Average power [kW]	9.30	10.57	+13.7
CPSR range [rpm]	472	1926	+308.1

5.3.3 Flux-Weakening and MTPV trajectory evaluation

As the rotational speed increases above the base speed, the back-EMF rises, and the voltage limit constraint forces the current vector to move along the current limit circle or, if reachable, the Maximum Torque Per Voltage (MTPV) trajectory. According to the comprehensive review of flux-weakening techniques presented in [14], assuming a linear magnetic model, the voltage limit describes a family of ellipses in the d-q plane governed by the equation:

$$V_{lim}^2 \geq \omega^2 \left[\left(\lambda_{pm} + L_d\, I_d \right)^2 + \left(L_q\, I_q \right)^2 \right] \tag{5.1}$$

The center of these ellipses is located on the negative real axis at the coordinates $C = \left(- \lambda_{pm} / L_d, 0 \right)^2$. The magnitude of the current corresponding to this center is defined as the Characteristic Current (I_{ch}), which represents the theoretical short-circuit current required to completely nullify the magnet flux:

$$I_{ch} = \frac{\lambda_{pm}}{L} \tag{5.2}$$

It is important to note that the classical formulation above assumes constant inductance parameters. However, as demonstrated by the flux maps in Section 5.1, the inductance L_d is subject to saturation and cross-coupling effects, making it a function of the operating point. Consequently, the characteristic center C is not a fixed geometric point but shifts dynamically as the current vector changes. Nevertheless, for the purpose of this feasibility analysis, the linear approximation remains valid since the resulting I_{ch} magnitude provides a clear classification of the machine behavior.

The relationship between this characteristic current and the supply's maximum current I_{max} is the fundamental factor determining the theoretical speed range of the drive. As illustrated in the classification diagrams adapted from [14] and reported in Fig. 5.14, two distinct operating conditions exist. If the center C lies inside the current limit circle ($I_{ch} \leq I_{max}$), the drive can reach the MTPV operation point where the total stator flux is minimized, theoretically allowing the maximum power to be maintained indefinitely. Conversely, if the center lies outside the current limit circle ($I_{ch} > I_{max}$), the voltage ellipse becomes tangent to the current circle at a specific maximum speed ω_{max}; above this threshold, no intersection exists between the voltage and current limits, forcing the torque to drop to zero.

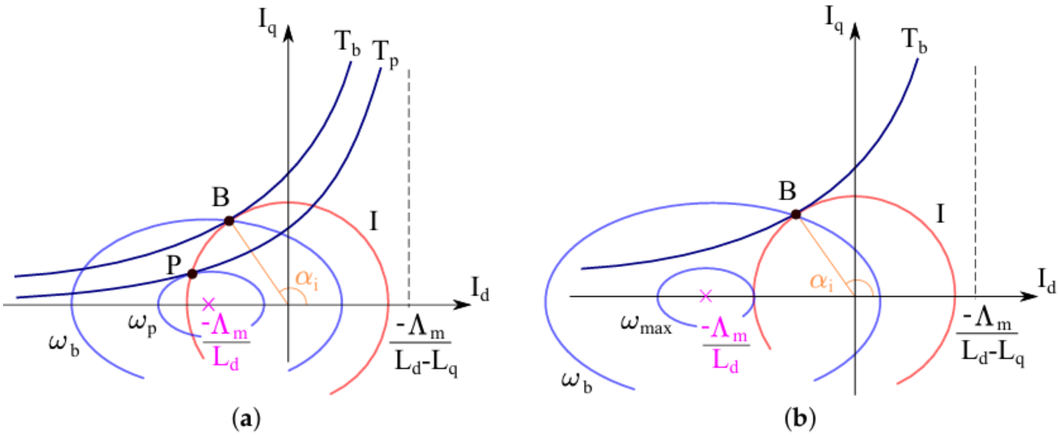

Figure 5.14 - Geometric classification of Flux-Weakening regions in the d-q plane. (a): ($I_{ch} \leq I_{max}$); (b): ($I_{ch} > I_{max}$)

This geometric condition directly dictates the mechanical output. As highlighted in Fig. 5.15, a machine satisfying the condition $I_{ch} \leq I_{max}$ (Fig. 5.14(a)) is capable of reaching the MTPV trajectory, thus maintaining a wide and flat CPSR. Conversely, when the characteristic current exceeds the rated limit ($I_{ch} > I_{max}$, as in Fig. 5.14 (b)), the machine experiences a sharp power drop at high speeds. Because the voltage limit restricts the current to its maximum circle, the permanent magnet flux cannot be completely weakened, causing the power output to decrease.

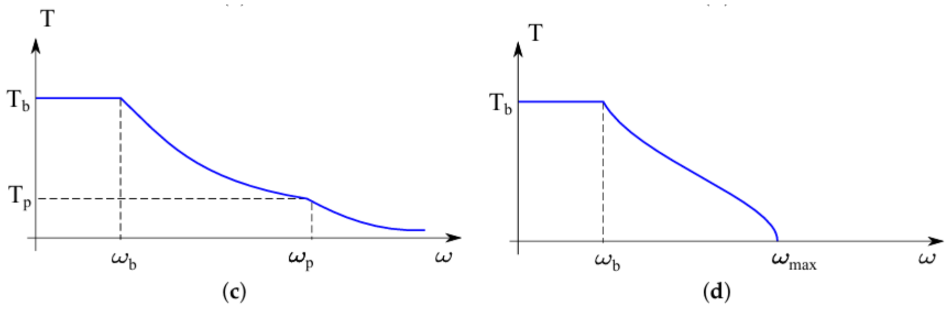

Figure 5.15 – Comparison of mechanical characteristics [14]

Applying this analytical framework to the proposed AF-SPM and AF-IPM designs, the calculation yields a characteristic current significantly larger than the rated limit $I_{ch} \gg I_{max}$. Since the characteristic point falls well outside the operating domain, neither machine can reach the asymptotic MTPV region. Consequently, the power delivery will inevitably drop once the voltage limit becomes dominant along the current circle. This diagnosis is visually confirmed by the specific operating trajectories simulated, presented in Fig. 5.16 and Fig. 5.17. In both diagrams, the hypothetical center of the voltage ellipses (C) is marked, highlighting its position well beyond the supply's rated current limit. For the AF-SPM, the trajectory tracks the limit circle without ever approaching the stability point. Similarly, despite the AF-IPM's ability to exploit the second quadrant for reluctance torque, its characteristic point remains unreachable. This confirms that, under these specific constraints, both topologies operate in the condition where an extended constant power region is physically unachievable.

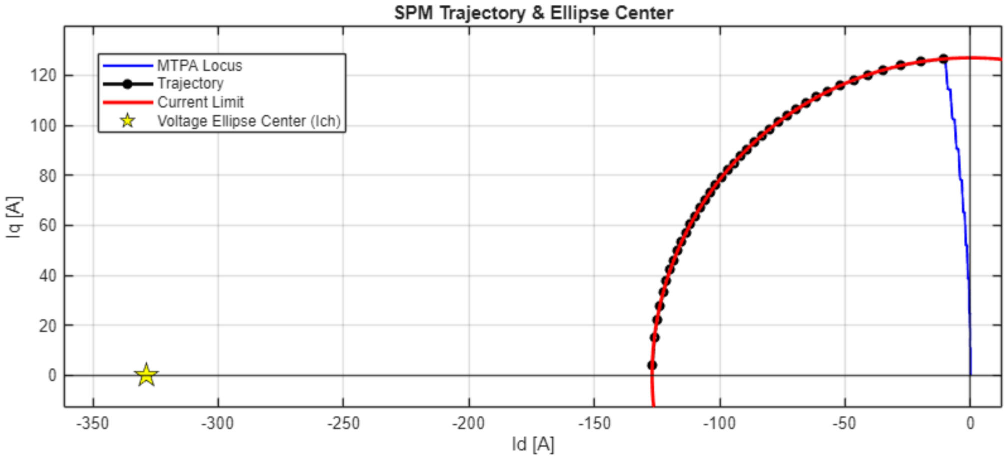

Figure 5.16 - Flux-Weakening analysis for the AF-SPM (63 A)

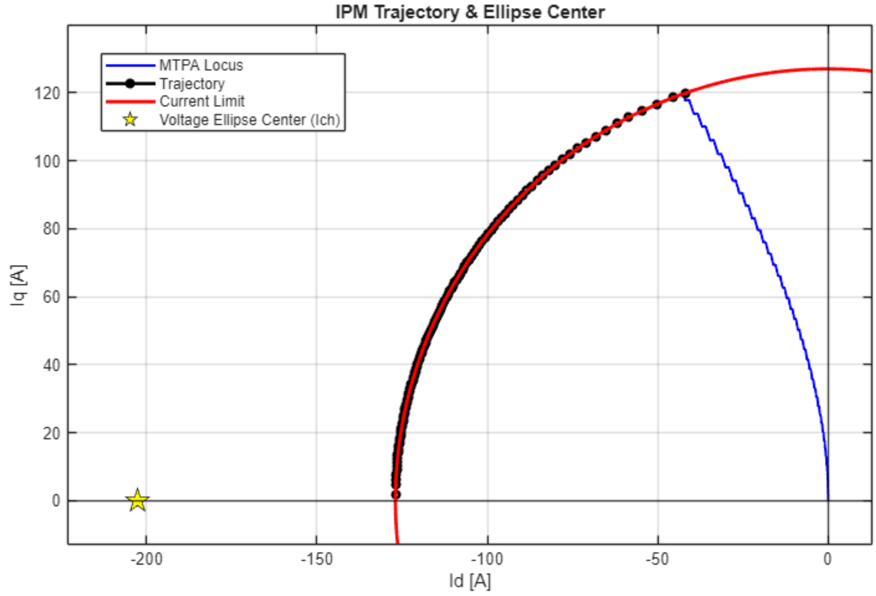

Figure 5.17 - Flux-Weakening analysis for the AF-IPM (63 A)

To achieve a wider Constant Power Speed Range (CPSR) and enable MTPV capabilities, the condition $\lambda_{pm} / L_d < \mathrm{I}_{max}$ must be satisfied. Based on the theoretical framework reviewed in [14], three main design strategies can be identified to effectively move the characteristic point C inside the current circle:

1. Increasing the d-axis Inductance (L_d): This parameter can be modified by altering the rotor geometry. For the AF-IPM topology, adjusting the magnet inclination or the V-shaped angle can increase the reluctance path along the d-axis, effectively increasing L_d.

2. Increasing the Current (I_{max}): If the machine electromagnetic design is fixed to maximize torque density, the operating envelope can be expanded by increasing the drive's current capability to encompass the characteristic point C.

The second strategy was selected for further investigation. While the following section presents the performance at the rated current (63 A) a subsequent analysis (Section 5.4) will explore the machine's behavior under a hypothetical peak current condition, set to double the nominal value (126 A). This test aims to satisfy the condition $\mathrm{I}_{max} > \lambda_{pm} / L_d$, thereby unlocking the high-speed MTPV potential discussed in the theoretical analysis.

5.4 Peak Performance

High-performance automotive applications often demand operating points well beyond the continuous rating to handle peak acceleration. Consequently, to simulate a severe stress condition and attempt to verify the reachability of the MTPV region, the supply current limit was theoretically doubled to 126 A. This scenario aims to satisfy the condition $I_{ch} \leq I_{max}$, potentially becomes possible to reach the MTPV trajectory and assess the resulting extension of the CPSR.

5.4.1 Expanded current Trajectories

The impact of expanding the current limit reveals a fundamental divergence between the two topologies, driven by their distinct magnetic parameters and saturation behaviors. By doubling the operating radius to 126 A, the current limit circle covers a significantly larger area of the second quadrant, yet the geometric outcome and the resulting strategy differ drastically for the two machines. Starting with the AF-SPM, the simulation highlights severe impact of magnetic saturation on the current trajectory. Theoretically, a surface-mounted machine should operate with the current vector aligned along the q-axis ($I_d = 0$). However, at this elevated current level, the stator teeth experience deep saturation, altering the magnetic linearity. As a result, the MTPA locus deviates significantly from the vertical axis, requiring a substantial negative d-axis current component to maximize torque density even before the voltage limit is reached. Despite this expanded operating capability, the geometric limitation remains the critical bottleneck. Due to the large effective air-gap characteristic of the surface-mounted topology, the d-axis inductance L_d is intrinsically low. According to the definition $I_{ch} = \lambda_{pm} / L_d$ this results in an extremely high characteristic current. Consequently, even with the supply current doubled to 126 A, the characteristic center remains situated well outside the reachable operating domain. The operating trajectory extends further into the flux-weakening region compared to the nominal case, the voltage ellipses eventually detach from the current limit circle, preventing the attainment of the asymptotic MTPV region as shown in Fig. 5.18.

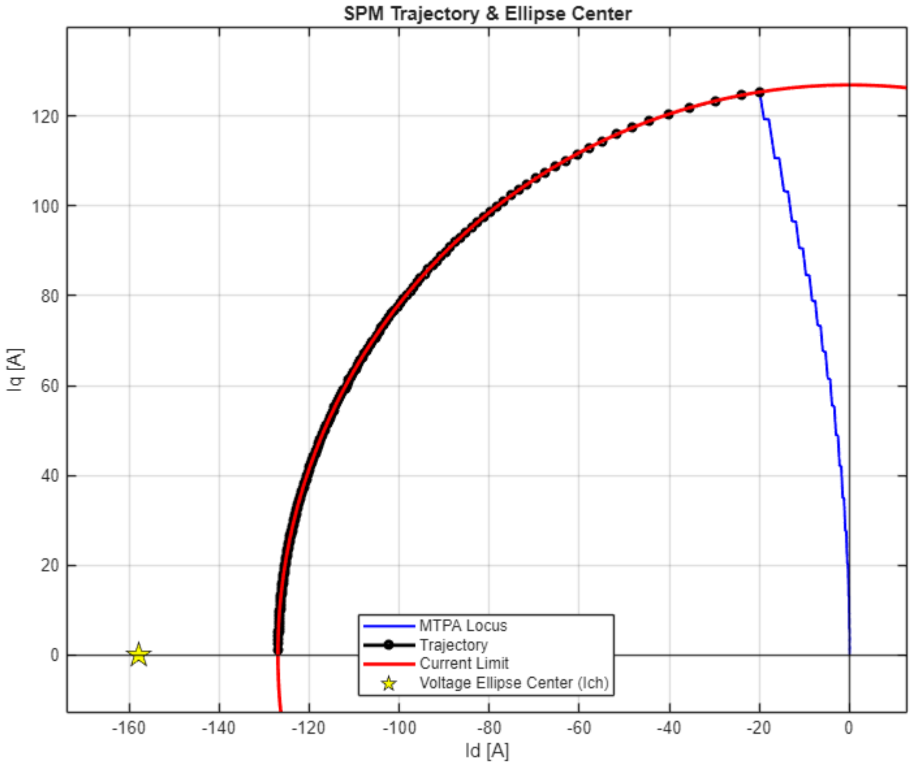

Figure 5.18- Operating trajectory for the AF-SPM (126 A)

In contrast, the AF-IPM presents a radically different scenario, effectively leveraging its rotor anisotropy to overcome the speed limit. The interior permanent magnet structure naturally offers a higher d-axis inductance compared to the surface-mounted counterpart, thanks to the reluctance paths defined by the rotor geometry. This higher inductance yields a significantly lower characteristic current I_{ch}. When the supply capability is increased to 126 A, the current limit circle becomes large enough to approach the characteristic center as shown in Fig. 5.19. The algorithm can now inject sufficient demagnetizing current to completely nullify the magnet flux, allowing the operating point to track the MTPV trajectory (the constant flux hyperbola) indefinitely. Unlike the AF-SPM, which is forced to stop generating torque once the voltage limit is hit, the AF-IPM can modulate the flux linkage dynamically to stay within the voltage ellipse, theoretically unlocking an unlimited speed range subject only to mechanical constraints.

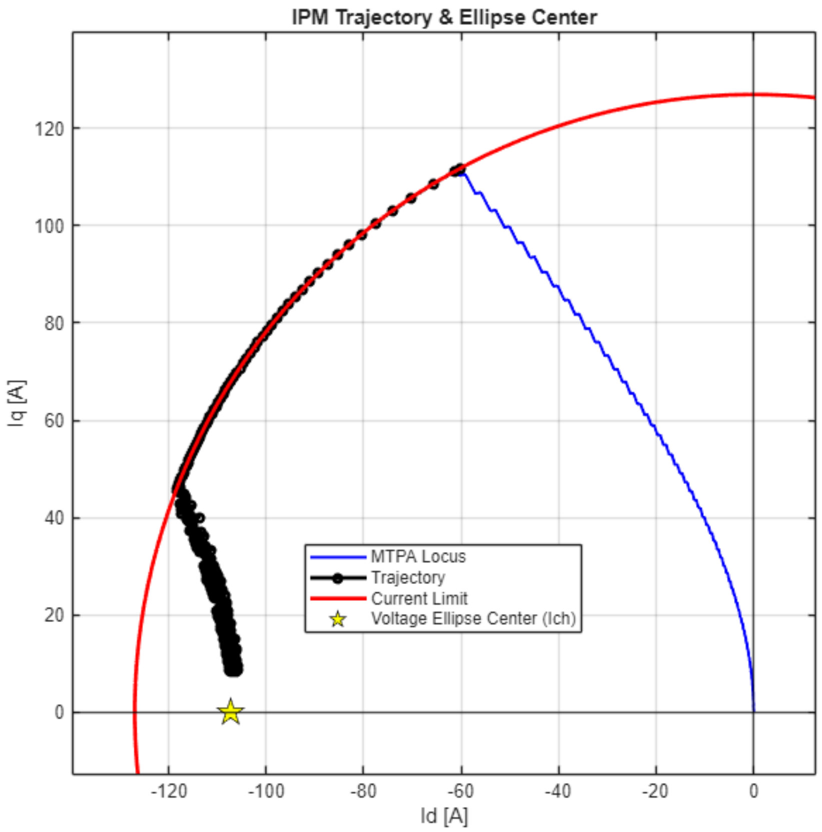

Figure 5.19 - Operating trajectory for the AF-IPM (126 A)

5.4.2 Torque-Speed Characteristics

In the torque-speed envelopes shown in Fig. 5.20, and detailed in Table 5.3, the AF-SPM continues to exhibit a higher absolute peak torque of 101.2 Nm, outperforming the AF-IPM (88.4 Nm) by 12.7%. This advantage is driven by the direct magnetic interaction of the surface-mounted topology. However, due to the heavy magnetic saturation of the stator core at these high excitation levels (126 A), the output torque for both machines does not scale linearly with the current increase. Despite this saturation, the AF-SPM maintains its torque advantage during the initial acceleration phase, with both machines sharing nearly identical base speeds (2600 rpm for the SPM and 2620 rpm for the IPM).

As the rotational speed increases, the superior flux-weakening capability of the Interior Permanent Magnet design becomes the dominant factor. While the AF-SPM torque profile extends significantly further compared to the nominal case, reaching a maximum speed of 13,921 rpm, it is limited by the supply constraints, forcing the torque to drop to zero without entering a constant power region. In contrast, the AF-IPM successfully reaches the MTPV limit. Thanks to the accessible characteristic center, the AF-IPM torque decays smoothly following the theoretical $1/\omega$ proportionality. This specific trajectory allows the AF-IPM to easily reach 20,000 rpm, representing a +43.7% extension over the AF-SPM boundary. Notably, since 20,000 rpm represents the algorithmic upper limit set for the simulation, this confirms that the high current condition allows the AF-IPM to sustain operation almost indefinitely along the constant power hyperbola.

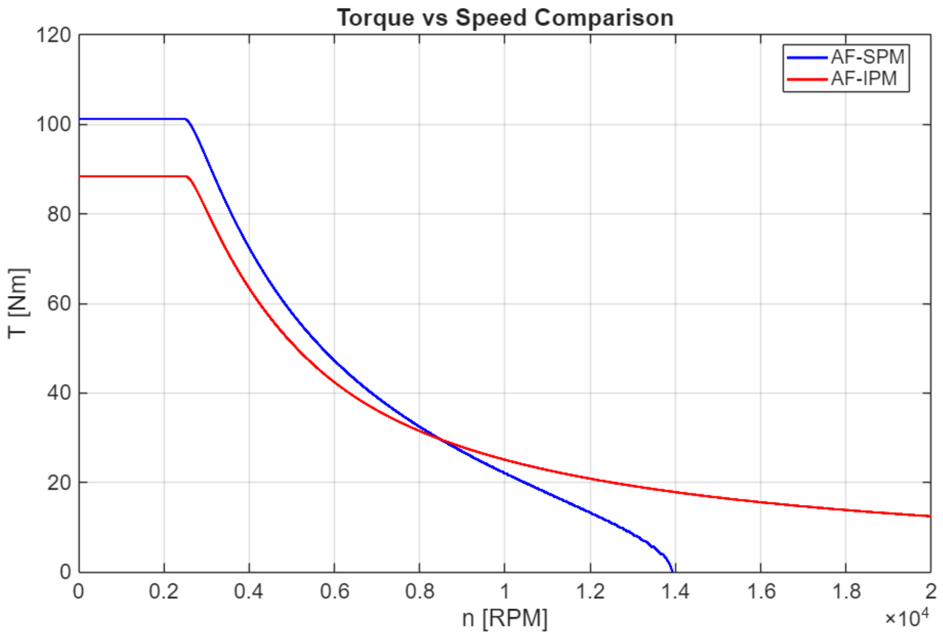

Figure 5.20 - Torque-Speed characteristics comparison (126 A)

Table 5.3: Torque comparison at peak condition

Parameter	AF-SPM	AF-IPM	Variation (%)
Peak Torque [Nm]	101.2	88.4	-12.7
Base Speed [rpm]	2600	2620	+0.8
Max speed [rpm]	13921	20000	+43.7

5.4.3 Power-Speed Characteristics and CPSR

The most significant improvement is observed in the power delivery profile, presented in Fig. 5.21. At rated current, the power curve was characterized by a peak followed by a rapid roll-off. Under peak conditions, the behavior changes drastically. The AF-IPM now exhibits a distinct CPSR. After reaching the peak power at base speed, the output remains relatively flat for a wide frequency range. This plateau indicates that the machine has successfully entered or approached the MTPV region, where the voltage limit and current limit allow for a constant energy conversion rate. This result validates the theoretical hypothesis: the electromagnetic design of the AF-IPM is capable of sustaining an extended, theoretically unlimited constant power region, provided that the supply system is sized correctly to reach the characteristic current required for complete flux cancellation. Although this condition theoretically allows the speed to approach infinity, such extreme velocities are mechanically unfeasible. Therefore, a maximum limit of 20,000 rpm was set for the simulation. Conversely, although the AF-SPM benefits from the increased current, its inherently lower inductance prevents it from maintaining a flat power profile.

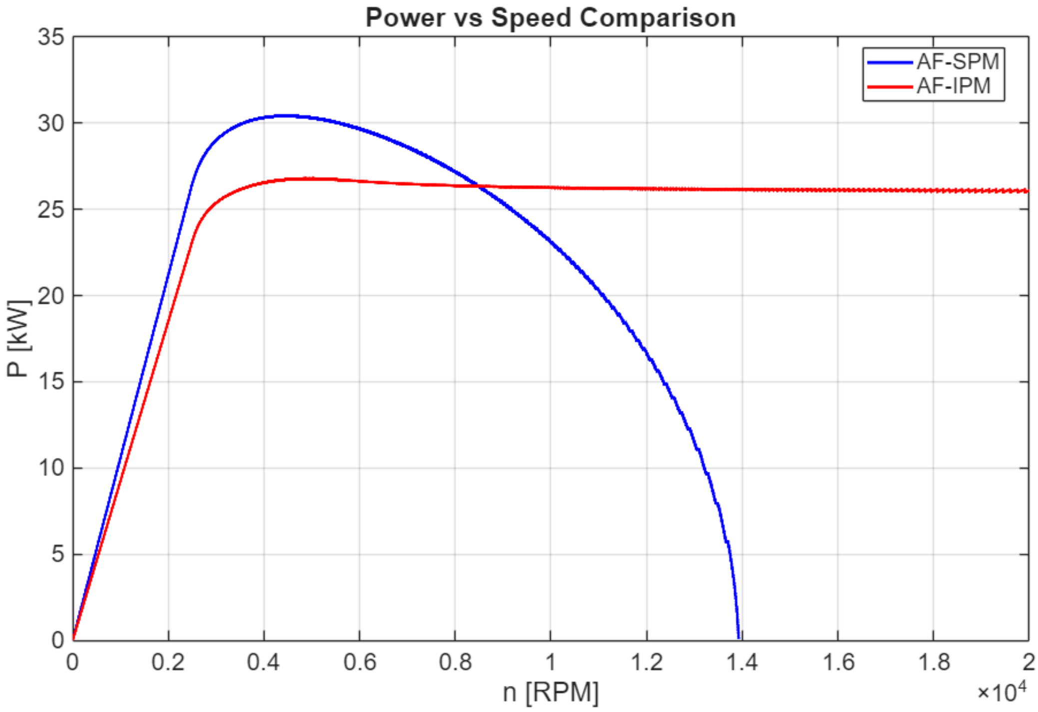

Figure 5.21 – Power-Speed characteristics comparison (126 A)

The data presented in Table 5.4 provides a comprehensive quantitative assessment of the power delivery profiles for both topologies under peak current conditions. The results highlight a fundamental trade-off between absolute peak performance and high-speed power retention.

The AF-SPM exhibits a superior peak power of 30.44 kW, outperforming the AF-IPM (26.80 kW) by 11.9%. Conversely, the AF-IPM reveals its structural superiority in the flux-weakening region.

Although the AF-IPM electromagnetic design theoretically allows unlimited speed, such values are mechanically unrealistic. Therefore, a maximum limit of 20,000 rpm was imposed for a meaningful comparison.

The interior magnet design achieves a massive Constant Power Speed Range (CPSR) of 17,377 rpm. This represents an extraordinary +385.5% extension compared to the narrow 3,579 rpm range of the AF-SPM.

Ultimately, this vastly extended operating envelope translates into a higher overall energy delivery across the speed spectrum. Despite having a lower initial peak, the AF-IPM achieves an average power of 24.39 kW throughout the evaluated speed range, marking a +10.8% improvement over the AF-SPM (22.01 kW).

Table 5.4: Power comparison at peak condition

Parameter	AF-SPM	AF-IPM	Variation (%)
Peak power [kW]	30.44	26.80	-11.9
Average power [kW]	22.01	24.39	+10.8
CPSR range [rpm]	3579	17377	+385.5

6 Conclusions

The primary objective of this thesis was to perform a comprehensive comparative study between an AF-SPM and an AF-IPM, specifically intended for traction applications. The investigation was conducted using high-fidelity 3D Finite Element Analysis (FEA) coupled with a MATLAB® environment for the computation of optimal operating trajectories. By imposing strict parity conditions on the stator geometry and electrical constraints, the research succeeded in isolating the effects of rotor anisotropy and validating the potential of the V-shaped topology. The analysis of the results highlights distinct behaviors for the two topologies depending on operating speed and load conditions.

Under nominal rating conditions, the AF-SPM exhibits superior torque capability in the base-speed region due to the direct interaction between the magnets and the air-gap, which maximizes magnetic flux linkage. However, as the rotational speed increases, the superior flux-weakening capability of the AF-IPM becomes evident. The interior magnet topology maintains higher torque levels deep into the field-weakening region and achieves a higher maximum speed compared to the surface-mounted counterpart. Nevertheless, it is important to note that under these specific nominal constraints, neither machine reaches the MTPV trajectory. Because the available stator current is insufficient to completely counteract the permanent magnet flux, both machines possess a strict theoretical speed limit. This behavior is dictated by the intrinsic geometric characteristics of the two machines, specifically the combination of permanent magnet flux linkage and inductance values, which places the characteristic center of the voltage limit ellipses outside the current limit circle. Despite the inability to reach the MTPV trajectory under nominal conditions, the AF-IPM still demonstrates a distinct advantage. It exhibits a more gradual power drop-off and maintains significantly higher power delivery at high speeds compared to the AF-SPM. To overcome the limitations of the rated scenario, the investigation was extended to a Peak Performance condition by doubling the supply current limit. Although both machines are strictly constrained by the same maximum supply voltage at high speeds, their responses differ significantly. Due to its inherently low d-axis inductance, the AF-SPM cannot sufficiently counteract the permanent magnet flux, failing to achieve a constant power plateau even at elevated currents. Conversely, the AF-IPM successfully achieves deep flux-weakening operation. The expanded current capability allows the limit circle to encompass the characteristic center of the voltage ellipses, effectively unlocking the MTPV region and enabling an extended Constant Power Speed Range. This result confirms that the structural complexity of the V-shaped rotor is fully justified by its flux-weakening capability, identifying it as a valid and competitive candidate for traction applications requiring wide operating speed ranges. In conclusion, this thesis validates the V-shaped axial flux concept, confirming that while the AF-SPM remains the optimal choice for low-speed duty, the proposed AF-IPM represents a robust alternative for high-performance traction requiring extended speed ranges.

While the electromagnetic characterization presented in this thesis provides a robust validation of the proposed V-shaped topology, it is important to acknowledge that the analysis was restricted to a single specific rotor geometry. A natural progression of this research would be a comprehensive parametric study or an automated design optimization aimed at exploring the vast design space of the V-shaped rotor. Future investigations could systematically vary critical geometric parameters such as the magnet inclination angle, the iron bridge thickness and the magnet dimensionss. As demonstrated in recent literature [1], such optimization processes could further improve the saliency ratio and torque density, potentially leading to even more competitive results compared to the baseline design adopted in this study.

Furthermore, to move towards a complete drive system design, the scope of the analysis should be expanded beyond the torque-speed capabilities. Future works should include a detailed evaluation of total losses, specifically focusing on the magnet eddy current losses which can be critical in high-speed axial flux machines. This data would form the basis for a dedicated thermal management study to ensure safe operation under the peak performance conditions identified. Finally, generating complete efficiency maps over the entire operating range would provide a definitive assessment of the energy consumption trade-offs between the Surface-Mounted and Interior Permanent Magnet architectures in real-world driving cycles.

Appendix

Matlab script 1 (master.m)

```
%  MASTER script for mapping (SPM & IPM)
%  Runs FEM simulations via Flux to map the motor.
%  Results are saved in .mat files.
clc; clear; close all;
tStart = tic;

%% 1. SIMULATION CONFIGURATION
% Select motor: 0 = SPM, 1 = IPM
MOTOR_TYPE = 1;

% Common Parameters
% Path to the Flux project
WORKPATH    = 'C:/Users/s332855/luca_mandrile/matlab/axial_motor';
max_retries = 3;     % Max solver attempts
pp          = 6;     % Pole pairs
n_sim       = 1500;  % FEM Speed

% --- DYNAMIC CONFIGURATION ---
if MOTOR_TYPE == 0
    % SPM Setup
    disp('*** START: SPM (Surface PM) ***');
    proj_name    = 'SPM_load';
    out_file     = 'Dati_Motore_SPM.mat';
    solver_func  = @SPM_solver;
    phase_offset = 30.19;

    % Simulation Vector
    theta_tot = -2 : 2 : 10;

elseif MOTOR_TYPE == 1
    % IPM Setup
    disp('*** START: IPM (Interior PM) ***');
    proj_name    = 'IPM_load';
    out_file     = 'Dati_Motore_IPM.mat';
    solver_func  = @IPM_solver;
    phase_offset = 30.01;

    % Simulation Vector
    theta_tot = -2 : 2 : 10;

else
    error('Invalid Motor Selection (0 or 1).');
end

%% 2. INITIALIZATION
% Discard the first point (transient)
theta_vec = theta_tot(2:end);
theta_el  = theta_vec * pp;
Rs        = 0.0451;

% Clarke Matrix
Clarke_Mat = [2/3, -1/3, -1/3; ...
              0, sqrt(3)/3, -sqrt(3)/3];

% --- Current Grid Setup ---
```

```
% Max Current Calculation (~63 A)
Imax_tot = 7.43 * 72.5 * sqrt(2);
Imax     = Imax_tot / 12;


% Grid Density
I_div  = 4;
I_step = Imax / I_div;
Id_vec = -Imax : I_step : Imax;
Iq_vec = -Imax : I_step : Imax;

% Simulation Counters
n_points_sim = length(Id_vec) * length(Iq_vec);
s_count      = 0;

% Pre-allocation (Maps)
sz_q   = length(Iq_vec);
sz_d   = length(Id_vec);
fd_map = zeros(sz_q, sz_d);
fq_map = zeros(sz_q, sz_d);
T_map  = zeros(sz_q, sz_d);
TR_map = zeros(sz_q, sz_d);

% Pre-allocation (Temp Vectors)
num_steps = length(theta_vec);
fd_tmp    = zeros(1, length(theta_el));
fq_tmp    = zeros(1, length(theta_el));
A         = zeros(num_steps, 3);
B         = zeros(num_steps, 1);

%% 3. MAIN SIMULATION LOOP
fprintf('Starting Scan (%d points)...\n', n_points_sim);

for i = 1:length(Iq_vec)
    Iq = Iq_vec(i);

    for j = 1:length(Id_vec)
        Id = Id_vec(j);

        retry   = 0;
        success = false;

        % --- Solver Retry Loop ---
        while ~success && retry < max_retries
            try
                % Progress Display
                s_count = s_count + 1;
                fprintf('Sim %d/%d | Id=%.1f Iq=%.1f... ', ...
                        s_count, n_points_sim, Id, Iq);

                % CALL SOLVER FUNCTION
                [tmp_A, tmp_B] = solver_func(WORKPATH, proj_name, ...
                                             theta_tot, n_sim, Id, Iq);

                % --- Data Parsing (Flux string format) ---
                % Flux outputs data starting from specific rows
                row_start_A = 22;
                row_start_B = 18;

                for k = 1:num_steps
                    % Extract 3-Phase Flux
                    r_A   = row_start_A + k - 1;
                    str_A = string(tmp_A{r_A, 1});
                    val_A = str2num(str_A);
```

```
                    % Extract Torque
                    r_B   = row_start_B + k - 1;
                    str_B = string(tmp_B{r_B, 1});
                    val_B = str2num(str_B);

                    % Store valid data
                    if length(val_A) >= 4
                        A(k, :) = val_A(2:4); % Cols 2,3,4
                        B(k, :) = val_B(2);   % Col 2
                    end
                end

                fprintf('OK.\n');
                success = true;

            catch ME
                retry = retry + 1;
                fprintf('\nError (Attempt %d): %s\n', retry, ME.message);
            end
        end

        if ~success, error('Sim failed after max retries.'); end

        % --- Post-Processing (Park Transform) ---
        fa = A(:,1); fb = A(:,2); fc = A(:,3);

        for k = 1:length(theta_el)
            if k > length(fa), break; end

            % Rotation Matrix (using phase offset)
            ang = theta_el(k) + phase_offset;
            Rot = [cosd(ang),  sind(ang); ...
                  -sind(ang),  cosd(ang)];

            % Transformations: ABC -> AlphaBeta -> DQ
            f_abc  = [fa(k); fb(k); fc(k)];
            f_ab   = Clarke_Mat * f_abc;
            f_dq   = Rot * f_ab;

            fd_tmp(k) = f_dq(1);
            fq_tmp(k) = f_dq(2);
        end

        % Fill Maps (Mean values for DC component)
        fd_map(i, j) = mean(fd_tmp);
        fq_map(i, j) = mean(fq_tmp);
        T_map(i, j)  = mean(B);
        TR_map(i, j) = max(B) - min(B); % Torque Ripple

        % Debug Print
        % fprintf('   Ld: %.4f | Lq: %.4f | T: %.2f\n', ...
        %          mean(fd_tmp), mean(fq_tmp), mean(B));
    end
end

%% 4. SAVE OUTPUT
time_min = toc(tStart) / 60;
fprintf('\n--- FINISHED ---\nTotal Time: %.2f min\n', time_min);
fprintf('Saving to: %s ... ', out_file);

% Save essential variables
save(out_file, 'fd_map', 'fq_map', 'T_map', 'TR_map');
fprintf('Done.\n');
```

Matlab script 2 (SPM_solver.m)

```
%  FUNCTION: SPM_solver
%  Interfacing with Altair Flux to solve the SPM motor model.
%
%  INPUTS:
%   WORKPATH     - Directory of the Flux project
%   fluxproject  - Name of the .FLU file
%   theta_vec_tot- Vector of rotor positions to simulate
%   n            - Speed [rpm]
%   Id, Iq       - Current components [A]
%
%  OUTPUTS:
%   tmp_A        - Flux linkage results (Cell array)
%   tmp_B        - Torque results (Cell array)

function [tmp_A, tmp_B] = SPM_solver(WORKPATH, fluxproject, ...
                                     theta_vec_tot, n, Id, Iq)

% --- Java/Network Configuration ---
% Fix IP to localhost to avoid network card conflicts
java.lang.System.setProperty('java.rmi.server.hostname', ...
                             '127.0.0.1');
qt = char(34); % ASCII double quotes

% --- Path Setup ---
LOAD_PATH   = fullfile(WORKPATH, [fluxproject '.FLU']);
dtheta      = 2;
theta_min   = min(theta_vec_tot);
theta_max   = max(theta_vec_tot);

% Output Plot Names
flux_plots   = 'results_flux';
torque_plots = 'result_torque';

% --- Working Directories ---
% INSTALLFLUX_PATH should be verified on the specific machine
INSTALLFLUX_PATH = 'C:\Program Files\Altair\2024.1\flux\Flux';

% String formatting for Jython
LOAD_PATH_MOD = ['"', LOAD_PATH, '"'];
match         = wildcardPattern + "\";
% Extract project name from path
PROJECT_NAME  = erase(LOAD_PATH, match);

% Define temporary save location
SAVE_PATH_MOD = fullfile(WORKPATH, [fluxproject '_1.FLU']);
SAVE_LOCATION = ['"', SAVE_PATH_MOD, '"'];

% --- Server & Classpath Setup (flux3d_mp.m) ---
installFlux = getenv('INSTALLFLUX');
if strcmp(installFlux,'')
    installFlux = INSTALLFLUX_PATH;
end

installJar = [installFlux, '/Api/jre8/'];

% Add required JARs to Java Dynamic Classpath
% (Broken into multiple lines for thesis width compliance)
javaaddpath({[installJar,'fluxmp.jar'], ...
             [installJar,'cedserver.jar'], ...
             [installJar,'CoreBoot.jar'], ...
             [installJar,'CoreBus.jar'], ...
```

```
             [installJar,'rsicore.jar'], ...
             [installJar,'CoreCommon.jar'], ...
             [installJar,'CedUtils.jar'], ...
             [installJar,'CssUtils.jar'], ...
             [installJar,'CssService.jar']});

import rsi.fluxmp.FMP.*

% --- Server Parameters ---
NUM_MEM_LABEL  = 'MEMSIZN3=';
CHAR_MEM_LABEL = 'MEMSIZC3=';
LANG_LABEL     = 'CAO_DEFLAN=';

% Debug Mode
RELEASEMODE = 0;
% Init Flux API
FMP_init(RELEASEMODE);

% --- Start Local Flux Server ---
% Allocating memory (approx 32GB)
args = {[NUM_MEM_LABEL, '32000000000'], [LANG_LABEL, '2']};
serverUid = FMP_startLocaleServer('FLUX3D', WORKPATH, args);

% --- Project Management ---
% Load Project
cmd_load = ['loadProject(', LOAD_PATH_MOD, ')'];
FMP_executeJythonCommand(serverUid, cmd_load);

% Save As (Temp)
cmd_save = ['saveProjectAs(', SAVE_LOCATION, ')'];
FMP_executeJythonCommand(serverUid, cmd_save);

% Delete previous results to avoid conflicts
cmd_del = 'DeleteAllResults(deletePostprocessingResults="yes")';
FMP_executeJythonCommand(serverUid, cmd_del);

% --- Scenario Definition ---
% Clear existing scenarios
FMP_executeJythonCommand(serverUid, 'Scenario[ALL].delete()');
FMP_executeJythonCommand(serverUid, 'Scenario(name="RES_FLUXPROJECT")');

% Add Pilot: Rotor Position (Dynamic Interval)
cmd_pilot_ang = ['Scenario["RES_FLUXPROJECT"].addPilot(', ...
    'pilot=MultiValues(parameter=VariationParameter["ANGPOS_ROTOR"],',...
    'intervals=[IntervalStepValue(minValue=', num2str(theta_min), ...
    ',maxValue=', num2str(theta_max), ...
    ',stepValue=', num2str(dtheta), ')]))'];
FMP_executeJythonCommand(serverUid, cmd_pilot_ang);

% Add Pilot: Id
cmd_pilot_id = ['Scenario["RES_FLUXPROJECT"].addPilot(', ...
    'pilot=MonoValue(parameter=VariationParameter["ID"], value=', ...
    num2str(Id), '))'];
FMP_executeJythonCommand(serverUid, cmd_pilot_id);

% Add Pilot: Iq
cmd_pilot_iq = ['Scenario["RES_FLUXPROJECT"].addPilot(', ...
    'pilot=MonoValue(parameter=VariationParameter["IQ"], value=', ...
    num2str(Iq), '))'];
FMP_executeJythonCommand(serverUid, cmd_pilot_iq);

% Add Pilot: Speed
cmd_pilot_spd = ['Scenario["RES_FLUXPROJECT"].addPilot(', ...
    'pilot=MonoValue(parameter=VariationParameter["SPEED"], value=', ...
    num2str(n), '))'];
```

```
FMP_executeJythonCommand(serverUid, cmd_pilot_spd);
% --- Define Output Curves ---

% 1. Flux Linkage Curves (Coils 1, 2, 3)
% (String broken for readability)
flux_formula =
'["FluxCoil(COILCONDUCTOR_1)","FluxCoil(COILCONDUCTOR_2)","FluxCoil(COILC
ONDUCTOR_3)"]';
cmd_res_flux = ['EvolutiveCurve2D(name="', flux_plots, '",', ...
    'evolutivePath=EvolutivePath(parameterSet=[', ...
    'SetParameterFixed(paramEvol=VariationParameter["ID"],', ...
    'currentValue=', num2str(Id), '),', ...
    'SetParameterFixed(paramEvol=VariationParameter["IQ"],', ...
    'currentValue=', num2str(Iq), '),', ...
    'SetParameterFixed(paramEvol=VariationParameter["SPEED"],', ...
    'currentValue=', num2str(n), '),', ...

'SetParameterXVariable(paramEvol=VariationParameter["ANGPOS_ROTOR"],',
...
    'limitMin=', num2str(theta_min), ...
    ',limitMax=', num2str(theta_vec_tot(end)), ')]),', ...
    'formula=', flux_formula, ')'];

% 2. Torque Curve
torque_formula = '["TorqueElecMag(ROTOR)"]';
cmd_res_trq = ['EvolutiveCurve2D(name="', torque_plots, '",', ...
    'evolutivePath=EvolutivePath(parameterSet=[', ...
    'SetParameterFixed(paramEvol=VariationParameter["ID"],', ...
    'currentValue=', num2str(Id), '),', ...
    'SetParameterFixed(paramEvol=VariationParameter["IQ"],', ...
    'currentValue=', num2str(Iq), '),', ...
    'SetParameterFixed(paramEvol=VariationParameter["SPEED"],', ...
    'currentValue=', num2str(n), '),', ...

'SetParameterXVariable(paramEvol=VariationParameter["ANGPOS_ROTOR"],',
...
    'limitMin=', num2str(theta_min), ...
    ',limitMax=', num2str(theta_vec_tot(end)), ')]),', ...
    'formula=', torque_formula, ')'];

% --- Solve ---
FMP_executeJythonCommand(serverUid, cmd_save);
cmd_solve = ['Scenario["RES_FLUXPROJECT"].solve(projectName=', ...
             SAVE_LOCATION, ')'];
FMP_executeJythonCommand(serverUid, cmd_solve);

% --- Post-Processing & Export ---
% Generate curves
FMP_executeJythonCommand(serverUid, cmd_res_flux);
FMP_executeJythonCommand(serverUid, cmd_res_trq);

% Define Export Paths (Dynamic, using WORKPATH)
% Note: Using forward slashes for Jython compatibility
clean_workpath = strrep(WORKPATH, '\', '/');
file_flux_out  = [clean_workpath, '/SPM_MTPV'];
file_trq_out   = [clean_workpath, '/SPM_MTPV_1'];

% Export Flux to TXT
cmd_exp_flux = ['CurveVariation2D["', flux_plots, '"].exportTXT(', ...
    'txtFile="', file_flux_out, '", mode="replace")'];
FMP_executeJythonCommand(serverUid, cmd_exp_flux);

% Export Torque to TXT
cmd_exp_trq = ['CurveVariation2D["', torque_plots, '"].exportTXT(', ...
    'txtFile="', file_trq_out, '", mode="replace")'];
```

```
FMP_executeJythonCommand(serverUid, cmd_exp_trq);

% Save Final State
FMP_executeJythonCommand(serverUid, cmd_save);

% --- Read Results into MATLAB ---
tmp_A = readcell(fullfile(WORKPATH, 'SPM_MTPV.txt'));
tmp_B = readcell(fullfile(WORKPATH, 'SPM_MTPV_1.txt'));

% --- Cleanup ---
FMP_stopServer(serverUid);

end
```

Matlab script 3 (IPM_solver.m)

```
%  FUNCTION: IPM_solver
%  Interfacing with Altair Flux to solve the IPM motor model.
%
%  NOTE: This function shares the exact same logic and structure as
%  SPM_solver. Only the function name and output filenames differ.
%  Redundant code sections have been omitted for brevity.
function [tmp_A, tmp_B] = IPM_solver(WORKPATH, fluxproject, ...
                                     theta_vec_tot, n, Id, Iq)

% ... [Initialization, Server Setup, Project Loading, and Scenario
%      creation are identical to SPM_solver presented above] ...

% --- Post-Processing & Export (DIFFERENCES ONLY) ---

% Define Export Paths (Dynamic, using WORKPATH)
clean_workpath = strrep(WORKPATH, '\', '/');

% CHANGED: Output filenames specific to IPM
file_flux_out  = [clean_workpath, '/IPM_MTPV'];
file_trq_out   = [clean_workpath, '/IPM_MTPV_1'];

% ... [Export Commands via Jython are identical] ...

% Export Flux to TXT
cmd_exp_flux = ['CurveVariation2D["results_flux"].exportTXT(', ...
    'txtFile="', file_flux_out, '", mode="replace")'];
FMP_executeJythonCommand(serverUid, cmd_exp_flux);

% Export Torque to TXT
cmd_exp_trq = ['CurveVariation2D["result_torque"].exportTXT(', ...
    'txtFile="', file_trq_out, '", mode="replace")'];
FMP_executeJythonCommand(serverUid, cmd_exp_trq);

% Save Final State
cmd_save = ['saveProjectAs("', fullfile(WORKPATH, [fluxproject
'_1.FLU']), '")'];
FMP_executeJythonCommand(serverUid, cmd_save);

% --- Read Results into MATLAB ---
% CHANGED: Reading from IPM specific text files
tmp_A = readcell(fullfile(WORKPATH, 'IPM_MTPV.txt'));
tmp_B = readcell(fullfile(WORKPATH, 'IPM_MTPV_1.txt'));

% --- Cleanup ---
FMP_stopServer(serverUid);
End
```

Matlab script 4 (post_processing.m)

```
%% SCRIPT: post_processing.m
%  DESCRIPTION:
%  Performs post-processing analysis for SPM and IPM electric motors
%  1. Generates dense interpolation grids for Flux and Torque.
%  2. Calculates the ideal MTPA (Max Torque Per Ampere) trajectory.
%  3. Simulates the operating envelope (Torque-Speed) considering
%     Voltage and Current limits.
clc;
clear;
close all;

%% 1. GENERAL CONFIGURATION AND PARAMETERS

% --- File Management ---
motor_files  = {'Dati_Motore_SPM.mat', 'Dati_Motore_IPM.mat'};
motor_labels = {'SPM', 'IPM'};
plot_colors  = {'b', 'r'};           % Blue for SPM, Red for IPM

% --- Motor Physical Parameters ---
pole_pairs = 6;              % Number of pole pairs (p)
R_stator   = 0.0451;         % Stator Phase Resistance [Ohm]
scale_fact = 12;             % Scaling factor for flux linkage maps

% --- Drive/Inverter Constraints ---
V_DC_bus    = 400;                 % DC Bus Voltage [V]
% Max phase voltage (Peak) assuming linear modulation range
V_max_phase = V_DC_bus / sqrt(3);

% --- Analysis Settings ---
curr_step_grid = 0.5;    % Step size for dense current grid [A]
rpm_step       = 100;    % Speed increment for the analysis loop [RPM]
max_rpm        = 20000;  % Maximum speed limit for simulation [RPM]
T_threshold    = 0.01;   % Min torque to consider motor "running" [Nm]

% --- Initialize Output Structure ---
RESULTS = struct();

%% 2. MAIN ANALYSIS LOOP

for k = 1:length(motor_files)

    % 2.1 Data Loading and Pre-processing

    filename   = motor_files{k};
    motor_name = motor_labels{k};

    if ~isfile(filename)
        error('File %s not found in directory.', filename);
    end

    fprintf('\n--- PROCESSING MOTOR: %s ---\n', motor_name);

    % Load FEM data
    fem_data = load(filename);

    % Extract maps and apply scaling factors
    lambda_d_raw = fem_data.fd_map * scale_fact;  % D-axis Flux [Wb]
    lambda_q_raw = fem_data.fq_map * scale_fact;  % Q-axis Flux [Wb]
    torque_raw   = fem_data.T_map;                % Torque Map [Nm]

    % Define Current Limits (Simulation specific scaling)
    I_peak_tot  = 7.43 * 72.5 * sqrt(2);
    I_max_rated = (I_peak_tot / 12) * 1;

    % Reconstruct original axis vectors from map dimensions
    dim_d = size(torque_raw, 2);
    dim_q = size(torque_raw, 1);

    % Create linear vectors for raw interpolation
    Id_axis_raw = linspace(-I_max_rated, I_max_rated, dim_d);
```

```
Iq_axis_raw = linspace(-I_max_rated, I_max_rated, dim_q);


% 2.2 Dense Grid Generation (High-Resolution Interpolation)

% High-res meshgrid to accurately find max torque under limits.
[Id_mesh, Iq_mesh] = meshgrid(...
    -I_max_rated : curr_step_grid : I_max_rated, ...
    -I_max_rated : curr_step_grid : I_max_rated);

interp_method = 'spline'; % Spline gives smoother derivatives

% Interpolate Torque and Flux maps onto the dense mesh
Torque_grid   = interp2(Id_axis_raw, Iq_axis_raw, torque_raw, ...
                        Id_mesh, Iq_mesh, interp_method);
Lambda_d_grid = interp2(Id_axis_raw, Iq_axis_raw, lambda_d_raw, ...
                        Id_mesh, Iq_mesh, interp_method);
Lambda_q_grid = interp2(Id_axis_raw, Iq_axis_raw, lambda_q_raw, ...
                        Id_mesh, Iq_mesh, interp_method);


% 2.3 Maximum Torque Per Ampere (MTPA) Locus Calculation

% Scan current circles to find angle yielding max torque.
% This ignores voltage limits (infinite speed assumption).

mtpa_id_vec = [];
mtpa_iq_vec = [];

current_mags = linspace(0, I_max_rated, 200);

for i_mag = current_mags
    % Scan angles in 2nd quadrant (90-180 deg)
    angles = linspace(pi/2, pi, 180);

    id_tr = i_mag * cos(angles);
    iq_tr = i_mag * sin(angles);

    % Interpolate torque on the arc
    t_arc = interp2(Id_axis_raw, Iq_axis_raw, torque_raw, ...
                    id_tr, iq_tr, interp_method);

    [~, max_idx] = max(t_arc);

    mtpa_id_vec(end+1) = id_tr(max_idx);
    mtpa_iq_vec(end+1) = iq_tr(max_idx);
end


% 2.4 Operating Envelope Calculation (Speed Loop)

% Increase speed to find max torque subject to Current & Voltage.

rpm_curr = 0;

% Initialize temporary storage vectors
res_speed = []; res_t_fem = []; res_t_an = [];
res_Id = []; res_Iq = [];

fprintf('   -> Calculating Torque-Speed characteristic...\n');

while true
    % Check absolute speed limit
    if rpm_curr > max_rpm
        fprintf('   -> Reached Max RPM (%d). Stop.\n', max_rpm);
        break;
    end

    % Electrical Angular Velocity [rad/s]
    omega_el = 2 * pi * (pole_pairs * rpm_curr / 60);

    % Calculate Phase Voltage components at every mesh point
    % Vd = Rs*Id - w*Lq  |  Vq = Rs*Iq + w*Ld
    Vd_grid = R_stator * Id_mesh - omega_el * Lambda_q_grid;
```

```
        Vq_grid = R_stator * Iq_mesh + omega_el * Lambda_d_grid;

        % Voltage Magnitude (Peak Phase)
        V_mag_grid = sqrt(Vd_grid.^2 + Vq_grid.^2);

        % --- Apply Constraints ---
        % 1. Current Limit: Inside the circle of radius I_max_rated
        mask_curr = (Id_mesh.^2 + Iq_mesh.^2) <= (I_max_rated^2);

        % 2. Voltage Limit: Inside the voltage ellipse
        mask_volt = V_mag_grid <= V_max_phase;

        % Combined valid operating region
        mask_valid = mask_curr & mask_volt;

        % Apply mask to Torque Grid (Invalid points become -Infinity)
        Torque_masked = Torque_grid;
        Torque_masked(~mask_valid) = -Inf;

        % Find Maximum Torque in the valid region (FEM Torque)
        [max_T_step, lin_idx] = max(Torque_masked(:));

        % Termination: No valid points left or Torque drops to zero
        if isempty(max_T_step) || isinf(max_T_step) || ...
           max_T_step < T_threshold

            fprintf('   -> Voltage limit reached at %d RPM.\n', rpm_curr);
            break;
        end

        % Retrieve corresponding optimal Id, Iq
        [r_idx, c_idx] = ind2sub(size(Torque_masked), lin_idx);
        opt_Id = Id_mesh(r_idx, c_idx);
        opt_Iq = Iq_mesh(r_idx, c_idx);

        % --- Analytic Torque Calculation for Validation ---
        lam_d_pt = Lambda_d_grid(r_idx, c_idx);
        lam_q_pt = Lambda_q_grid(r_idx, c_idx);

        % T = 1.5 * p * (Lambda_d*Iq - Lambda_q*Id)
        T_analytic = 1.5 * pole_pairs * ...
                     (lam_d_pt*opt_Iq - lam_q_pt*opt_Id);

        % Store results for this speed step
        res_speed(end+1) = rpm_curr;
        res_t_fem(end+1) = max_T_step;
        res_t_an(end+1)  = T_analytic;
        res_Id(end+1)    = opt_Id;
        res_Iq(end+1)    = opt_Iq;

        % Increment speed
        rpm_curr = rpm_curr + rpm_step;
    end


    % 2.5 Store Results in Structure

    RESULTS(k).name    = motor_name;
    RESULTS(k).speed   = res_speed;
    RESULTS(k).t_fem   = res_t_fem;    % Torque computed from FEM Map
    RESULTS(k).t_an    = res_t_an;     % Torque computed analytically
    RESULTS(k).Id      = res_Id;       % Optimal D-axis current
    RESULTS(k).Iq      = res_Iq;       % Optimal Q-axis current

    % Mechanical Power [kW] = (T * w_mech) / 1000
    w_mech = res_speed * 2 * pi / 60;
    RESULTS(k).pow     = (res_t_fem .* w_mech) / 1000;

    RESULTS(k).mtpa_id = mtpa_id_vec;
    RESULTS(k).mtpa_iq = mtpa_iq_vec;
    RESULTS(k).Imax    = I_max_rated;  % Used for plotting circle
end
```

Bibliography

[1] B. Tekgun, T. Husain, S. Das, Y. Sozer and M. Hamdan, "Design of a novel interior permanent magnet axial flux machine," 2017 IEEE Energy Conversion Congress and Exposition (ECCE), Cincinnati, OH, USA, 2017, pp. 314-320..

[2] M. A. Rahman, "History of interior permanent magnet motors [History]," in IEEE Industry Applications Magazine, vol. 19, no. 1, pp. 10-15, Jan.-Feb. 2013..

[3] Chau, K. T.. Electric Vehicle Machines and Drives : Design, Analysis and Application, John Wiley & Sons, Incorporated, 2015. ProQuest Ebook Central..

[4] N. Gadiyar, J. Van Verdeghem and E. L. Severson, "A Review of Axial Flux Permanent Magnet Machine Technology," in IEEE Transactions on Industry Applications, vol. 59, no. 4, pp. 3920-3933.

[5] S. Kahourzade, A. Mahmoudi, H. W. Ping and M. N. Uddin, "A Comprehensive Review of Axial-Flux Permanent-Magnet Machines," in Canadian Journal of Electrical and Computer Engineering, vol. 37, no. 1, pp. 19-33.

[6] A. Cavagnino, M. Lazzari, F. Profumo and A. Tenconi, "A comparison between the axial flux and the radial flux structures for PM synchronous motors,", Conference Record of the 2001 IEEE Industry Applications Conference. 36th IAS Annual Meeting (Cat. No.01CH37248), Chicago, IL, USA, 2001, pp. 1611-1618 vol.3.

[7] B. V and C. C, "Characteristic Stability Analysis of Axial Flux Motors in Comparison with Radial Flux Motors Subjected to EV Application," 2023 IEEE International Conference on Power Electronics, and Renewable Energy (PESGRE), India, 2023, pp. 1-6.

[8] Bo Zhang, T. Epskamp, M. Doppelbauer and M. Gregor, "A comparison of the transverse, axial and radial flux PM synchronous motors for electric vehicle," 2014 IEEE International Electric Vehicle Conference (IEVC), Florence, 2014, pp. 1-6..

[9] Z. Azar, L. J. Wu, D. Evans and Z. Q. Zhu, "Influence of rotor configuration on iron and magnet losses of fractional-slot IPM machines," 5th IET International

Conference on Power Electronics, Machines and Drives (PEMD 2010), Brighton, UK, 2010, pp. 1-6..

[10] D. Evans, Z. Azar, L. J. Wu and Z. Q. Zhu, "Comparison of optimal design and performance of PM machines having non-overlapping windings and different rotor topologies," 5th IET International Conference on Power Electronics,, Machines and Drives (PEMD 2010), Brighton, UK, 2010, pp. 1-7.

[11] H. Mel, A. Mansouri and H. Trabelsi, "FEA-based performances evaluation of three permanent magnet machines for traction application," 2019 19th International Conference on Sciences and Techniques of Automatic Control, and Computer Engineering (STA), Sousse, Tunisia, 2019, pp. 353-358.

[12] emetor, Emetor - free resources for electrical machine design - winding editor, 2026, url: https://www.emetor.com/windings/.

[13] Altair Engineering Inc. - Altair Flux Maxwell equation, Flux User Guide, 2026, url: https://help.altair.com/flux/Flux/Help/english/UserGuide/English/topics/EquationsDeMaxwellPourUnSystemeElectrique.htm.

[14] N. Bianchi,; P. Gherardo, L. Cinti; L. Ortombina, "A Review about Flux-Weakening Operating Limits and Control Techniques for Synchronous Motor Drives", in Energies, 2022, pp. 1-18.